3D single breath-hold MR methodology for measuring cardiac parametric mapping at 3T

by

Tiago Fernando Ferreira da Silva

in partial fulfillment of the requirements for the degree of Doctor of Philosophy in

Multimedia and Communications

Universidad Carlos III de Madrid

Advisors:

Javier Sánchez González

Borja Ibáñez Cabeza

Tutor:

Manuel Desco Menéndez

May 2021

This thesis has received funding from the European Union Horizon 2020 research and innovation programme under the Marie Sklodowska-Curie grant agreement N722427

4D ANALYSIS of HEART DEVELOPMENT and
REGENERATION USING ADVANCED LIGHT MICROSCOPY
Innovate Training Network

ACKNOWLEDGMENTS

This thesis would not have been possible without the support and nurturing of many people and here I would like to express my gratitude.

First of all, I would like to acknowledge the Philips team. I cannot begin to express my thanks to Dr. Javier Sánchez González, who played a decisive role in every step of this thesis, providing an invaluable contribution, unwavering support, and wise guidance. I would like to extend my deepest gratitude to Dr. Paula Montesinos, Dr. Claudia de Molina Gómez, and Dr. Víctor Vicente Palacios, who provided me with insightful suggestions, helpful advice, and encouragement throughout this thesis.

I would like to extend my sincere thanks to the members of the Translational Laboratory for Cardiovascular Imaging and Therapy at CNIC. Specifically, I would like to thank Professor Borja Ibáñez for his support and encouragement. Many thanks to Gonzalo López Martín and the other MR technicians for their help and practical suggestions. Special thanks to Robert Austin Benn for his contagious positivity and energy.

I am also grateful to Professor Marcel Breeuwer and the members of the Medical Image Analysis group at the Eindhoven University of Technology for their availability and support during my secondment in Eindhoven.

I very much appreciate the availability and help of Professor Manuel Desco throughout this thesis.

I gratefully acknowledge the assistance of Lilit Manukyan in all matters related to the Marie Sklodowska-Curie grant. Furthermore, I would like to thank my fellow early-stage researchers (Laia, Elena, Paul, Morena, and Eleonora) for their companionship throughout this journey.

Last but not least, I am deeply indebted to my family for their love and unconditional support. My parents, Fernando and Maria Odália Silva, my brother Gonçalo Silva and my life partner Yiyi Ji have always been there for me through thick and thin and make me believe that everything is possible. I dedicate this thesis to our little one, Vicente Silva, who only joined us months ago, but already helped me immensely with his smiles and cooings.

PUBLISHED AND SUBMITTED CONTENT

The following list describes the refereed scientific contributions derived from this thesis:

T. Ferreira da Silva, C. Galan-Arriola, P. Montesinos, G. Javier López-Martín, M. Desco, V. Fuster, B. Ibáñez, J. Sanchez-Gonzalez, "Single breath-hold saturation-recovery 3D cardiac T1 mapping via compressed SENSE at 3T" Magnetic Resonance Materials in Physics, Biology and Medicine (2020). DOI 10.1007/s10334-020-00848-2

- The author provided key ideas to the proposed methodology, developed the pulse sequences and map generation methodologies, designed the study, acquired the data, analyzed the data, and wrote the manuscript.
- This work is fully included in Sections 3.1, 4.1, and 5.1.
- The material from this source included in this thesis is not singled out with typographic means and references.

T. Ferreira da Silva, C. Galan-Arriola, P. Montesinos, V. Vicente-Palacios, M. Veta, M. Breeuwer, B. Ibañez, J. Sánchez-González, "Improving the image quality of cardiac T1 maps via a residual dense network", 37th annual scientific meeting of European Society for Magnetic Resonance in Medicine and Biology, online meeting (2020). DOI 10.1007/s10334-020-00876-y

- The author provided key ideas to the proposed methodology, implemented and trained the convolutional neural network, implemented the pulse sequences and map generation methodologies, designed the study, acquired the data, analyzed the data, wrote the abstract, and presented the Lightning Talk.
- This work is fully included in Sections 3.2, 4.2, and 5.2.
- The material from this source included in this thesis is not singled out with typographic means and references.

T. Ferreira da Silva, P. Montesinos, C. Galan-Arriola, R.A. Benn, B. Ibañez, J. Sánchez-González "3D cardiac T1 and T2 mapping in a single breath-hold via compressed SENSE at 3T", 28th annual meeting of International Society of Magnetic Resonance in Medicine, online meeting (2020)

- The author provided key ideas to the proposed methodology, developed the pulse sequences and map generation methodologies, designed the study, acquired the data, analyzed the data, wrote the abstract, and presented the e-poster.
- This work is partially included in Sections 3.1, 4.1, and 5.1.
- The material from this source included in this thesis is not singled out with typographic means and references.

T. Ferreira da Silva, P. Montesinos, R.A. Benn, C. Galan-Arriola, M. Lobo González, G. López-Martín, B. Ibañez, J. Sánchez-González, "Single breath-hold saturation-recovery 3D cardiac T1 mapping via compressed SENSE at 3T", 27th annual meeting of International Society of Magnetic Resonance in Medicine, Montréal, QC, Canada (2019)

- The author provided key ideas to the proposed methodology, developed the pulse sequences and map generation methodologies, designed the study, acquired the data, analyzed the data, wrote the abstract, and presented the e-poster.
- This work is partially included in Sections 3.1, 4.1, and 5.1.
- The material from this source included in this thesis is not singled out with typographic means and references.

OTHER RESEARCH MERITS

The following list includes articles in peer-reviewed journals that are co-authored by the author and are not related to this thesis:

N. Al-Wakeel-Marquard, **T. Ferreira da Silva**, S. Jeuthe, S. Rastin, F. Muench, D. O h-Ici, S. Yilmaz, F. Berger, T. Kuehne, D. Messroghli, "Measuring myocardial extracellular volume of the right ventricle in patients with congenital heart disease – a T1 mapping study", Scientific Reports. *Under review*

R. Kranzusch, F. Aus dem Siepen, S. Wiesemann, L. Zange, S. Jeuthe, **T. Ferreira da Silva**, T. Kuehne, B. Pieske, C. Tillmanns, M.G. Friedrich, J. Schulz-Menger, D.R. Messroghli, "Z-score mapping for standardized analysis and reporting of cardiovascular magnetic resonance modified Look-Locker inversion recovery (MOLLI) T1 data: Normal behavior and validation in patients with amyloidosis.", Journal of Cardiovascular Magnetic Resonance (2020). DOI 10.1186/s12968-019-0595-7

J.F. Fernandes, R. Alves, **T. Ferreira da Silva**, S. Nordmeyer, F. Hellmeier, L. Goubergrits, A. Hennemuth, F. Berger, S. Schubert, T. Kuehne, M. Kelm, "CMR-Based and Time-Shift Corrected Pressure Gradients Provide Good Agreement to Invasive Measurements in Aortic Coarctation", JACC: Cardiovascular Imaging (2018). DOI 10.1016/j.jcmg.2018.03.013

J.F. Fernandes, L. Goubergrits, J. Brüning, F. Hellmeier, S. Nordmeyer, **T. Ferreira da Silva**, S. Schubert, F. Berger, T. Kuehne, M. Kelm, "Beyond Pressure Gradients: The Effects of Intervention on Heart Power in Aortic Coarctation", PLoS One (2017). DOI 10.1371/journal.pone.0168487

C.M. Augustin, A. Crozier, A. Neic, A.J. Prassl, E. Karabelas, **T. Ferreira da Silva**, J.F. Fernandes, F. Campos, T. Kuehne, G. Plank, "Patient-specific modeling of left ventricular electromechanics as a driver for haemodynamic analysis", EP Europace (2016). DOI 10.1093/europace/euw369

S. Jeuthe, K. Wassilew, D. O H-Ici, **T. Ferreira da Silva**, F. Münch, F. Berger, T. Kuehne, B. Pieske, D.R. Messroghli, "Myocardial T1 maps reflect histological findings in acute and chronic stages of myocarditis in rat model", Journal of Cardiovascular Magnetic Resonance (2016). DOI 10.1186/s12968-016-0241-6

T. Henriques, S. Mariani, A. Burykin, F. Rodrigues, **T.F. Silva**, M.D. Costa, A. Goldberger, "Multiscale Poincaré Plots for Visualizing the Structure of Heartbeat Time Series", BMC Medical Informatics and Decision Making (2016). DOI 10.1186/s12911-016-0252-0

A. Burykin, S. Mariani; T. Henriques; **T.F. Silva**, W. Schnettler, M. Costa, A. Goldberger, "Remembrance of time series past: simple chromatic method for visualizing trends in biomedical signals", Physiological Measurement (2015). DOI 10.1088/0967-3334/36/7/n95

ABSTRACT

One of the foremost and challenging subfields of MRI is cardiac magnetic resonance imaging (CMR). CMR is becoming an indispensable tool in cardiovascular medicine by acquiring data about anatomy and function simultaneously. For instance, it allows the non-invasive characterization of myocardial tissues via parametric mapping techniques. These mapping techniques provide a spatial visualization of quantitative changes in the myocardial parameters. Inspired by the need to develop novel high-quality parametric sequences for 3T, this thesis's primary goal is to introduce an accurate and efficient 3D single breath-hold MR methodology for measuring cardiac parametric mapping at 3T.

This thesis is divided into two main parts: i) research and development of a new 3D T1 saturation recovery mapping technique (3D SACORA), together with a feasibility study regarding the possibility of adding a T2 mapping feature to 3D SACORA concepts, and ii) research and implementation of a deep learning-based post-processing method to improve the T1 maps obtained with 3D SACORA.

In the first part of the thesis, 3D SACORA was developed as a new 3D T1 mapping sequence to speed up T1 mapping acquisition of the whole heart. The proposed sequence was validated in phantoms against the gold standard technique IR-SE and in-vivo against the reference sequence 3D SASHA. The 3D SACORA pulse sequence design was focused on acquiring the entire left ventricle in a single breath-hold while achieving good quality T1 mapping and stability over a wide range of heart rates (HRs). The precision and accuracy of 3D SACORA were assessed in phantom experiments. Reference T1 values were obtained using IR-SE. In order to further validate 3D SACORA T1 estimation accuracy and precision, T1 values were also estimated using an in-house version of 3D SASHA. For in-vivo validation, seven large healthy pigs were scanned with 3D SACORA and 3D SASHA. In all pigs, images were acquired before and after administration of MR contrast agent.

The phantom results showed good agreement and no significant bias between methods. In the in-vivo experiments, all T1-weighted images showed good contrast and quality, and the T1 maps correctly represented the information contained in the T1-weighted images. Septal

T1s and coefficients of variation did not considerably differ between the two sequences, confirming good accuracy and precision. 3D SACORA images showed good contrast, homogeneity and were comparable to corresponding 3D SASHA images, despite the shorter acquisition time (15s vs. 188s, for a heart rate of 60 bpm). In conclusion, the proposed 3D SACORA successfully acquired a whole-heart 3D T1 map in a single breath-hold at 3T, estimating T1 values in agreement with those obtained with the IR-SE and 3D SASHA sequences.

Following the successful validation of 3D SACORA, a feasibility study was performed to assess the potential of modifying the acquisition scheme of 3D SACORA in order to obtain T1 and T2 maps simultaneously in a single breath-hold. This 3D T1/T2 sequence was named 3D dual saturation-recovery compressed SENSE rapid acquisition (3D dual-SACORA). A phantom of eight tubes was built to validate the proposed sequence. The phantom was scanned with 3D dual-SACORA with a simulated heart rate of 60 bpm. Reference T1 and T2 values were estimated using IR-SE and GraSE sequences, respectively. An in-vivo study was performed with a healthy volunteer to evaluate the parametric maps' image quality obtained with the 3D dual-SACORA sequence.

T1 and T2 maps of the phantom were successfully obtained with the 3D dual-SACORA sequence. The results show that the proposed sequence achieved good precision and accuracy for most values. A volunteer was successfully scanned with the proposed sequence (acquisition duration of approximately 20s) in a single breath-hold. The saturation time images and the parametric maps obtained with the 3D dual-SACORA sequence showed good contrast and homogeneity. The septal T1 and T2 values are in good agreement with reference sequences and published work. In conclusion, this feasibility study's findings open the door to the possibility of using 3D SACORA concepts to develop a successful 3D T1/T2 sequence.

In the second part of the thesis, a deep learning-based super-resolution model was implemented to improve the image quality of the T1 maps of 3D SACORA, and a comprehensive study of the performance of the model in different MR image datasets and sequences was performed. After careful consideration, the selected convolutional neural network to improve the image quality of the T1 maps was the Residual Dense Network (RDN). This network has shown outstanding performance against state-of-the-art methods

on benchmark datasets; however, it has not been validated on MR datasets. In this way, the RDN model was initially validated on cardiac and brain benchmark datasets. After this validation, the model was validated on a self-acquired cardiac dataset and on improving T1 maps.

The RDN model improved the images successfully for the two benchmark datasets, achieving better performance with the brain dataset than with the cardiac dataset. This result was expected as the brain images have more well-defined edges than the cardiac images, making the resolution enhancement more evident. On the self-acquired cardiac dataset, the model also obtained an enhanced performance on image quality assessment metrics and improved visual assessment, particularly on well-defined edges. Regarding the T1 mapping sequences, the model improved the image quality of the saturation time images and the T1 maps. The model was able to enhance the T1 maps analytically and visually. Analytically, the model did not considerably modify the T1 values while improving the standard deviation in both myocardium and blood. Visually, the model improved the T1 maps by removing noise and motion artifacts without losing resolution on the edges. In conclusion, the RDN model was validated on three different MR datasets and used to improve the image quality of the T1 maps obtained with 3D SACORA and 3D SASHA.

In summary, a 3D single breath-hold MR methodology was introduced, including a ready-to-go 3D single breath-hold T1 mapping sequence for 3T (3D SACORA), together with the ideas for a new 3D T1/T2 mapping sequence (3D dual-SACORA); and a deep learning-based post-processing implementation capable of improving the image quality of 3D SACORA T1 maps.

CONTENTS

LIST OF FIGURES

LIST OF TABLES

CHAPTER 1

INTRODUCTION

Medical imaging is a primary field of current medical research and practice, and there is a continuous drive to improve medical imaging techniques to provide high-quality and cost-effective healthcare. Medical imaging has progressed tremendously during the past decades, fuelled by new high-tech equipment and digital technology breakthroughs. Some of the modalities that have seen significant improvements are magnetic resonance imaging (MRI), radiography, computed tomography, and ultrasound.

Although MRI is critical in today's clinical practice, it is a relatively recent technology with plenty of room to improve. Nuclear magnetic resonance (NMR), the physical phenomenon used by MRI, was presented by the groups of Edwards Mills Purcell and Felix Bloch in 1946 [1, 2], who won the Nobel Prize in Physics in 1952. Later, Paul C. Lauterbur and Peter Mansfield groups made feasible NMR's practical application to medical imaging in the early 1970s [3, 4], sharing the Nobel Prize in Medicine or Physiology in 2003. MRI is a non-invasive technique with the capability to provide images containing reliable information about anatomy, physiology, and pathology. The main advantages of MRI are the non-ionizing radiation, the low side effects of the contrast agents, and the excellent contrast between soft tissues achieved by using their physical and biochemical properties.

One of the foremost and challenging subfields of MRI is cardiac magnetic resonance imaging (CMR). CMR is becoming an indispensable tool in cardiovascular medicine by acquiring data about anatomy and function simultaneously. For instance, it provides unique information about structural changes in the myocardium, being an alternative to myocardial biopsies and histochemical analysis. Although a powerful technique, CMR is challenging due to cardiac motion, and tremendous efforts have been put into research in cardiac acquisitions, triggering, and post-processing algorithms, motivated by the fact that cardiovascular diseases are the leading cause of worldwide deaths. Groundbreaking developments such as 3-dimensional (3D) techniques, parallel imaging, compressed sensing

(CS), fingerprinting, and artificial intelligence (AI) have continuously advanced the performance and versatility of CMR; however, there is still room to decrease acquisition time, improve image quality and reduce costs. Thus, novel high-quality approaches are welcome for advancing CMR and, ultimately, for better patient care.

1.1. MRI Basics

MRI is derived from NMR, a phenomenon based on the interaction between the nuclear spin and an external static magnetic field. In clinical MRI, the nucleus of the hydrogen atom is the most relevant for imaging due to its abundance in water and fat. It is a single positively-charged proton and is continuously rotating, generating a tiny magnetic field known as the magnetic moment. If a strong external magnetic field (B0) is applied, the magnetic moment of the proton experiences a twisting force (torque), and it starts precessing around the B0 field (**Figure 1-1**). The precessional frequency is proportional to the B0 field and is known as the Larmor precession frequency (ω_0)

$$\omega_0 = \gamma B_0 \tag{1.1}$$

Where γ is a constant named the gyromagnetic ratio, and B0 is the external magnetic field. In this way, all the protons precess at the same Larmor frequency while inside the same B0 field.

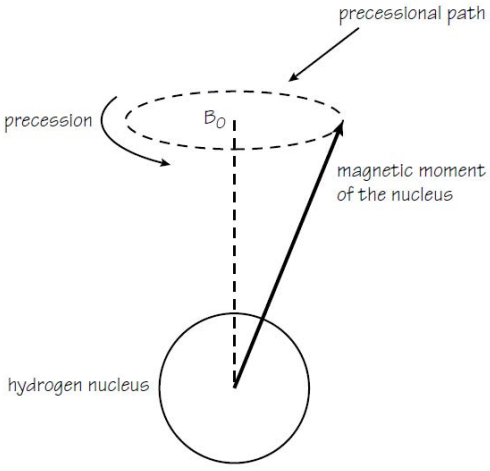

Figure 1-1 – Precession of the magnetic moment of the hydrogen nucleus in the presence of an external magnetic field B0. Image from [5].

The protons precess in one of two energy levels, known as nuclear Zeeman levels: an energy level parallel to the B0 field (lower energy, spin-up) and an energy level anti-parallel to the B0 field (higher energy, spin-down). The frequency of electromagnetic radiation required to cause transitions between the two levels is the Larmor precession frequency mentioned above. There are slightly more protons located at the lower energy level than at the higher energy level, and this small difference leads to a net macroscopic magnetization, known as M0, as shown in **Figure 1-2**. M0 aligns perfectly with the B0 field and is associated with the z-direction.

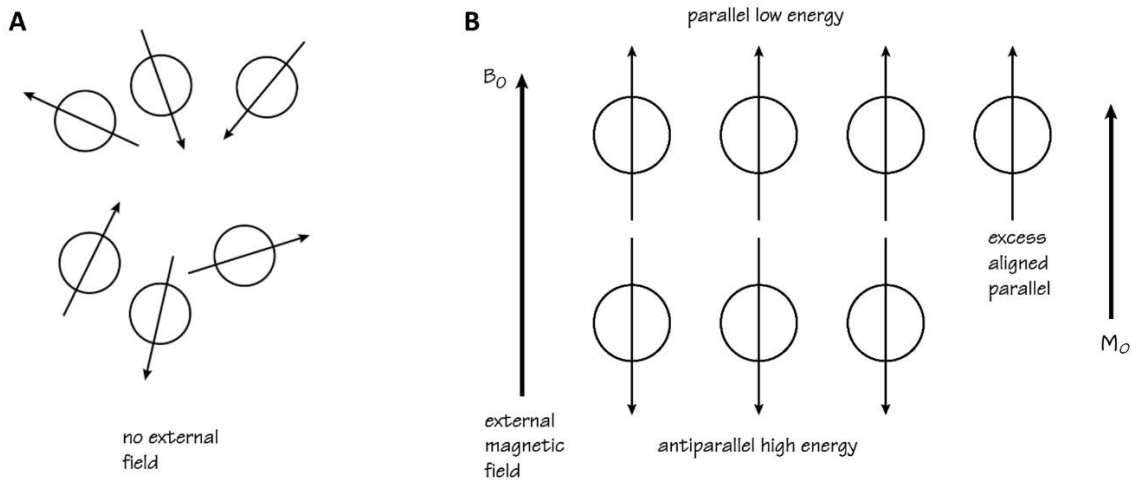

Figure 1-2 – Protons in the absence (A) and presence (B) of an external magnetic field B0. A) The protons are randomly aligned – the net magnetization is null. B) The protons align parallel (lower energy, spin-up) or anti-parallel (higher energy, spin-down) to the B0, and a measurable net magnetization M0 is created by the excess of protons in the lower energy level. Image adapted from [5].

Since M0 magnetization is small and parallel to the B0 field, measuring it is practically impossible at equilibrium. A circularly polarized radiofrequency (RF) field (B1) is applied perpendicular to the B0 field with a frequency equal to the Larmor frequency to tip 90 degrees the M0 to the x-y plane (transverse plane), as shown in **Figure 1-3**. This process also brings the protons into phase coherence, creating the oscillating decaying MRI signal that is detected and measured by a receiver coil (sensitive to magnetization perpendicular to B0) while the protons dephasing occurs. The signal amplitude decays exponentially during the protons

dephasing – free induction decay (FID). The RF pulse flip angle is not always required to be 90 degrees and can be adjusted by changing the pulse's strength and duration; for instance, a flip angle of 180 degrees is often applied. The MRI sequences never aim to measure the FID directly; instead, they use the spin (SE) and gradient (GE) echoes, as described in more detail in section 1.2.

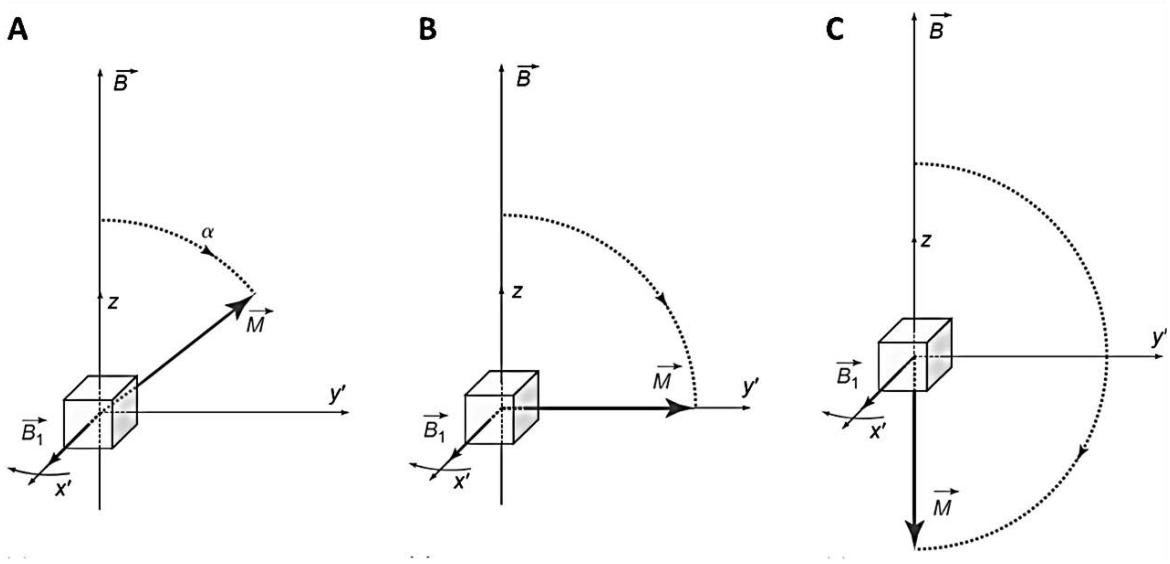

Figure 1-3 – M0 is tipped when a circularly polarized radiofrequency (RF) field (B1) is applied perpendicular to the B0 field with a frequency equal to the Larmor frequency. A) The angle between the z-axis and M, denominated as the flip angle (α), depends on the RF pulse's strength and duration. B) A 90° RF-pulse creates a 90° flip angle. C) A 180° RF-pulse, also known as an inversion pulse, creates a 180° flip angle. Image adapted from [6].

As soon as the excitation process is over, the protons start the relaxation process immediately, relaxing progressively from the x-y plane to the equilibrium M0, shown in **Figure 1-4**. The relaxation consists of the protons' dephasing and the release of the energy absorbed during the excitation.

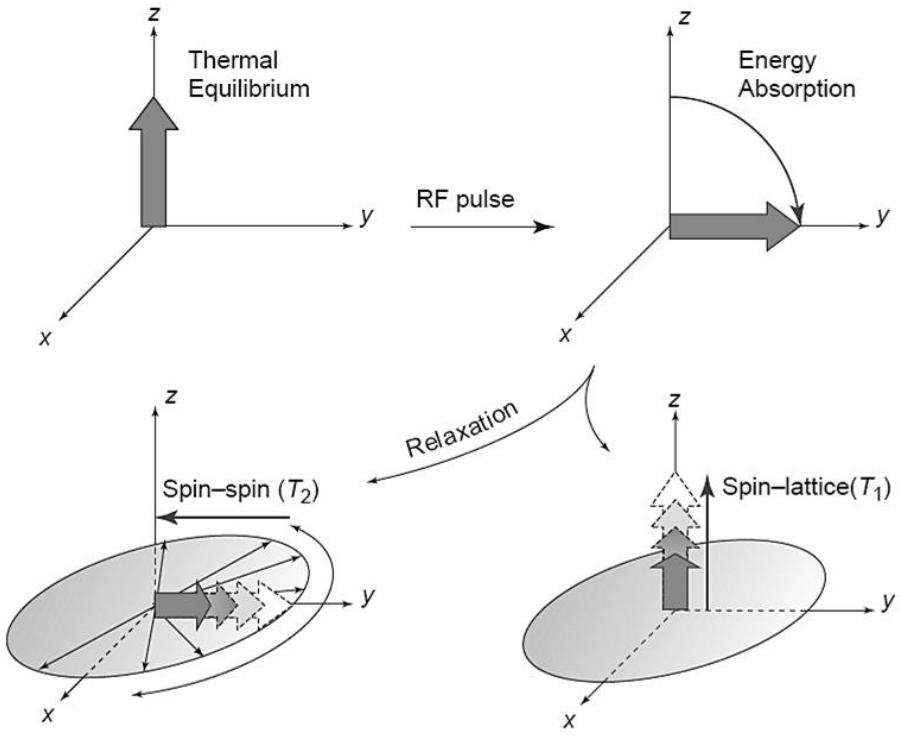

Figure 1-4 – Free induction decay process. Immediately after the RF pulse, the spin-spin (T2) and spin-lattice (T1) relaxations start, and eventually, the thermal equilibrium is reached again. Image adapted from [6].

The protons' dephasing is due to differences in their precessional frequencies. These differences arise because of the inevitable inhomogeneities in the B0 field and the interactions between the protons. The protons' interactions make the transverse magnetization decrease gradually to zero following an exponential decay function (**Figure 1-5**). This process is known as spin-spin relaxation, and the time required to drop the transverse magnetization to 37% is known as the relaxation time T2. The spin-spin relaxation is a very rapid process, reaching a zero transverse magnetization after tens of milliseconds. The efficiency of the spin-spin relaxation depends mostly on the proximity of the protons and molecular motion. Therefore, the T2 value of water is longer than the T2 value of fat as the protons' motion is less constrained.

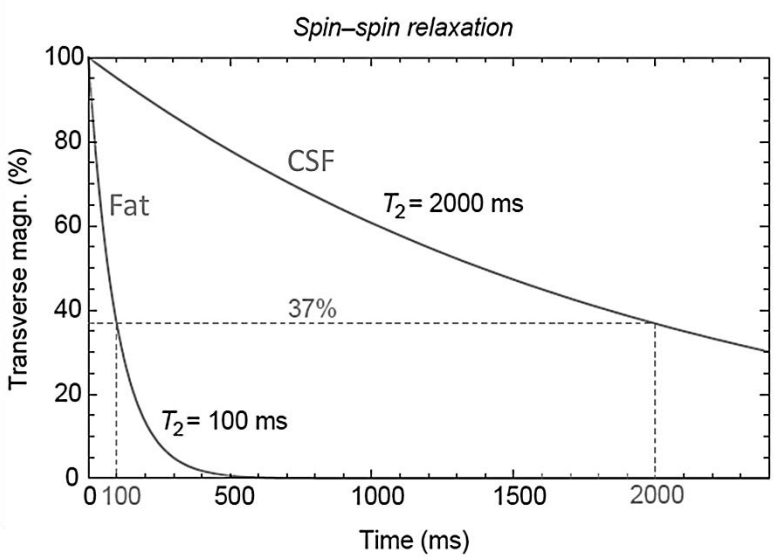

Figure 1-5 – Spin-spin relaxation process for cerebrospinal fluid (CSF) and fat. At 1.5 T, T2 of the fat is ~100 ms, while T2 of CSF is ~2000 ms. Image adapted from [6].

The spin-spin relaxation does not yield a net loss of energy; a net loss of energy only occurs with the protons' interaction with the surrounding tissues (lattice). The release of the energy absorbed during the excitation to the lattice makes the longitudinal magnetization gradually return to the equilibrium M0; in other words, the protons gradually disperse the extra energy and return to the equilibrium populations in the two Zeeman energy levels (i.e., spin-up or spin-down). This process is known as spin-lattice relaxation, and the time required for the longitudinal magnetization to reach 63% of the equilibrium M0 is known as the relaxation time T1. The spin-lattice relaxation is exponential and takes hundreds of milliseconds to reach the equilibrium M0 (**Figure 1-6**). The efficiency of the tissue in releasing energy to the surrounding environment determines its T1 value. Water is much less efficient than fat in this process, and therefore, the T1 value of water is much longer. T1 is substantially longer than T2 in human tissues and changes considerably with the magnetic field strength.

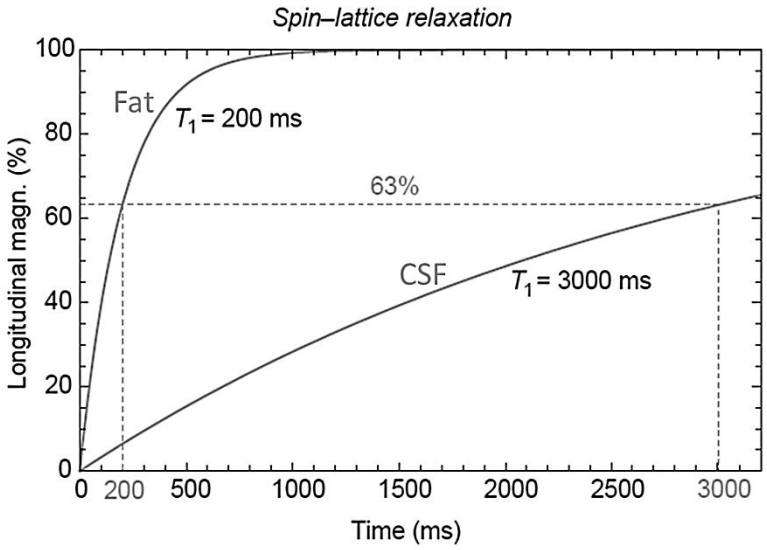

Figure 1-6 – Spin-lattice relaxation process for fat and cerebrospinal fluid (CSF). At 1.5 T, T1 of the fat is ~200 ms, while T1 of CSF is ~3000 ms. Image adapted from [6].

The relaxation mechanisms are routinely modified by contrast agents to improve image quality and diagnostic accuracy. Gadolinium is a contrast agent with strong paramagnetic properties, and therefore, it gets much more magnetized in a magnetic field than the human tissue. The main effects of using gadolinium are the improvement of the signal-to-noise-ratio (SNR) of the T1-weighted images and the decrease of the T1 and T2 relaxation times. In clinical practice, the fact that tissues affected by the contrast agent appear with an enhanced signal on the T1-weighted images is beneficial to decision making.

The external magnetic field B0 of the scanner is homogeneous. In this way, all the protons present the same Larmor frequency, which is the frequency targeted by the excitation RF pulse. However, in practice, the RF pulse excites only a slice of protons due to a gradient field superimposed to B0, known as the slice-selective gradient. The slice-selective gradient changes the magnetic field experienced by the protons according to their slice and thus changes their precessional frequency (**Figure 1-7**).

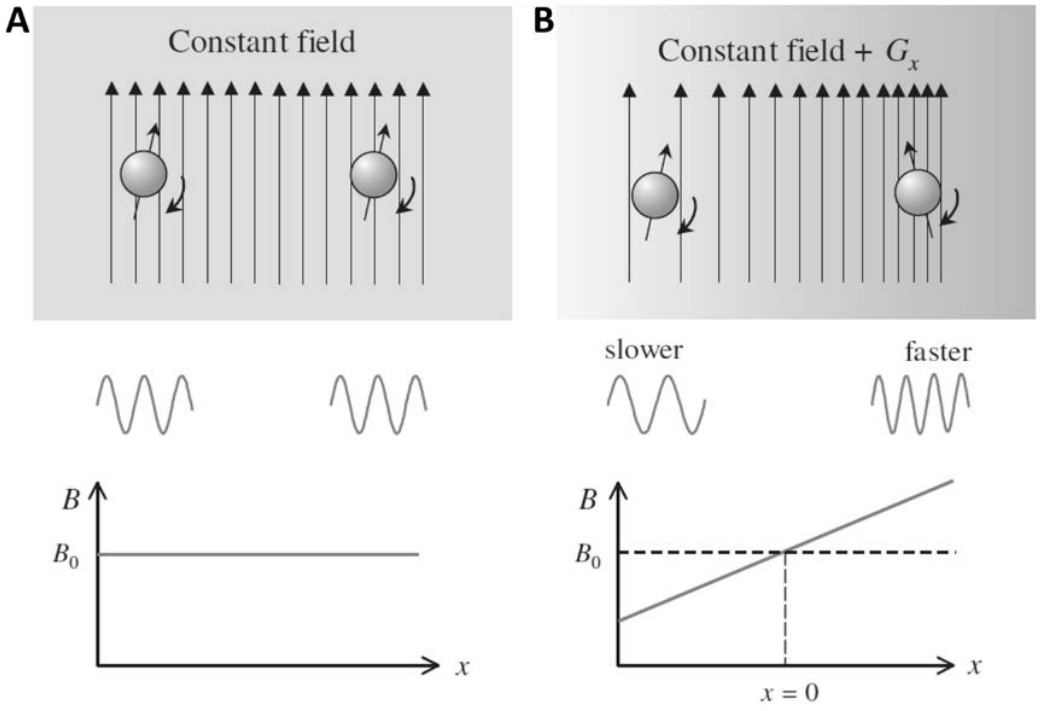

Figure 1-7 – Effect of the field gradient. **A)** In a constant field, i.e., B0, all protons precess at the same Larmor frequency. **B)** When a field gradient (G_x) is added, the protons' precessional frequency becomes position-dependent. Image adapted from [7].

Since the protons' precessional frequencies are different for each slice, RF pulses of specific frequencies can excite specific slices, making it possible to examine all imaging planes without moving the patient. The slice-selective gradient steepness and the RF pulse bandwidth determine the slice thickness (**Figure 1-8**).

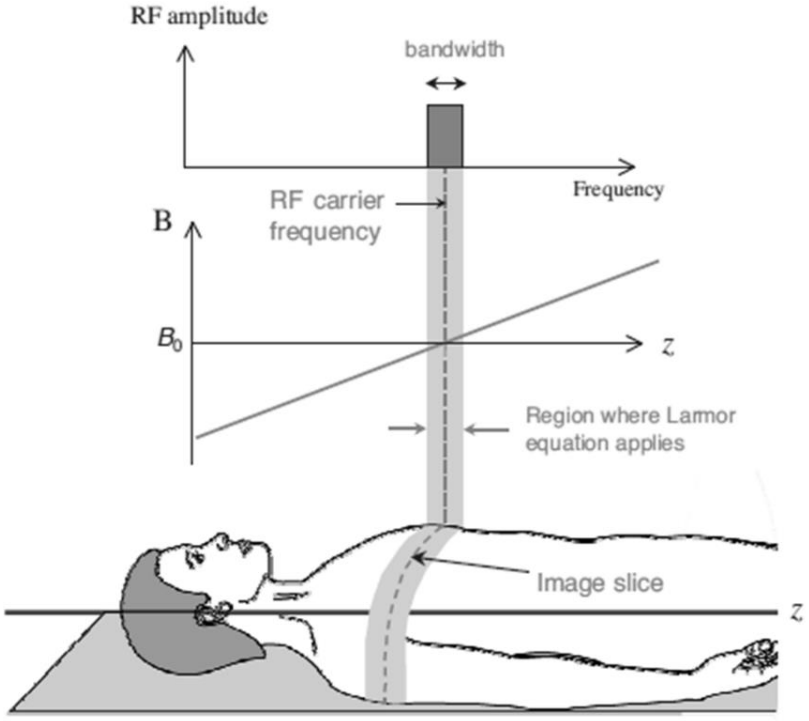

Figure 1-8 – The slice-selective gradient modifies the precessional frequency of protons at different slices. When an RF pulse with a specific frequency is applied, only the image slice with that frequency is selected. Image adapted from [7].

The position within the slice from where the signal is coming is still unknown only with the slice selection. Two other gradient fields (the frequency-encoding gradient and the phase-encoding gradient) are applied to determine this position. The frequency encoding gradient is applied after the excitation RF pulse and the phase-encoding gradient, while the MR signal is received. All the protons have the same precessional frequency after the slice-selective gradient, so the frequency-encoding gradient is applied perpendicularly to the slice-selective gradient to modify that precessional frequency. In this way, different columns of the slice have different precessional frequencies and emit signals with those frequencies (**Figure 1-9**).

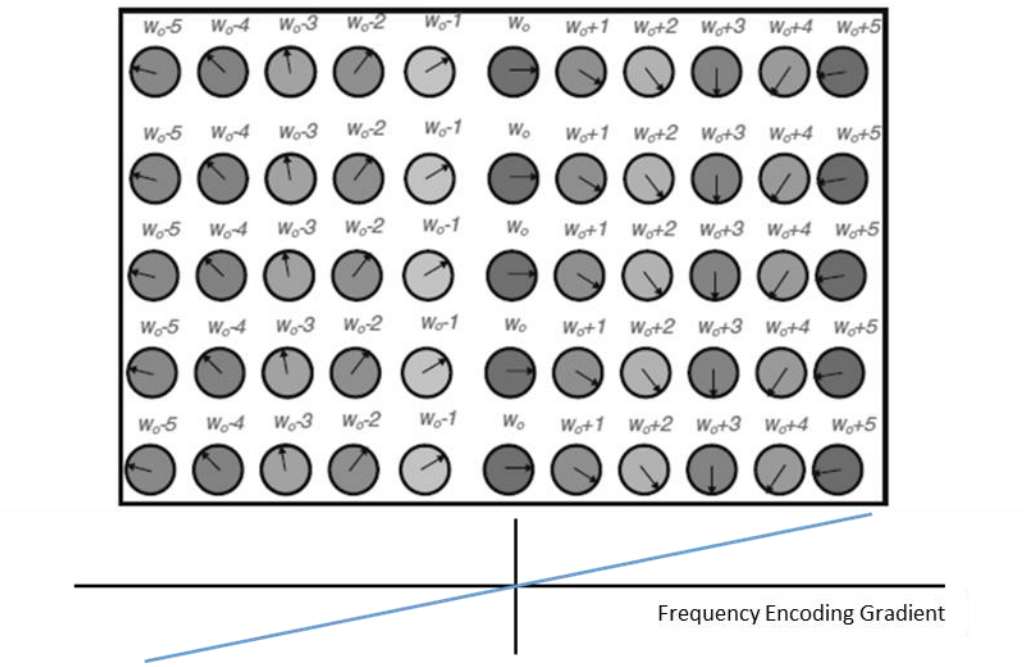

Figure 1-9 – Frequency encoding. Image adapted from [8].

However, the same column protons still have the same frequency, which is why the phase-encoding gradient is required. This gradient uses the fact that all protons are in phase after the excitation RF pulse. It is applied during a short time between the excitation and the frequency-encoding gradient to slightly change the protons' precessional frequency according to the magnetic field strength, dephasing the protons according to their position in the column. After switching off this gradient, the precessional frequency gets back to normal, while the protons continue dephased. In this way, protons in the same column emit signals with the same frequency but different phases (**Figure 1-10**). Hence, the signals coming out of the slice have different frequencies and phases according to the location, encoding spatial information.

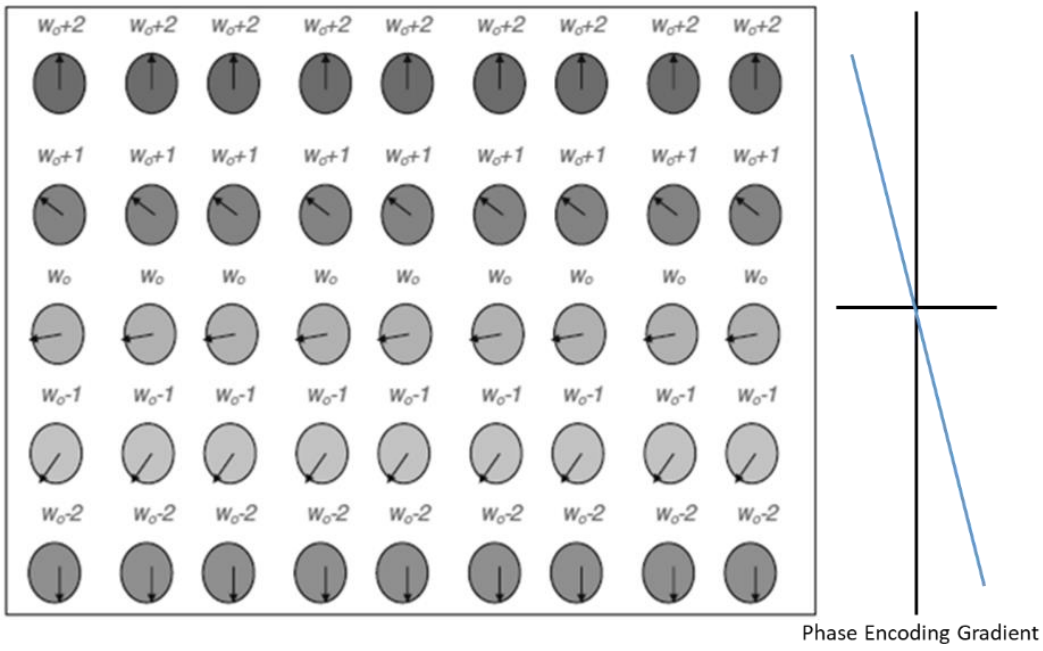

Figure 1-10 – Phase encoding. Image adapted from [8].

The raw data collected from the MR signal during a scan are stored in a matrix called k-space. K-space represents the acquired image's spatial frequency domain, and after the k-space is filled, an MR image is reconstructed by applying a 2D Fourier transform.

The data in k-space can be collected linearly – cartesian sampling or non-linearly – non-cartesian sampling (**Figure 1-11**). In the cartesian sampling, the horizontal axis of the k-space typically stores the frequency-encoding information, and the vertical axis typically stores the phase-encoding information. The number of phase encoding steps determine substantially the duration of the measurement. Non-cartesian sampling follows non-linear trajectories. For instance, in the radial and spiral samplings, the frequency and phase encoding gradients are manipulated simultaneously to allow transversals in the k-space, off the cartesian grid. Some advantages of these strategies include faster acquisition and less sensitivity to motion artifacts than cartesian sampling. On the other hand, the periphery of the k-space is relatively undersampled, which can compromise spatial resolution. The image reconstruction is not as straightforward as in cartesian sampling, as the data points need to be re-gridded in a rectangular matrix before Fourier transformation.

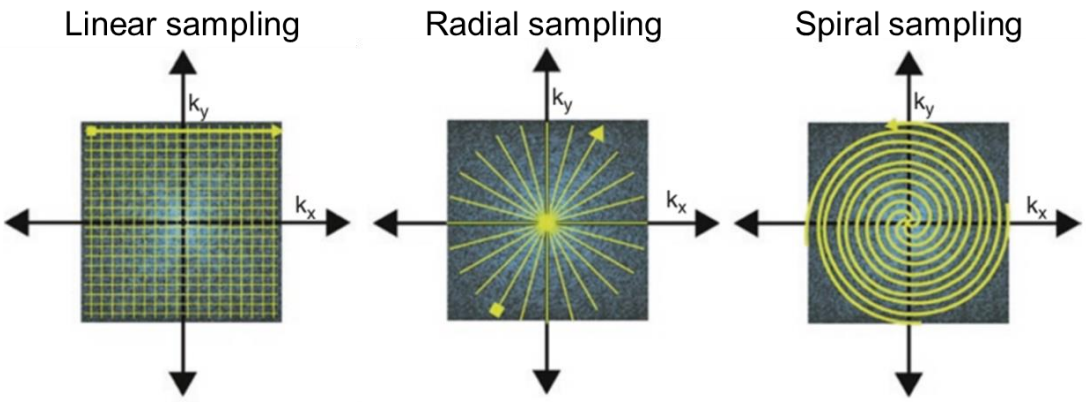

Figure 1-11 – K-space data sampling trajectories. Image adapted from [9].

Although the k-space and the image space have the same size, the lines in the k-space do not correspond to lines in the image space, i.e., the bottom lines of the k-space do not correspond to the bottom lines of the image. Instead, the data from the center of k-space (low spatial frequencies) contain signal-to-noise and contrast information, while the data from outer areas (high spatial frequencies) contain image resolution information, i.e., boundaries and edges (**Figure 1-12**).

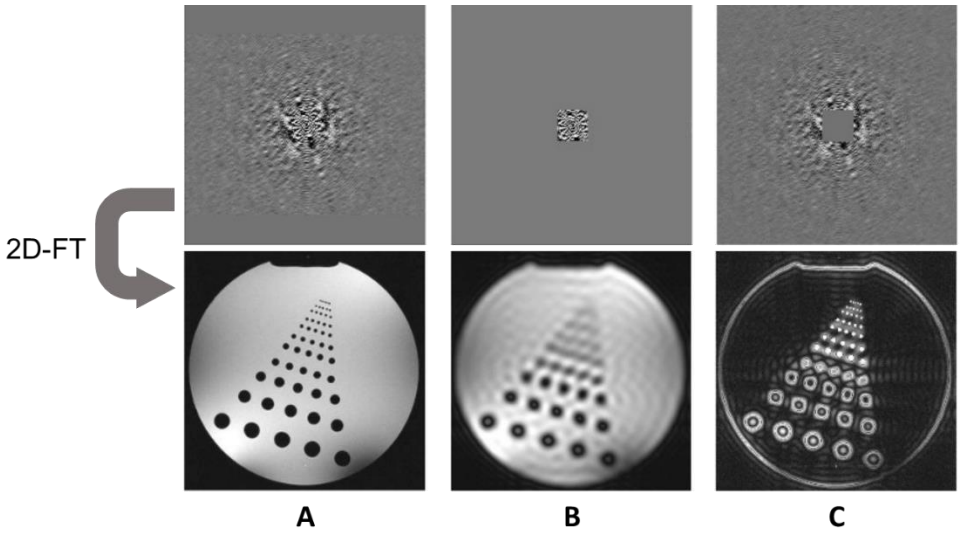

Figure 1-12 – K-space and corresponding MR images. A) complete k-space – contains all contrast, signal, and resolution information. B) center of k-space only – contains contrast information, but it lacks resolution. C) outer k-space only – contains information about edges and boundaries, but it lacks signal and contrast. Image adapted from [10].

1.2. Quantitative CMR: Acquisition

Two types of MR sequences are the standard for MRI acquisition: gradient-echo (GE) and spin-echo (SE). Despite the ever-increasing amount of different sequences, GE and SE sequences continue to be the basic models of the structure of MR sequences. For both cases, the sequences start with an excitation RF pulse. This RF pulse has a flip angle of 90º for SE sequences and smaller flip angles for GE sequences. In SE sequences, the protons dephase naturally after 90º excitation until a 180º excitation is applied to reverse the protons phase angle without changing the precessional frequencies. The protons come back into phase after a period equal to the time between the 90º pulse and the 180º pulse, creating the spin-echo and emitting the signal (**Figure 1-13**).

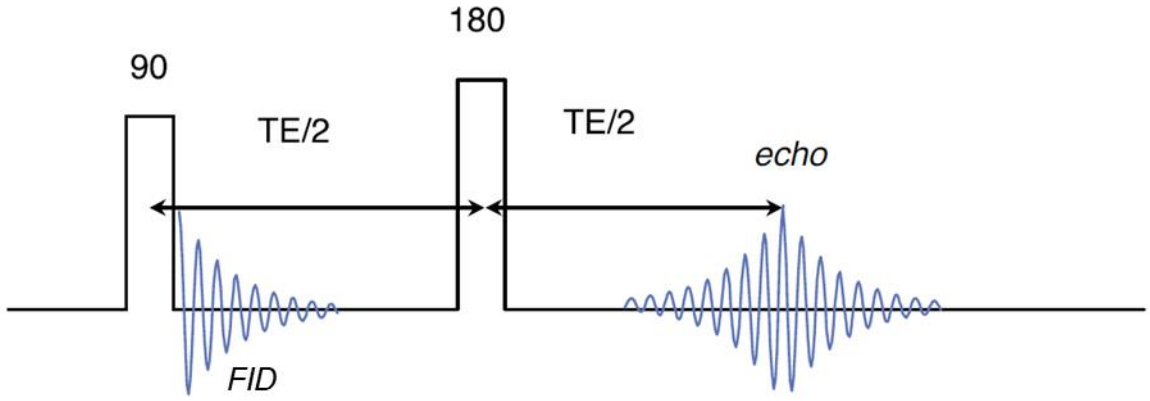

Figure 1-13 – Basic sequence spin-echo (SE). Image adapted from [7].

In GE sequences, a very fast dephasing of the transverse magnetization is caused by a negative gradient lobe immediately after the excitation pulse. The magnetic field gradient is then reversed with the application of a positive gradient, which makes the protons that were precessing at a low frequency start precessing at a higher frequency and vice-versa. After some time, the protons are in phase, creating the gradient echo and emitting the signal (**Figure 1-14**). Based on either SE or GE sequences structure, a vast amount of sequences have been developed to improve MRI performance over the years, mainly driven by the need to speed up acquisitions.

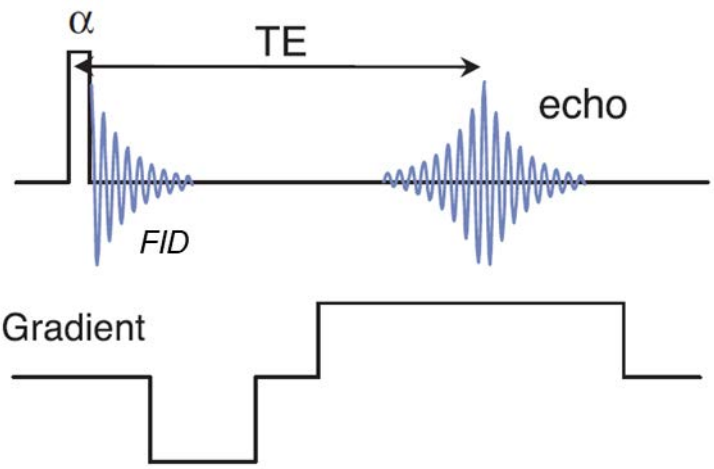

Figure 1-14 – Basic sequence gradient-echo (GE). Image adapted from [7].

Next, the focus is on describing the sequences relevant to this work: cardiac sequences of T1 mapping, T2 mapping, and T1/T2 mapping. A particular focus is put on sequences that were used in this work.

1.2.1. T1 mapping sequences

T1 mapping provides pixel-wise T1 values by fitting images acquired during the T1 magnetization recovery at different times after application of an inversion pulse [11], a saturation pulse [12], or a combination of both [13].

CMR T1 mapping is complex due to the heart's motion, and several two-dimensional (2D) pulse sequences have been presented in recent years to tackle the problem [14–16]. However, these sequences are designed to acquire only a single slice per breath-hold. The modified Look-Locker inversion recovery (MOLLI) sequence applies an inversion pulse followed by different single-shot steady-state free precession (SSFP) readouts over multiple heartbeats [11]. MOLLI is precise and reproducible; however, it underestimates T1, mainly due to the magnetization transfer effect and imperfect inversion efficiency [15]. To overcome this limitation, saturation recovery single-shot acquisition (SASHA) replaces the inversion pulses with saturation pulses, thus avoiding the underestimation of T1 values due to incomplete

recovery of the signal after the inversion pulse [12]. This approach improves accuracy at the cost of a lower signal-to-noise ratio (SNR). A different 2D saturation recovery sequence design is provided by modified Look-Locker acquisition using saturation recovery (MLLSR), which allows the saturation pulses to be shared between several readouts acquired in different heart beats in order to minimize T1 estimation error and provide high flexibility [17]. Lastly, saturation pulse-prepared heart rate independent inversion recovery (SAPPHIRE) is a hybrid approach that uses inversion and saturation pulses and sits at the midpoint between the advantages and limitations of saturation and inversion schemes [13].

Highly accurate T1 estimates can also be obtained with three-dimensional (3D) pulse sequences based on saturation recovery and developed to fully cover the left ventricle (LV). 3D SASHA combines a 2D SASHA-based pulse scheme with free-breathing imaging for 3D acquisition at 1.5T [18]. A more recent free-breathing 3D T1 mapping sequence provides 3D acquisition at 3T, based on a new pulse scheme that acquires substantially fewer T1-weighted images than 3D SASHA [19]. These 3D saturation recovery approaches offer higher SNR and good spatial coverage at the cost of longer acquisition times. They require navigator-triggered free-breathing and therefore rely on the respiratory navigation performance to achieve good image quality and acceptable acquisition time. Acquisition time is nevertheless in the range of minutes, even when denoising and optimization techniques are used [20, 21]. Such long acquisition time compromises the feasibility of T1 mapping during contrast equilibrium and reduces clinical applicability. Furthermore, these 3D saturation recovery sequences acquire all T1-weighted images in the same RR interval of the saturation pulse, which compromises T1 estimation quality, particularly for long T1s and high heart rates [22].

Independently of magnetic preparation, most proposed T1 mapping techniques are acquired using SSFP readout techniques. At 3T, SSFP sequences have been associated with higher energy deposition and increased off-resonance artifacts [23]. Alternatives to SSFP sequences are spoiled sequences. These sequences use fast low-angle shot (FLASH) imaging readouts to avoid off-resonance artifacts and to eliminate transverse relaxation time (T2) dependence [19, 24, 25]. The main limitation of FLASH schemes is the low SNR compared with SSFP sequences.

Inversion recovery spin-echo (IR-SE)

The standard version of the Inversion recovery spin-echo (IR-SE) is an SE sequence with an additional 180º pulse (inversion pulse) applied at the beginning of the conventional SE sequence - before the 90º excitation pulse. The inversion pulse flips the longitudinal magnetization from positive to negative without forming a signal since there is no magnetization in the transverse plane. Then, the longitudinal relaxation starts, and the longitudinal magnetization moves in direction to the equilibrium at the initial orientation. After some time, known as the inversion time (TI), the 90º excitation pulse is applied, starting the conventional SE sequence (**Figure 1-15**). T1-weighted images with different inversion times yield different image contrast since the amount of longitudinal magnetization flipped into the transverse plane depends on the inversion time. Acquiring T1-weighted images with IR-SE is time-consuming but can be used to compute T1 maps of very high signal-to-noise-ratio (SNR) and accuracy. Nowadays, IR-SE is mostly used as a reference sequence during the development of new sequences or when comparing different sequences.

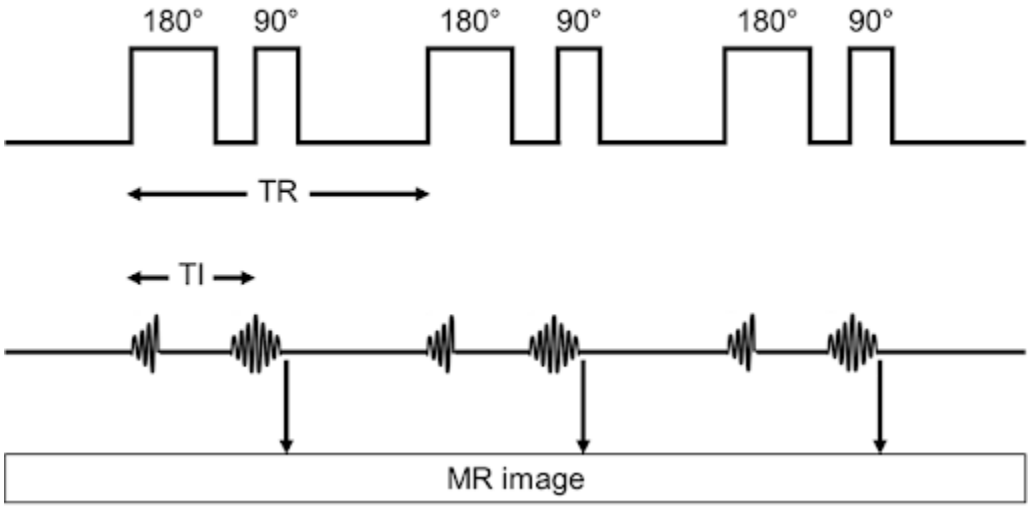

Figure 1-15 –Schematic of the Inversion recovery spin-echo (IR-SE) sequence. Image adapted from [26].

Modified Look-Locker Inversion Recovery (MOLLI)

Modified Look-Locker Inversion Recovery (MOLLI) was presented in 2004 by Daniel R. Messroghli et al. [11]. MOLLI is an inversion recovery sequence and applies two or three

inversion pulses, depending on the strategy. After the inversion pulses, single-shot SSFP readouts are applied at certain inversion times, acquiring the T1-weighted images. A resting period of three or four heartbeats is required before the inversion pulses to allow recovery of the longitudinal magnetization. The original version of MOLLI consisted of three inversion pulses with three, three, and five readouts, respectively (**Figure 1-16**). The recovery period before the inversion pulses was four seconds. The optimized MOLLI sequence used nowadays as the gold standard of inversion recovery sequences allows a shorter acquisition time for T1 mapping. A typical implementation consists of two inversion pulses with five and three readouts, respectively, with a recovery period before the second inversion pulse of three heartbeats. This MOLLI implementation is commonly denoted as 5(3)3. The inversion pulses implementation takes into account that the T1-weighted images need to be acquired at the same place in the cardiac cycle to accurately calculate the T1 values. In post-contrast imaging, shorter recovery periods can be used due to the shorter T1 values, decreasing MOLLI's acquisition time.

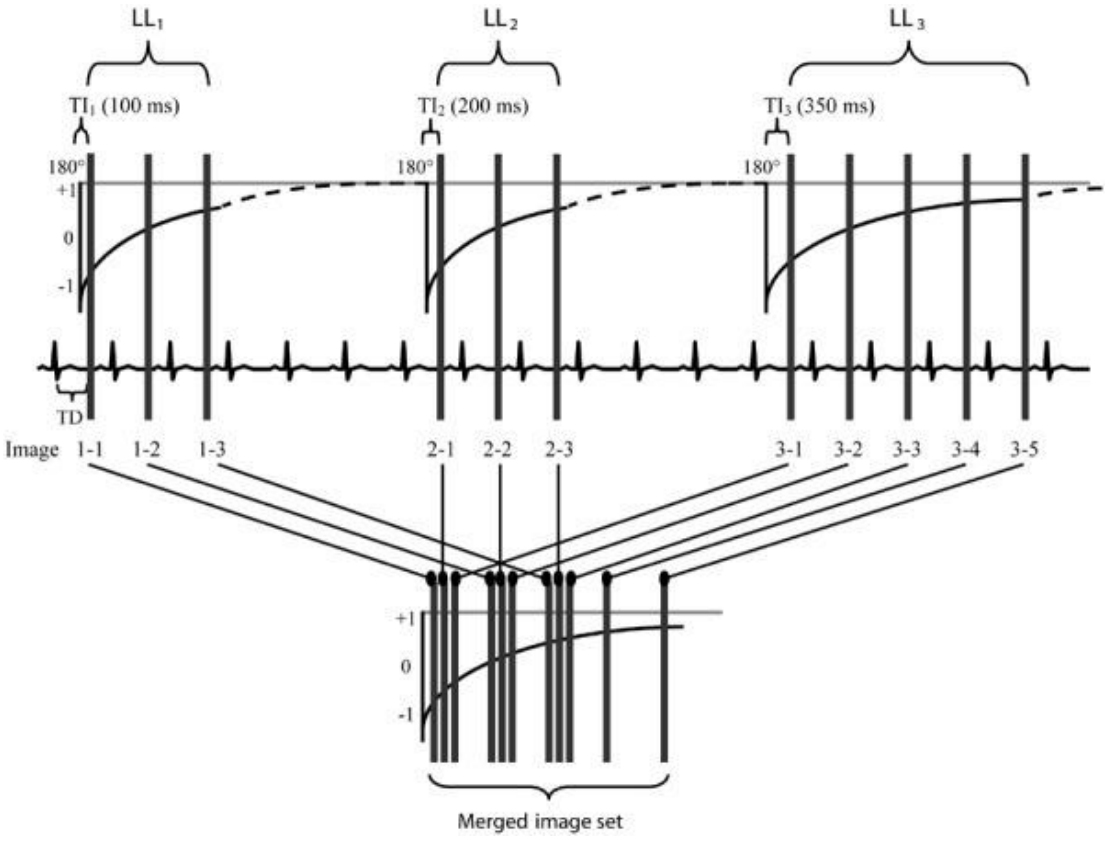

Figure 1-16 – Schematic diagram of the original MOLLI sequence. Eleven T1-weighted images are acquired and then regrouped according to the inversion time. Image from [11].

Saturation Recovery Single-Shot Acquisition (SASHA)

Saturation Recovery Single-Shot Acquisition (SASHA) is a saturation recovery sequence introduced in 2014 by Kelvin Chow et al. [12]. Saturation recovery sequences use 90º pulses (saturation pulses) instead of 180º pulses (inversion pulses), removing the magnetization memory and allowing a direct calculation of true T1s. SASHA applies ten single-shot SSFP readouts to acquire nine T1-weighted images and one proton density image. The proton density image is acquired at the start of the acquisition - without magnetization preparation. Next, the T1-weighted images are acquired with saturation times (TS) uniformly distributed in the RR interval. The saturation times are measured as the time between the saturation pulse and the centerline of the k-space. All images need to be acquired at the same place in the cardiac cycle.

A 3D version of SASHA (3D SASHA) was presented in 2017 by Giovanna Nordio et al. [18]. 3D SASHA is an adaptation of conventional SASHA, aiming to acquire 3D T1 maps of the whole volume of the heart in free breathing. In this way, 3D SASHA uses a 3D segmented k-space acquisition and a 1D hemidiagraphgmatic navigator for free-breathing acquisition. The sampling scheme of both SASHA sequences is reasonably similar; the most significant difference is that 3D SASHA acquires only eight T1-weighted images in order to decrease the acquisition time (**Figure 1-17**). For 3D SASHA, a recovery period of three heartbeats was used for the proton density.

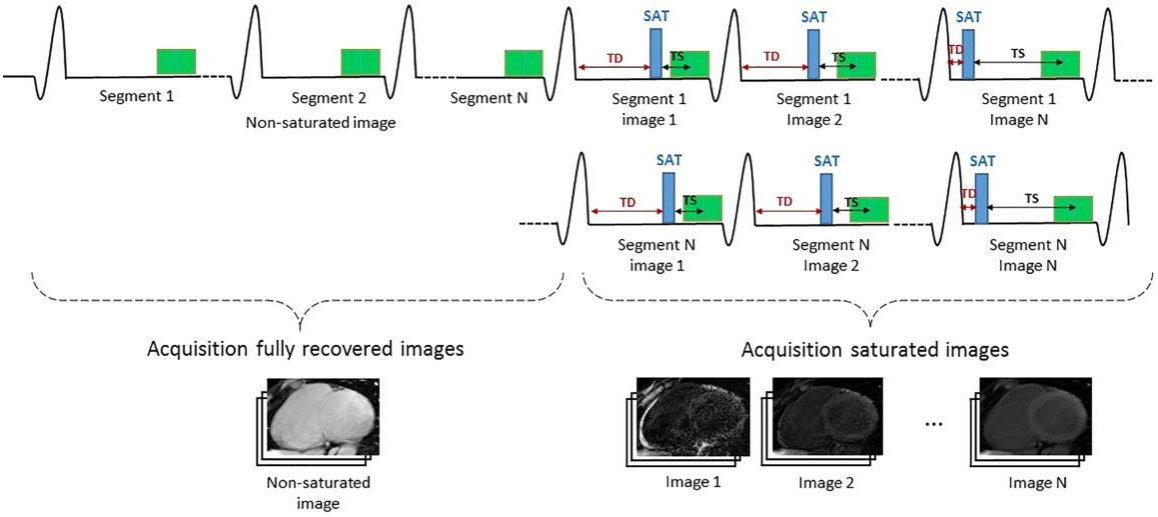

Figure 1-17 – Schematic of the 3D SASHA sequence. First, the proton density images (non-saturated) are acquired, followed by the acquisition of T1-weighted images with different saturation times (TS). Image from [18].

1.2.2. T2 mapping sequences

T2 mapping is very auspicious in detecting the myocardial water content, which is clinically relevant since edema is present in many cardiovascular conditions [27]. To this end, several sequences have been proposed and validated across the years. Although some sequences achieve good results, there are ongoing efforts to improve current T2 mapping sequences' performance on different diseases and their clinical applicability.

The gold-standard sequence to estimate the T2 relaxation time is the T2- turbo spin multi-echo sequence (T2-TSE). TSE sequence is based on the SE sequence and generates a train of echoes by applying a series of 180º pulses after the 90º pulse. The phase-encoding gradient is changed between echoes, which allows the acquisition of several lines of k-space in the same repetition time (TR) interval. The number of echoes in the same TR interval is the echo train length (ETL). The TSE sequence acquisition time is significantly shorter than the acquisition time of the conventional SE sequence. A variation of the SE sequence that can further decrease the acquisition time is the T2- gradient spin-echo (T2-GraSE).

Gradient spin-echo (GraSE)

Gradient spin-echo (GraSE) is a very rapid sequence with image contrast determined by T2, originally developed in 1991 by Koichi Oshio et al. [28]. Its applicability for myocardial edema quantification was demonstrated in 2015 by Rodrigo Fernández-Jiménez et al. [29]. Like the TSE sequence, GraSE consists of several 180º pulses applied after the 90º excitation pulse; however, it applies a series of gradient-echo readouts between the successive 180º pulses. The phase-encoding gradients are changed for each gradient-echo in order to sample the lines of k-space correctly (**Figure 1-18**). This technique can sample the k-space in a minimal number of excitations and decrease the acquisition time significantly. The T2 relaxation times obtained by T2-GraSE are comparable to the ones obtained by the reference T2-TSE [29], which shows that T2-GraSE is a reliable and faster alternative to T2-TSE.

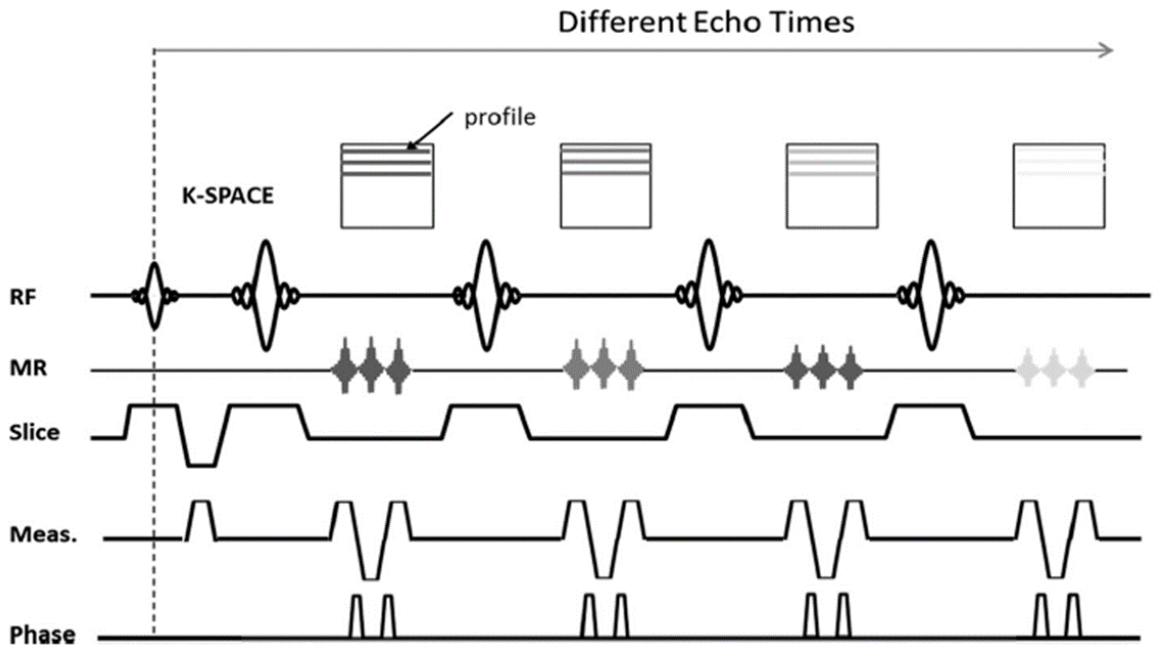

Figure 1-18 – General scheme of the GraSE sequence, a dark blood turbo spin-echo sequence. In these sequences, a few k-space lines are acquired in the same heartbeat for each image (multiple TEs), filling the k-space of every image progressively across the heartbeats. Image adapted from [29].

Some new 2D and 3D sequences try to estimate and quantify the absolute T2 values by fitting a certain number of images with different T2-weighting [30, 31]. In these sequences, each image is acquired independently at a separated heartbeat. They typically apply a preparation module with three or four T2-preparation pulses (T2prep), followed by an imaging part consisting of SSFP readouts. T2-preparation pulses have different echo times (TE) to acquire images with different T2 weightings. These echo times are typically uniformly distributed, from the non-T2-prepared image (TE = 0 ms) to the maximum TE allowed by the loss of signal (around 60 ms) (**Figure 1-19**).

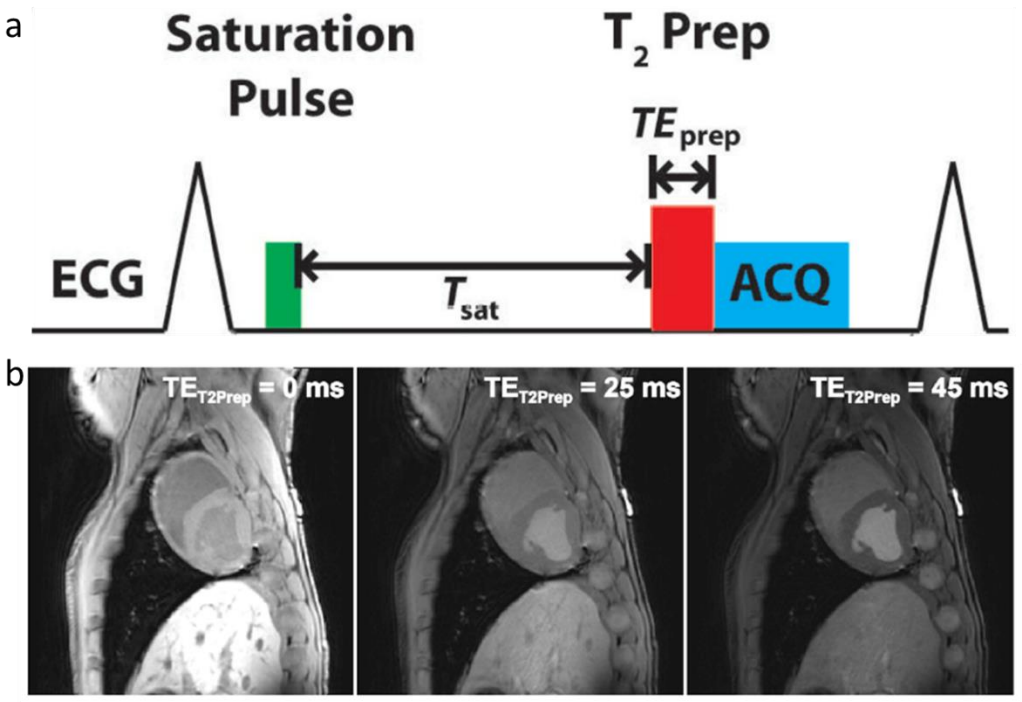

Figure 1-19 – Schematic illustration for bright blood T2 preparation pulse-based sequences. These sequences apply an additional magnetization preparation called T2-preparation pulse (a) to acquire images with a certain TE in order to sample the decay curve (b). Images adapted from [32] and [31].

1.2.3. T1/T2 mapping sequences

Cardiac parametric mapping (T1 and T2 mapping) has shown sensitivity to various cardiac diseases and has the potential to enhance the differentiation between normal and abnormal myocardium. Acquiring simultaneous, co-registered T1 and T2 3D maps increase imaging efficiency by providing complete coverage of the left ventricle and sensitivity to cardiac pathologies within a single acquisition. Obtaining cardiac T1 and T2 maps in a single scan can also boost and facilitate early diagnosis and treatment monitoring with CMR.

Several sequences have been developed to acquire T1 and T2 maps in a single scan. 3D-QALAS (3D-QuAntification using an interleaved Look-Locker Acquisition Sequence with T2 preparation pulse) is a 3D inversion recovery sequence based on spoiled Turbo Field Echo (TFE) [33]. 3D-QALAS performs interleaved T2 and IR prepared acquisitions; in more detail, it performs five acquisitions with T1 and T2 sensitizing phases to model the longitudinal magnetization and estimate the T1 and T2 values (**Figure 1-20**).

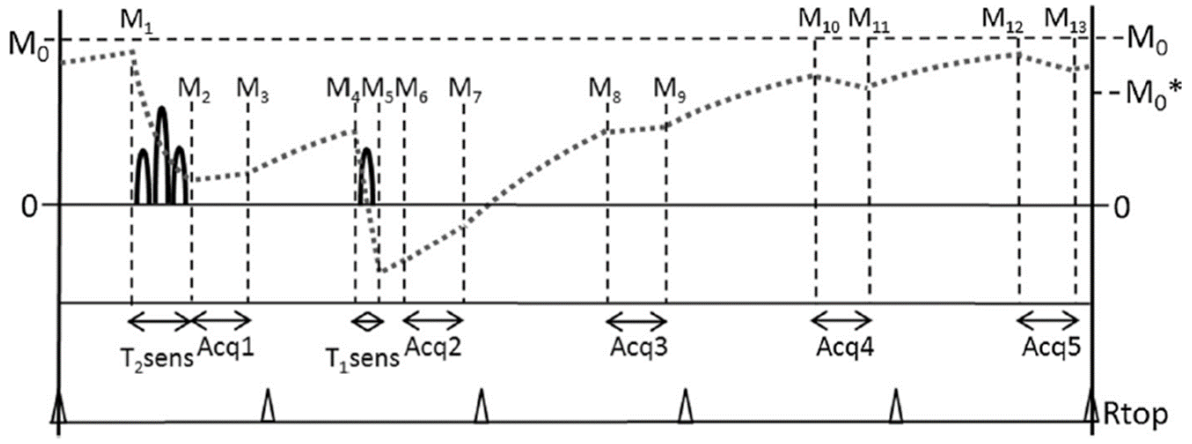

Figure 1-20 – Illustration of the 3D-QALAS acquisition scheme. Five images are acquired with the first image acquired after the T2 sensitizing phase and the remaining four images acquired after the T1 sensitizing phase. Image from [33].

Saturation recovery sequences are also used to acquire simultaneous myocardial T1 and T2 mapping, both in 2D [32] and 3D [34]. These sequences combine saturation pulses and T2-preparation pulses to acquire data to model the longitudinal magnetization using their specific signal model. In the work of Rui Guo et al. [34], T1 and T2 values were estimated separately with two different signal models (**Figure 1-21**), while in the work of Mehmet Akçakaya et al. [32], the approach was to use a combined signal model to fit the T1 and T2 values (**Figure 1-22**). The combined signal model is more robust than the two separated signal models, but the accuracy of T1 and T2 depends on each other, making the results more susceptible to modeling imperfections and causing bias on T1 due to the T2-preparation pulse.

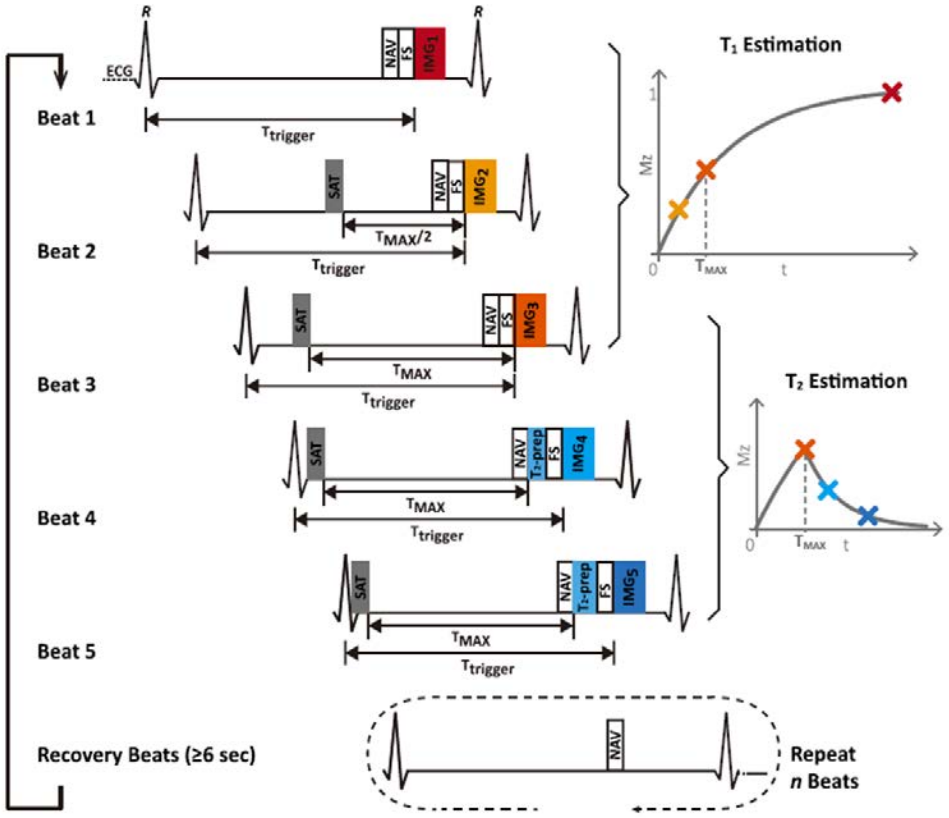

Figure 1-21 – Schematic diagram of the sequence presented in Rui Guo et al. [34]. Five separated images are acquired in an interleaved manner, with the proton density being the first image acquired (Beat 1). The first three images (Beat 1-3) are acquired without T2 preparation in order to estimate T1. The remaining two images (Beat 4-5) are acquired with T2-preparation pulses and a saturation time of TMAX in order to estimate T2. The image acquired without T2 preparation and a saturation time of TMAX (Beat 3) is used for both T1 and T2 estimation. Image from [34].

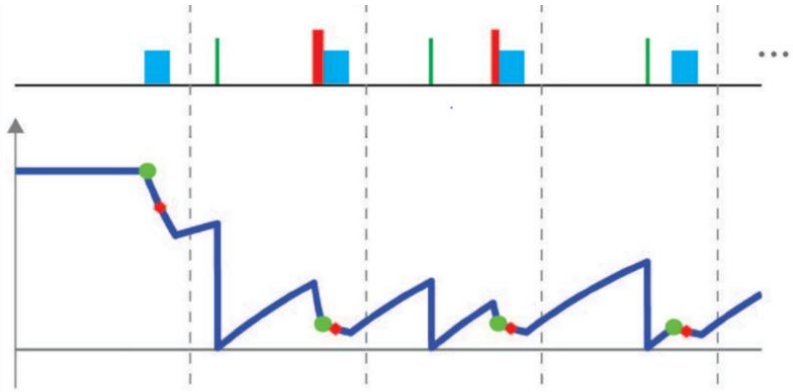

Figure 1-22 - Schematic diagram of the sequence presented in Mehmet Akçakaya et al. [32]. The first image acquired is the proton density – without T2 preparation. The remaining twelve images (three are shown) are acquired with different TS and T2-prep TE values. The SSFP imaging pulses effect is shown via the green and red circles in the longitudinal magnetization signal curve. The green circles mark the magnetization at the end of the T2 preparation pulses, while the red circles indicate the magnetization at the k-space center. Image adapted from [32].

1.3. Quantitative CMR: Mapping

The understanding of cardiomyopathies and myocarditis have improved considerably due to the widespread use of CMR. CMR provides a reliable way to visualize cardiac tissue, function, and morphology, improving therapy and prognosis and making it possible to identify the specific type of cardiomyopathy, which is frequently impossible without access to CMR. Although CMR is handy to assess cardiac function and morphology, it is the capability to characterize cardiac tissue that makes it indispensable for visualizing the tissue abnormalities related to cardiac diseases. For instance, the relaxation times are quite sensitive to changes in the myocardial tissue composition and can be quantified through T1 and T2 mapping. The quantification of the relaxation parameters is a fascinating application of CMR since it is a non-invasive way to evaluate disease severity and response to therapy.

Several T1 and T2 mapping sequences have been developed via combinations of pulse acquisitions with signal modeling in order to quantify the relaxation parameters accurately and obtain quantitative relaxation maps that provide pixel-wise information regarding the relaxation parameters. In this section, quantitative myocardial tissue imaging methods are described with a focus on signal modeling.

1.3.1. T1 mapping sequences

After acquiring a series of T1-weighted images that sample the T1 recovery curve, a theoretical signal intensity model is applied pixel-wise to fit the images into a T1 map, which can be described as a color-coded map of the heart displaying the fundamental tissue property T1 in milliseconds. Several T1 mapping sequences have been developed with innovative sampling strategies throughout the years and, consequently, requiring more complex signal models and post-processing. The main difficulties for computing reliable T1 maps are RR interval variability, through-plane cardiac motion, and respiratory motion artifacts. Nevertheless, the results can be improved by taking appropriate measures to improve the images before fitting. For example, T1 map quality can be improved by reducing respiration-induced motion using registration approaches such as non-rigid image registration [35].

Inversion recovery spin-echo (IR-SE)

Measuring T1 via IR-SE is a long process as several images with different TIs and long TR are required. Specifically, at least five images with different TIs should be acquired to estimate the T1 values correctly. Assuming a perfect inversion pulse, the signal (S) at each TI is given by

$$S(TI) = M_0\left(1 - 2e^{-\frac{TI}{T1}} + e^{-\frac{TR}{T1}}\right) \quad (1.2)$$

Where M0 is the net magnetization maximum value, TI is the inversion time, and TR is the repetition time. Assuming that the TR is at least five times longer than T1, allowing a full relaxation of the magnetization to M0, the signal equation can be approximated to

$$S(TI) = M_0\left(1 - 2e^{-\frac{TI}{T1}}\right) \quad (1.3)$$

This equation is the gold-standard to model the signal evolution of inversion recovery experiments for T1 mapping due to its simplicity.

Modified Look-Locker Inversion Recovery (MOLLI)

MOLLI was the first sequence to introduce pixel-wise mapping and obtain accurate T1 maps in a single breath-hold acquisition. It samples the inversion recovery curve for each pixel, acquiring T1-weighted images at multiple inversion times across different RR intervals. The inversion recovery curve follows a three-parameter signal (S) model given by

$$S(TI) = A - Be^{-\frac{TI}{T1^*}} \quad (1.4)$$

Where TI is the inversion time and T1* (apparent T1), A and B are the parameters for the 3-parameter model estimation. The steady-state free precession (SSFP) readout of MOLLI changes the inversion recovery curve by decreasing the equilibrium magnetization M0, making it impossible to acquire the correct T1 and, therefore, an apparent T1 (T1*) is acquired. In order to correct this imprecision, an equation based on a continuous readout using FLASH [36] is applied

$$T1 = T1^* \left(\frac{B}{A} - 1\right) \quad (1.5)$$

This approximation works exceptionally well for low flip angles and has been used over the years to estimate T1s with MOLLI.

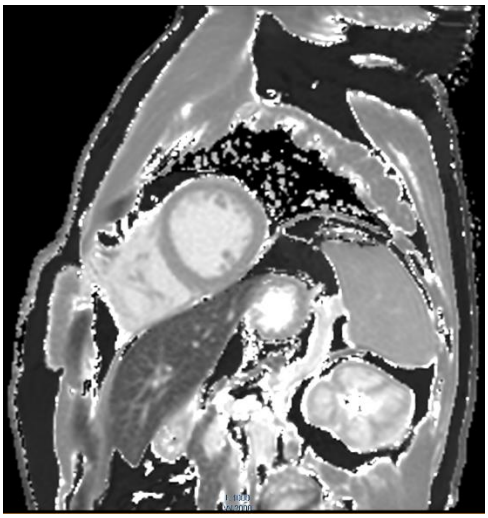

Figure 1-23 – Pre-contrast T1 map obtained with MOLLI. Acquisition time = 12 seconds.

Saturation Recovery Single-Shot Acquisition (SASHA)

SASHA acquires several images with different saturation times to sample the saturation recovery curve and perform a pixel-wise fitting. An image acquired with full magnetization (proton density) is required to estimate the T1s correctly. The T1 measured by SASHA is the real T1, which avoids some of the imprecisions of MOLLI. The saturation recovery follows a three-parameter signal S(t) model given by

$$S(TS) = A\left(1 - Be^{-\frac{(TS-\Delta)}{T1}}\right) \quad (1.6)$$

Where TS is the saturation time (time from the saturation pulse to the center of k-space), Δ is the time from the beginning of the readout to the center of the k-space, and T1, A (scaling factor) and B (saturation efficiency) are the parameters for the three-parameter model estimation. The three-parameter model takes into account that the saturation efficiency of the saturation pulse may not be ideal, which increases the accuracy. The drawback of counting with the saturation efficiency to estimate T1 is the loss of precision.

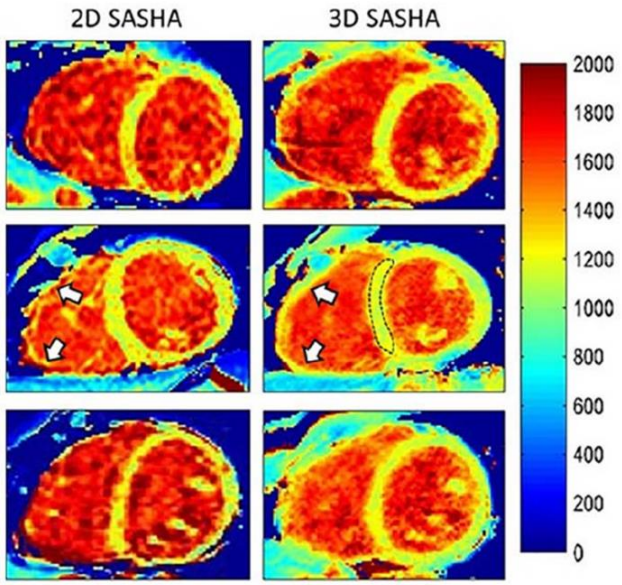

Figure 1-24 – T1 maps of three volunteers obtained with 2D SASHA and 3D SASHA. Acquisition time of 10 heartbeats and ±12 minutes, respectively. Image from [18].

1.3.2. T2 mapping sequences

Cardiac T2 mapping sequences are divided into two major types: i) bright blood T2 preparation pulse-based sequences and ii) dark blood turbo spin-echo sequences (TSE). The sequences of type ii) are TSE and GraSE sequences that acquire multiple echoes to sample the T2 curve. Sequences of type i) are more reproducible in-vivo and are getting more and more clinical recommendations [37]. In these sequences, images are acquired using T2prep pulses with different echo times for acquiring images with different T2 weightings, sampling the T2 curve. In both types, T2 mapping can be performed using a monoexponential decay model given by

$$S(t) = Ae^{-\frac{t}{T2}} \tag{1.7}$$

Where A is the scaling factor, and t is the echo time of the T2 preparation pulse for sequences of type i) and the echo time for sequences of type ii).

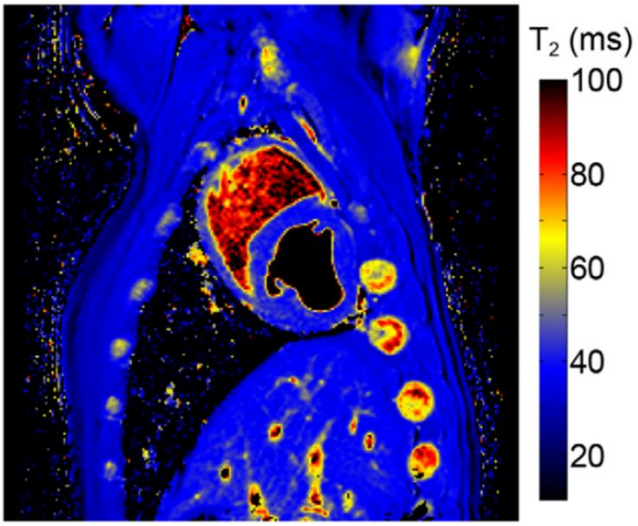

Figure 1-25 – T2 map slice obtained with a 3D T2-preparation pulse-based sequence. Acquisition time = 8.9 ± 1.9 min. Image from [31].

1.3.3. T1/T2 mapping sequences

Sequences for simultaneous myocardial T1 and T2 mapping have different approaches to sample the magnetization curves. 3D-QALAS calculates the T1 and T2 relaxation times from five measurements by simulating the longitudinal magnetization. The sequence calculates the magnetization of the images with multiple equations according to the theoretical effect of the T1 relaxation, RF pulse acquisition, and T1 and T2 sensitizing phases. In this way, a complex simulated magnetization evolution was used instead of the standard exponential models.

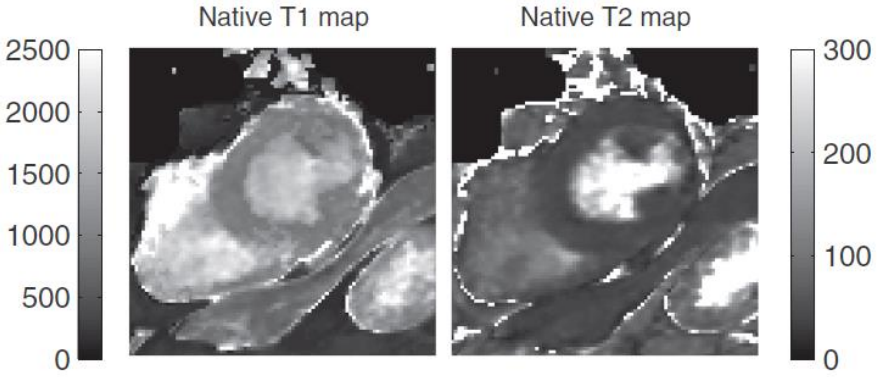

Figure 1-26 – Native T1 and T2 maps acquired simultaneously with 3D QALAS from a patient with a lateral myocardial infarction. Acquisition time = 15 heartbeats. Image from [33].

In the work of Rui Guo et al. [34], the approach of this 3D free-breathing sequence is to use the two standard exponential signal models to estimate T1 and T2. The relaxation parameters are estimated independently with two models: the two-parameter saturation recovery model for T1 and the monoexponential decay model for T2.

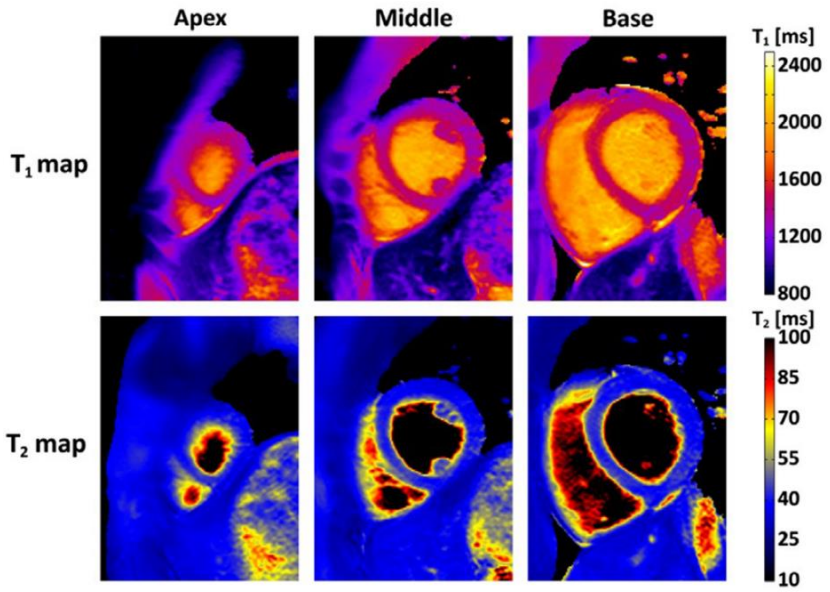

Figure 1-27 – Co-registered slices of T1 and T2 maps showing relaxation parameters estimated with the separated signal models approach. Acquisition time = 7.9 ± 1.4 min. Image from [34].

In the work of Mehmet Akçakaya et al. [32], the approach is to use a combined signal model. The magnetization evolution model is a 4-parameter model that characterizes the effect of the SSFP imaging pulses on the measured magnetization M

$$M(TS, T2P) = A\left(1 - e^{-\frac{TS}{T1}}\right)e^{-\frac{T2P}{T2}} + B \qquad (1.8)$$

Where TS is the saturation time, T2P is the T2 preparation time, A is associated with the signal at full-recovery (M0), and B is associated with the effect of the imaging pulses. The main drawback of a model with such amount of parameters is the loss of precision.

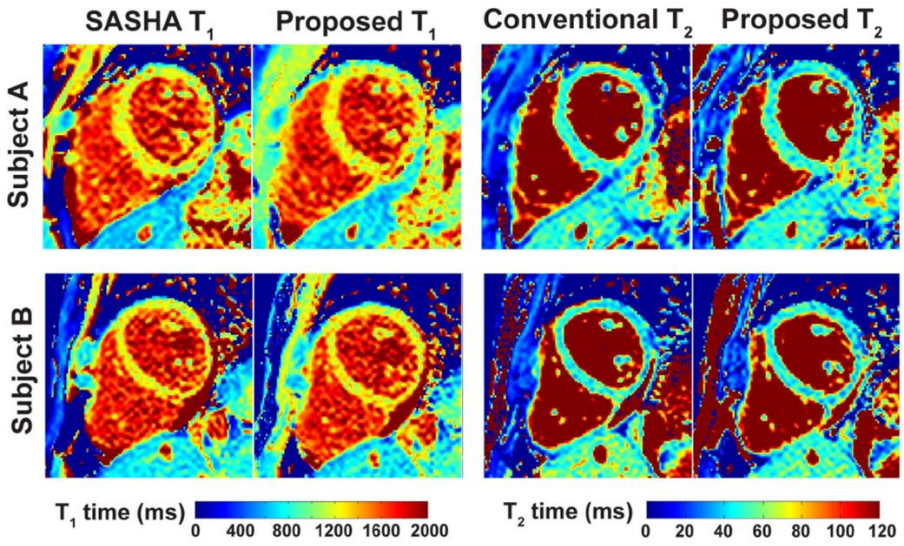

Figure 1-28 – T1 and T2 maps comparing the relaxation parameters estimated with the combined signal model approach against reference sequences. Acquisition time of the combined signal model sequence = 13 heartbeats. Image from [32].

1.4. Advanced techniques to improve MRI performance

In addition to the development of new pulse sequences, new techniques have emerged to accelerate acquisition. These techniques accelerate the acquisition by decreasing the amount of acquired data, allowing fast MR imaging. In this way, all these techniques have in common the exploitation of data redundancy by undersampling without significantly degrading the images. Currently, the three techniques that are the main workhorses in speeding up MR acquisitions are SENSitivity Encoding (SENSE) [38], generalized autocalibrating partially parallel acquisitions (GRAPPA) [39], and compressed sensing (CS) [40].

An alternative way to improve MRI performance is through the use of post-processing techniques. The quantitative relaxation maps provide pixel-wise information regarding the relaxation parameters, and post-processing techniques are helpful to improve the resolution and the SNR of the maps. State-of-the-art resampling algorithms and convolutional neural networks (CNNs) are major players nowadays in increasing image resolution and quality. The improvement of relaxation maps through post-processing techniques requires careful scrutiny since the pixels' values provide vital information and should remain unchanged.

In this section, some of the acceleration techniques that are nowadays used to reduce the acquisition time are described, and an introduction to super-resolution imaging and deep learning based super-resolution is provided.

1.4.1. Acceleration techniques

One of the main limitations of MRI is its long acquisition time in comparison with other imaging modalities. In this way, a considerable amount of effort has been put into developing techniques to accelerate the acquisition.

Parallel imaging techniques are a class of image reconstruction techniques that acquire a reduced number of k-space lines, decreasing the acquisition time considerably. Building on the development of phased array coils years earlier, SENSitivity Encoding (SENSE) was introduced in 1999 by Pruessmann et al. [38], being currently widespread clinically and enabling a reduction of acquisition time up to six times for 2D and nine times for 3D sequences [41]. SENSE is a parallel imaging reconstruction technique performed in the image domain that uses the receiver coil arrays' spatial information for reducing the number of phase-encoding steps.

Compressed sensing was introduced in 2006 by David Donoho [40], while in the same year, Emmanuel Candès et al. described a similar concept [42, 43]. One year later, Lustig et al. showed that compressed sensing can be applied to decrease the acquisition time of MR acquisitions [44], starting a never-ending period of research and breakthroughs in the topic. Compressed sensing can currently exploit the sparsity or compressibility of MR images and accelerate acquisition by undersampling without significantly degrading images. As most MR image information is contained in the k-space center, a variable density incoherently undersampling is applied with more sampling in the center than in the periphery (**Figure 1-29**). Compressed sensing has been successfully used in several applications, such as speeding up 3D cardiac imaging [45–47].

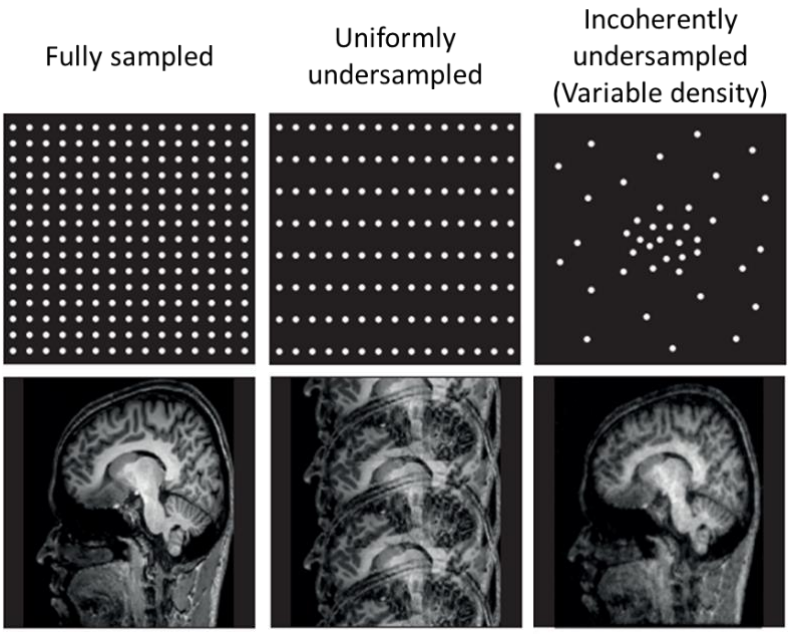

Figure 1-29 – Example of sample patterns and corresponding images. Image adapted from [41].

Compressed SENSE is built on compressed sensing and incorporates components of the parallel acquisition technique SENSE [38]. It solves an inverse problem with a sparsity constraint from data acquired using a balanced variable density incoherently undersampled k-space acquisition scheme with Poisson disc-style distribution. For reconstruction, the image is iteratively optimized according to the noise decorrelation, regularization, and coil sensitivities using a sparsity term based on wavelets transform [48, 49]. Compressed SENSE works in the spatial domain and can be applied in both phase-encoding directions for 3D imaging. Different regularization parameters/denoising levels can be used, varying from a maximum energy loss percentage of 0% to 30%. These regularization parameters establish the balance between data consistency, sparsity constraint, and noise reduction.

All in all, compressed SENSE combines parallel imaging, optimization of reconstruction speed, and automation. Studies showing the feasibility of compressed SENSE have recently been published for T1 calculation in the brain [48], cardiac cine imaging [50], and cardiac T1 mapping [51]. As expected, the method significantly reduced acquisition time, particularly in 3D acquisitions (**Figure 1-30**).

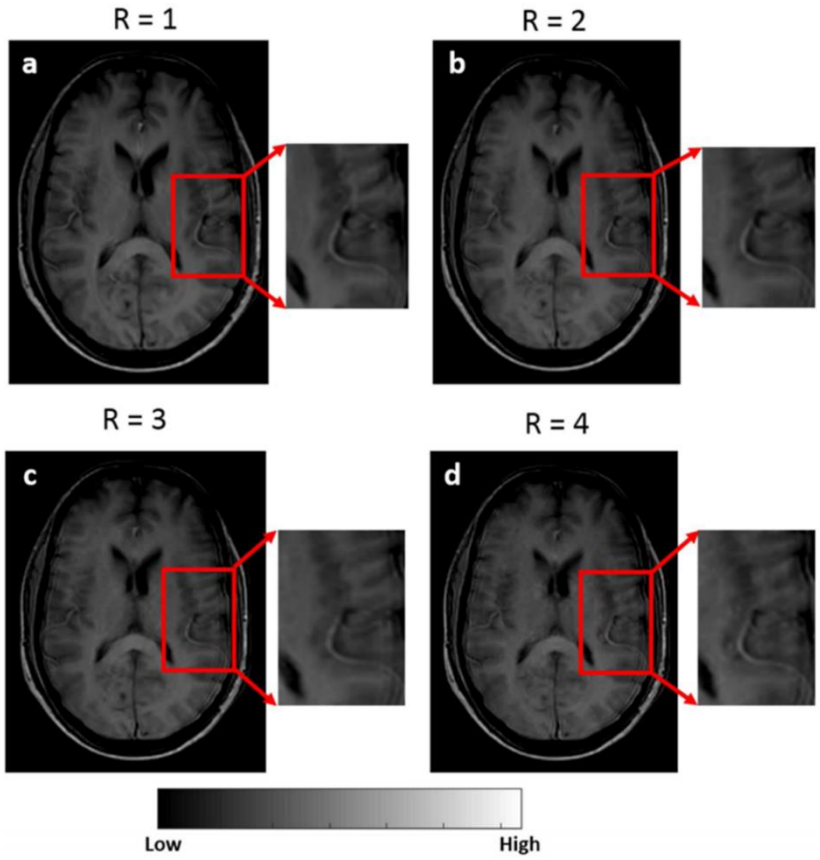

Figure 1-30 – Single slice T1-FFE images acquired with different compressed SENSE acceleration factors (R). The images show optimum quality for all acceleration factors. Image from [52].

1.4.2. Super-resolution imaging

Machine learning has been presented recently as a promising topic on cardiovascular magnetic resonance in many ways. Its applications go from image acquisition and reconstruction to image analysis and interpretation, as illustrated in **Figure 1-31**. Deep learning is a subfield of machine learning that has shown excellent results on topics such as natural language processing and computer vision. The development of powerful computer hardware and new optimized methods has contributed to the increasing deep learning usage. These new developments led to very deep neural networks (several layers) and optimized networks, such as convolutional neural networks for computer vision. Convolutional neural network (CNN) architectures are composed of multiple convolutional layers that process image data. Some of these architectures have been applied to super-resolution.

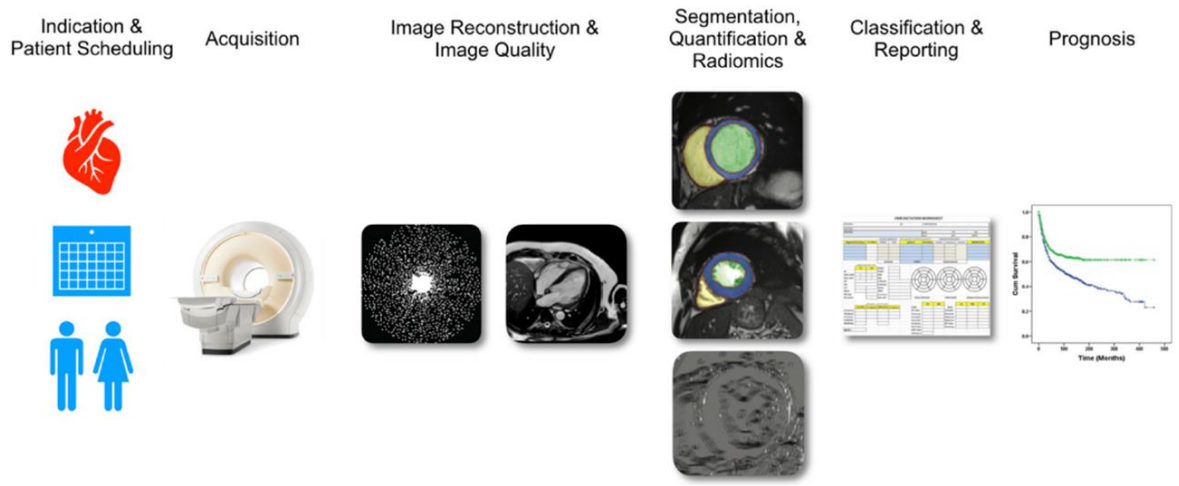

Figure 1-31 – Schematic showing the whole spectrum of CMR aspects that machine learning has the potential to highly contribute. Image from [53].

Super-resolution aims to obtain high-resolution images (HR) from low-resolution images (LR) of the same scene. A low-resolution image is, in general, characterized by having small spatial resolution (size) or being somehow degraded (e.g., blurring) and can be given by

$$LR = D(HR; \delta) \tag{1.9}$$

Where D is the degradation mapping function, and δ is the corresponding parameters of degradation, such as noise or the scaling factor. In this way, a degradation mapping function can be applied to convert an HR image to an LR image. The inverse is also possible if the degradation mapping function is available; however, this rarely happens in real-world applications, and a specific LR image can correspond to several possible HR images.

The traditional methods of image interpolation (scaling) that are widely used to resize images in real-world applications are nearest-neighbor, bilinear and bicubic interpolations, and Lanczos resampling [54]. When used for upsampling, these interpolation methods can increase image resolution (size); however, they have side effects (e.g., noise amplification and blurring) and only consider the information present in the input image. An alternative is to use deep learning-based super-resolution techniques. A vast number of deep learning techniques have been developed to obtain the best HR image from an LR image (**Figure 1-32**), using various types of network architectures and learning principles and strategies,

and achieving state-of-the-art performance on most super-resolution benchmarks and challenges [55].

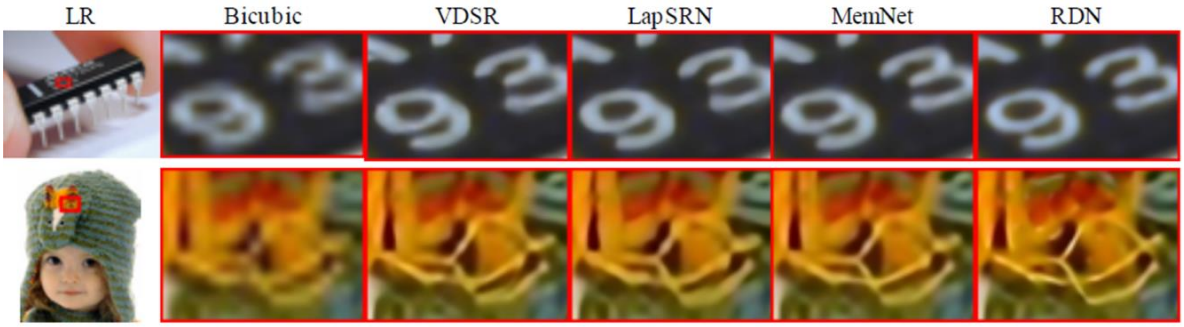

Figure 1-32 – Comparison of the visual results obtained by upsampling LR images (x4) with bicubic interpolation and four deep learning-based super-resolution techniques. Image from [56].

The deep learning techniques are commonly divided into supervised and unsupervised learning. Supervised learning is the most commonly used when there is access to the ground-truths of the training data. Unsupervised learning tries to discover structures through observation without access to the expected results, making the whole process more challenging. In supervised super-resolution models, the ground-truth (target) is the real HR image corresponding to the input LR image (commonly downsampled from the real HR image), and the model is trained with both low and high-resolution images. In general, these models are complex combinations of components such as network architecture, model frameworks, upsampling methods, and learning strategies [55]. The most mainstream network architectures are based on model frameworks of post-upsampling super-resolution in order to compute mostly in low-dimensional space (**Figure 1-33**).

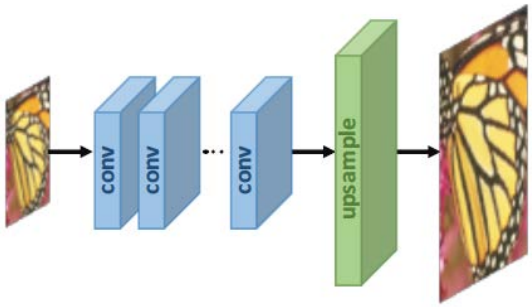

Figure 1-33 – Post-upsampling super-resolution model framework. Image adapted from [55].

Regarding network design strategies, there is a massive amount applied to super-resolution. Two of the most mainstream and more relevant to this work are residual learning [57] and dense connections [58]. Networks based on residual learning learn residuals instead of detailed mapping, while networks with dense connections have as the input of the layers all the features maps of all the previous layers (**Figure 1-34**).

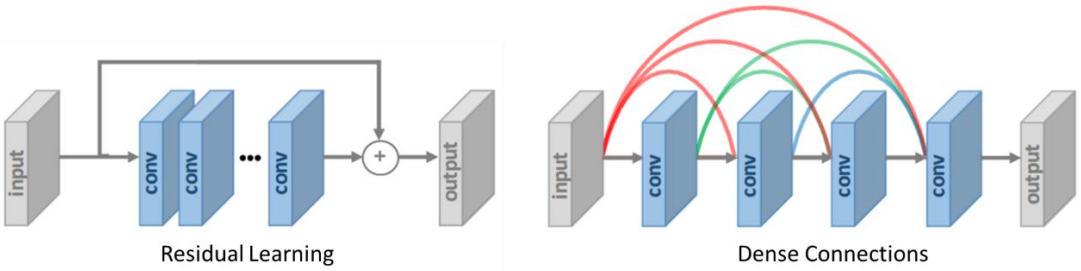

Figure 1-34 – Residual learning and dense connections network design strategies. Image adapted from [55].

Residual Dense Network (RDN)

A very deep CNN known as Residual Dense Network (RDN) was introduced in 2018 by Zhang et al. [56]. This network combines the aforementioned model framework and network design strategies to fully use the original LR image hierarchical features and achieve state-of-the-art performance. In other words, this network can make full use of all the local and global features of the image and has shown an excellent performance against state-of-the-art methods on benchmark datasets (**Figure 1-35**).

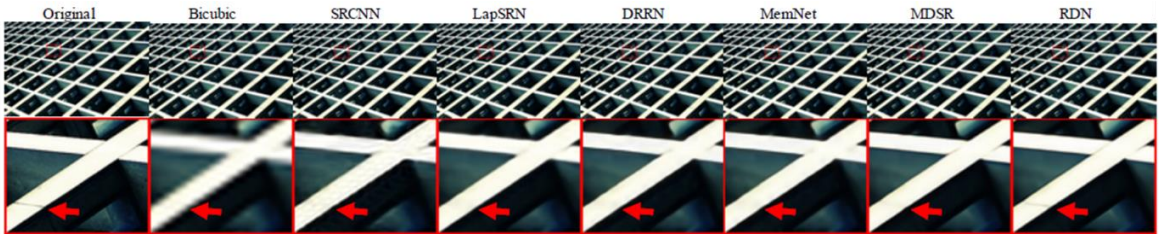

Figure 1-35 - Comparison of the visual results obtained by upsampling LR images (x4) with the RDN and with the bicubic interpolation and five other deep learning-based super-resolution techniques. Image adapted from [56].

Overall, the RDN architecture consists of four main sections: i) the shallow feature extraction net, ii) the residual dense blocks (RDB), iii) the dense feature fusion, and iv) the upsampling net. In i), the first two convolutional layers extract the shallow features; in ii), the set of residual dense blocks is the most critical section and extracts mostly local features; in iii), a dense feature fusion consisting of global feature fusion and global residual learning is performed; and in iv), an upsampling net is applied since the extracted features are in the LR space. The RDN and RDB architectures are illustrated in **Figure 1-36**.

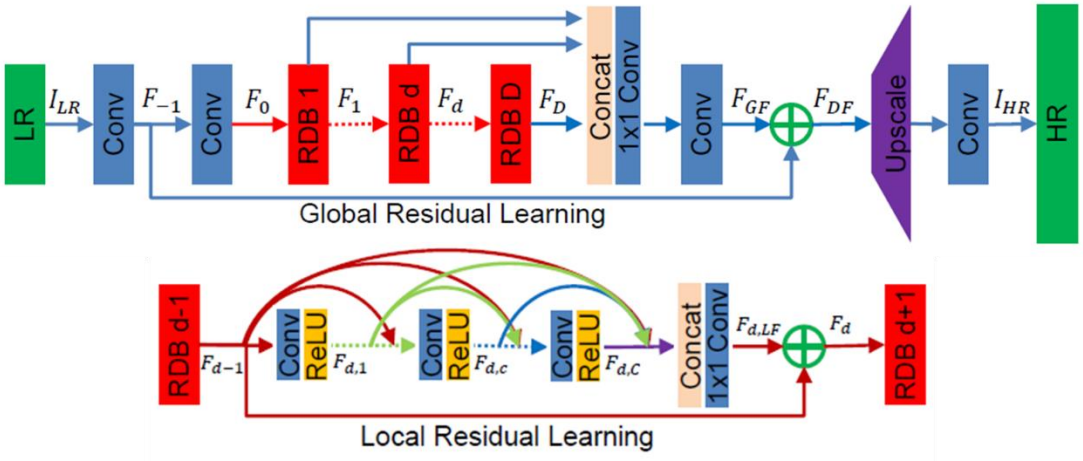

Figure 1-36 – Residual Dense Network (RDN) architecture (top row) and residual dense block (RDB) architecture (bottom row). Image adapted from [56].

CHAPTER 2

MOTIVATION AND OBJECTIVES

2.1. Motivation

Cardiovascular disease (CVD) is the most common cause of death in the European Society of Cardiology's (ESC) fifty-seven member countries. Considering the most recent year of available data per country, the number of deaths by CVD was 2.2 million in females and 1.9 million in males (**Figure 2-1**), which represents 47% and 39% of all deaths, respectively. Within the CVD deaths, coronary heart disease (ischaemic heart disease) is the most common cause, accounting for 38% in females and 44% in males of CVD deaths [59].

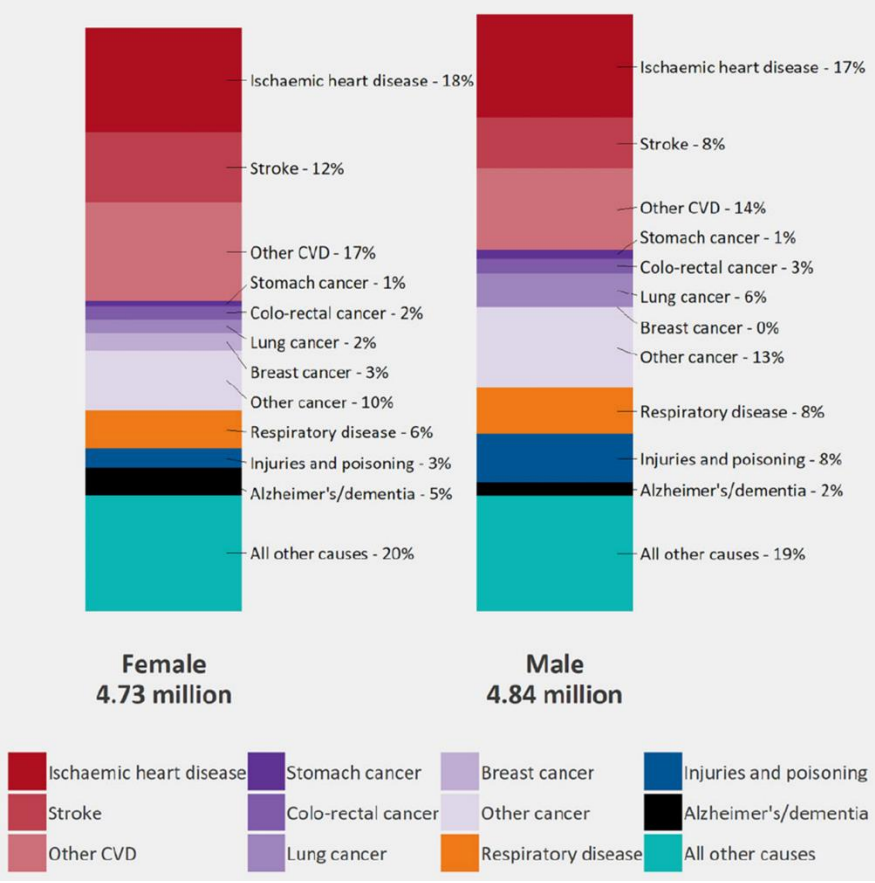

Figure 2-1 – Cause of deaths in the ESC member countries (excluding Algeria, Lebanon, Libya, and the Republic of Kosovo). Data from the WHO and image from [59].

Although CVD is still by far the most common cause of death overall, the significant improvements in the prevention and treatment of CVDs have made cancer the most common cause of death in a few countries. Some of these countries include the Netherlands, the United Kingdom, and Denmark for females and Portugal, Spain, and France for males [59].

The continuous cutting edge research on CMR has been one of the factors that led to such an improvement in the prevention and treatment of CVDs. CMR is becoming an indispensable tool in cardiovascular medicine by acquiring data about anatomy and function simultaneously. Furthermore, it allows the non-invasive characterization of myocardial tissues via parametric mapping techniques. Parametric mapping techniques provide a spatial visualization of quantitative changes in the myocardial parameters, which improves patient care and treatment by allowing better diagnostic decision making. All in all, parametric mapping provides unique and essential information about the myocardium and is a significant player towards precision medicine. Due to its diagnostic and prognostic usefulness, parametric mapping techniques should be applied in the clinical diagnostic assessment of all patients with heart failure [37].

On the technical side, parametric mapping sequences using new developments such as 3D acquisition, parallel imaging, compressed sensing, and artificial intelligence aim to provide new ways to decrease the acquisition time, improve the spatial resolution, and increase the coverage of the heart. These novel sequences are essential for the standardization of data acquisition and post-processing, and optimization of workflows, which are most likely the next significant future developments in cardiac mapping applicability [37]. In order to turn this into reality, there is the need to develop novel 3D parametric mapping sequences capable of obtaining T1 and T2 values in the shortest acquisition time possible (preferentially in a single breath-hold) without considerably compromising accuracy and precision.

With this in mind, we introduce a new single-breath hold MR methodology by developing and optimizing new parametric mapping sequences capable of obtaining accurate 3D parametric maps in a single breath-hold at 3T. Firstly, we propose and validate the 3D saturation-recovery compressed SENSE rapid acquisition (3D SACORA) imaging sequence, a new single breath-hold 3D T1 mapping technique at 3T. Secondly, we redesign the sequence to test the feasibility of adding the acquisition of T2-weighted images to 3D

SACORA in order to acquire co-registered T1 and T2 3D maps in a single breath-hold, proposing the 3D dual saturation-recovery compressed SENSE rapid acquisition (3D dual-SACORA) imaging sequence. Lastly, we implement a deep learning-based post-processing method (residual dense network) to improve the image quality of the cardiac T1 maps without compromising the correct estimation of T1 values.

2.2. Objectives

This thesis's general objective is to introduce an accurate and efficient 3D single breath-hold MR methodology for measuring cardiac parametric mapping on a 3T clinical scanner. To this purpose, the specific objectives are:

- Research and development of a new 3D T1 saturation recovery mapping technique (3D SACORA) to acquire the entire left ventricle in a single breath-hold at 3T. This approach aims to achieve good quality single breath-hold saturation recovery 3D T1 mapping and stability over a wide range of heart rates (HRs). To meet this objective, a novel acquisition scheme based on pre-pulses and TFE acquisitions is developed to characterize tissue accurately in a very short acquisition time. The novel single breath-hold 3D T1 mapping sequence is validated with phantom and in-vivo experiments. Furthermore, the gold standard saturation recovery sequence 3D SASHA is implemented to serve as a reference.
- Test the feasibility of adding a T2 mapping feature to the 3D SACORA sequence without substantially increasing the acquisition time. Acquiring simultaneous, co-registered T1 and T2 3D maps increases imaging efficiency and improves specificity to different cardiac pathologies. In this way, a modified 3D SACORA sequence called 3D dual-SACORA is proposed to acquire simultaneously 3D T1 and T2 maps while keeping the acquisition time within a single-breath-hold. Experiments in phantom and in-vivo are performed to assess the feasibility of this joint 3D T1/T2 approach.
- Research and implementation of a post-processing method to improve the T1 maps obtained with the 3D SACORA sequence. Although this sequence acquires good quality T1 maps, we hypothesize that artificial intelligence techniques can be applied to improve the T1 maps without compromising the correct estimation of T1 values.

In this way, a residual dense network (RDN) is trained with several high-resolution images with the final goal of improving the resolution and decreasing the noise of the T1 maps. The trained network is compared with the state-of-the-art Lanczos resampling to evaluate its performance on upsampling the T1 maps obtained by 3D SACORA and 3D SASHA.

CHAPTER 3

MATERIALS AND METHODS

3.1. Single breath-hold saturation recovery 3D cardiac T1 mapping via compressed SENSE

3.1.1. Pulse sequence design

The 3D saturation-recovery compressed SENSE rapid acquisition (3D SACORA) pulse sequence was designed to acquire the entire left ventricle in a single breath-hold while achieving good quality T1 mapping and stability over a wide range of heart rates (HRs).

3D SACORA consists of three distinct blocks (**Figure 3-1**). The sequence begins with proton density (PD) images to avoid T1 effects from prior saturation pulses (first block). Full signal recovery is ensured by waiting a minimum of 6 s between the PD readouts [19, 34]. The second block consists of images acquired at saturation time (TS) 1 and at TS1+RR interval (TS3). Finally, the third block of images is acquired at TS2 and at TS2+*n*RR intervals (TS4). T1 estimation is optimized not only by the PD images, but also by the selection of the acquired saturation time images [60]. TS1 is set to 250 ms to acquire the shortest possible saturation image while maintaining an adequate SNR. For most heart rates, TS2 is set to 500 ms to allow a TS4 similar to the native cardiac T1 (1500 ms at 3T). For high heart rates that make a 500-ms TS2 unfeasible, the sequence automatically computes the longest possible TS2 according to the RR interval derived from the heart rate defined by the user in the acquisition protocol.

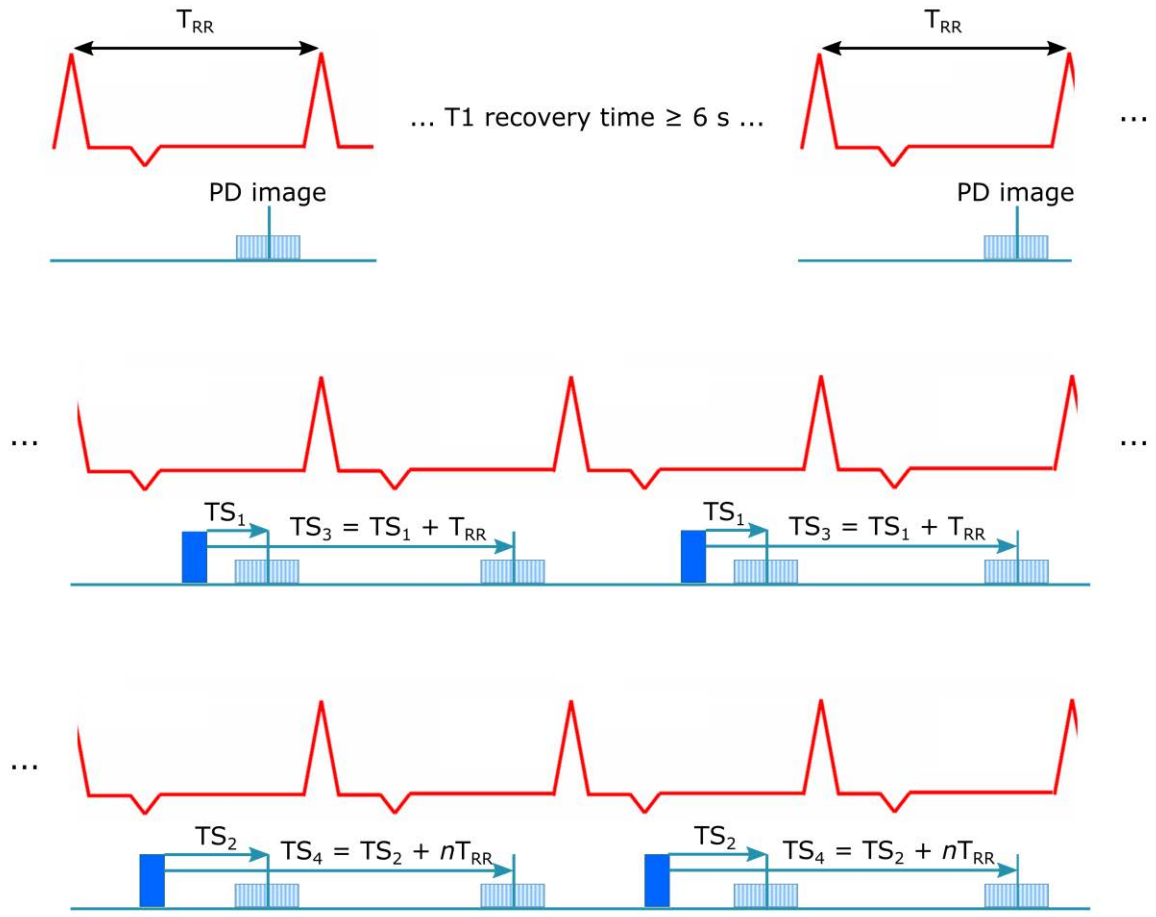

Figure 3-1 - 3D SACORA pulse sequence. The sequence performs two turbo field echo (TFE) shots for each 3D image: in the PD image block (first row), the two TFEs are separated by a minimum 6 s magnetization recovery; two images are acquired at TS1 and TS3 (second row); and two images are acquired at TS2 and TS4 (third row). TS1 = 250 ms, TS2 = 500 ms (if allowed by the HR), TS3 = TS1 + RR interval, TS4 = TS2 + *n*RR intervals (*n* depending on HR).

TS1 and TS2 ensure consistent sampling at the low saturation time area of the T1 relaxation curve for both low and high heart rates. TS3 is always acquired at the RR interval immediately after TS1, whereas TS4 is calculated to allow acquisition as close as possible to 1500 ms; therefore, TS4 is acquired after *n* recovery heartbeats computed according to the heart rate. In this way, the design ensures sampling close to the T1s of interest and that TS3 and TS4 are unconstrained by high heart rates, as shown in **Table 3-1.**

TS (ms) / HR (bpm)	TS1	TS2	TS3	TS4
40	250	500	1750	2000
50	250	500	1450	1700
60	250	500	1250	1500
70	250	500	1106	1356
80	250	498	1000	1248
90	250	423	916	1756
100	250	363	850	1563
110	250	314	795	1405
120	250	273	750	1273

Table 3-1 - Table with the sampling strategy of the saturation times of 3D SACORA for different heart rates (40 – 120 bpm). The saturation times change with the heart rate to cover the low saturation time area of the T1 relaxation curve and to ensure sampling close to the T1s of interest.

3D SACORA uses a spoiled linear turbo field echo (T1-TFE) acquisition (TR/TE/FA = 2.8ms/1.32ms/5°). The 3D sequence covers a volume of 322x322x60 mm with an in-plane resolution of 2.0x2.0 mm and a slice thickness of 10 mm reconstructed to 5 mm (12 slices). Composite radiofrequency (RF) pulses are used to achieve homogeneous saturation across different T1 values [61, 62]. Full image acquisition is accelerated using a k-space shutter and a spatial domain compressed SENSE factor of 4.5 in order to acquire a whole 3D volume in 2 independent TFE shots of echo train length of 76. In this study, compressed SENSE was applied in the spatial domain in both phase-encoding directions with a fixed regularization parameter (maximum energy loss percentage equal to 30%) to keep a good balance between data consistency, sparsity constraint, and noise reduction. The effect of different compressed SENSE factors (1.5, 3, and 4.5) is shown in **Figure 3-2**, and the effect of different regularization parameters/denoising levels is shown in **Figure 3-3**.

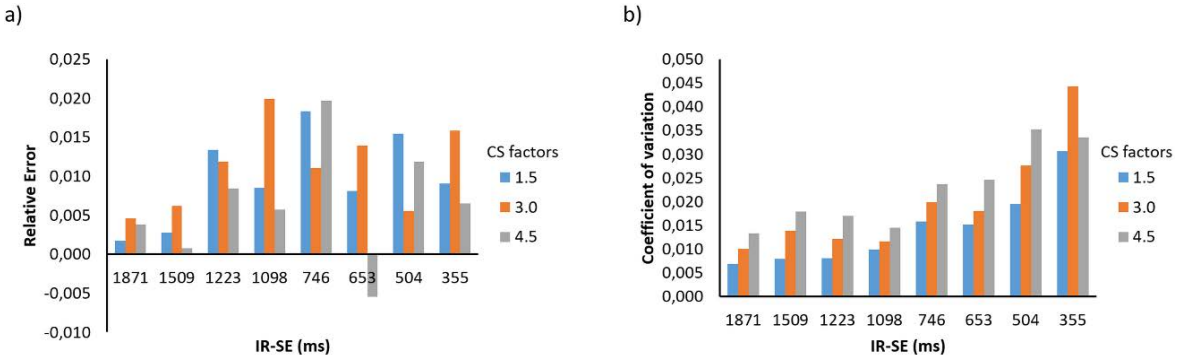

Figure 3-2 - Phantom acquisitions with a simulated heart rate of 60 bpm, showing a) the accuracy and b) precision of 3D SACORA for different compressed SENSE factors (1.5, 3, and 4.5).

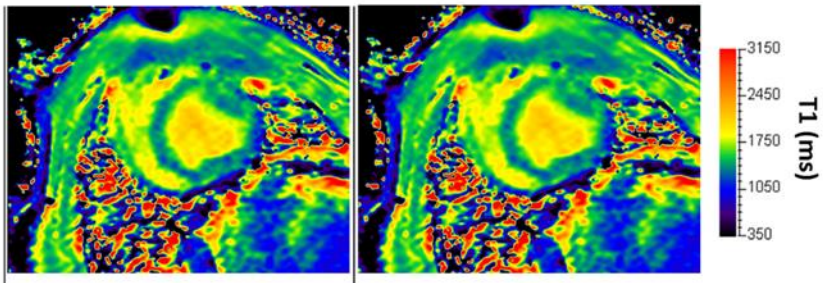

	a	b
Denoising level:	**Medium**	**Strong**
T1 Myocardium (ms):	1375 ± 62	1383 ± 56
T1 Blood (ms):	2100 ± 96	2103 ± 83

Figure 3-3 - The effect of different regularisation parameters levels on the estimated T1 maps with two different regularization factors: a) medium (maximum energy loss percentage, 15%) and b) strong (maximum energy loss percentage, 30%).

3.1.2. Image processing

For 3D SACORA, T1 values are estimated by bounded Levenberg-Marquardt fitting using Bloch equations [12]. All sampling points are corrected according to the linear readout, and sampling points TS3 and TS4 are further corrected for the magnetization distortion caused by the readout effects of TS1 and TS2, respectively [63–65]. The T1 curves are fitted to a three-parameter (T1, α, and M0) relaxation model following the signal model described in

Figure 3-4. The signal model considers the signal recovery after the saturation pulse and the signal evolution derived from the excitation pulses during the data acquisition. For instance, the magnetization evolution for the pair TS2 - TS4 is given by

$$M1 = M0\left(1 - \alpha\, e^{\frac{-\left(TS2 - \frac{T_{acq}}{2}\right)}{T1}}\right) \tag{3.1}$$

$$M2 = M0^{*} - (M0^{*} - M1)e^{\frac{-\frac{T_{acq}}{2}}{T1^{*}}} \tag{3.2}$$

$$M3 = M0^{*} - (M0^{*} - M2)\, e^{\frac{-\frac{T_{acq}}{2}}{T1^{*}}} \tag{3.3}$$

$$M4 = M0 - (M0 - M3)\, e^{\frac{-(TS4 - TS2 - T_{acq})}{T1}} \tag{3.4}$$

$$M5 = M0^{*} - (M0^{*} - M4)\, e^{\frac{-\frac{T_{acq}}{2}}{T1^{*}}} \tag{3.5}$$

Where TS2 and TS4 are the saturation times, T_{acq} is the TFE shot length, and α is the saturation pulse efficiency. T1* and M0* are the apparent T1 and the magnetization during signal readout using spoiled TFE acquisition and are given by

$$T1^{*} = \frac{1}{\frac{1}{T1} - \frac{1}{TR} ln(cos\theta)} \tag{3.6}$$

$$M0^{*} = M0\frac{TR}{TR - T1\ln(\cos\theta)} \tag{3.7}$$

Where TR is the repetition time and θ is the flip angle.

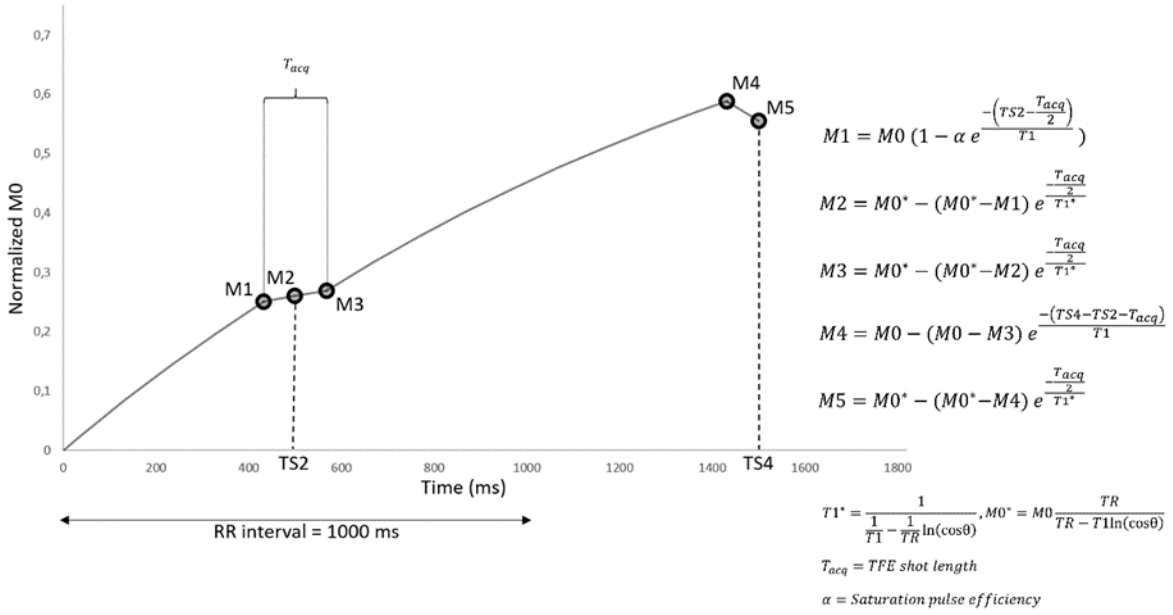

Figure 3-4 - Schematic representation of the magnetization evolution during a 3D SACORA acquisition. M1, M2, M3, M4, and M5 take into account signal recovery after saturation pulse as well as the signal evolution derived from excitation pulses during data acquisition for a single pair of saturation times (TS2 and TS4). T1* and M0* represent the apparent T1 and the magnetization during signal readout using spoiled turbo field echo acquisition. TR = repetition time, θ = flip angle, α = saturation pulse efficiency.

Fitting algorithm and T1 map generation are integrated into the scanner reconstruction pipeline; therefore, the parametric T1 maps for the entire 3D volume are available shortly after acquisition.

3.1.3. Validation

All studies were performed with a Philips Achieva 3T-Tx magnetic resonance imaging (MRI) scanner (Philips Healthcare, Best, the Netherlands) using a 32 channel cardiac coil. The acquisition parameters and T1 maps generation methodology were optimized for in-vivo acquisition and validated with phantom experiments.

Phantom validation

The precision and accuracy of 3D SACORA were assessed in phantom experiments. The phantom consisted of eight tubes filled with distilled water and different concentrations of an MR contrast agent (Dotarem, Guerbet, Paris, France) selected to obtain T1s spanning the range from 355 ms to 1871 ms.

Reference T1 values were obtained using an inversion-recovery spin-echo (IR-SE) sequence with a repetition time of 15 s and 15 inversion times ranging from 100 to 3500 ms. Other sequence parameters were slice thickness = 10 mm and TE = 18 ms. Each image was acquired in approximately 11 minutes.

In order to further validate 3D SACORA T1 estimation accuracy and precision, T1 values were also estimated using an in-house version of 3D SASHA [18]. This 3D SASHA variant used a linear spoiled T1-TFE readout without any respiratory trigger for phantom and in-vivo experiments. In addition to the PD image, eight equally spaced saturation time images were acquired, starting from a minimum saturation time of 120 ms to a maximum saturation time dependent on the heart rate – 709 ms in case of a heart rate of 60 bpm. PD recovery beats were computed automatically according to the heart rate so as to achieve a minimum T1 recovery time of 6 s. Other protocol characteristics were TR/TE/FA = 2.8ms/1.3ms/12°; slice thickness = 10 mm, reconstructed to 5 mm (12 slices); spatial domain compressed SENSE factor = 1.8; in-plane resolution = 2x2 mm; cartesian radial k-space filling; and echo train length = 30. For a heart rate of 60 bpm, the acquisition time was approximately 3 minutes. The bounded three-parameter relaxation model-fitting algorithm and the T1 map generator were integrated into the scanner reconstruction pipeline.

T1 values (mean ± standard deviation) were measured from manually drawn regions of interest (ROIs) in the generated T1 maps.

Passing-Bablok regression and Bland-Altman plots were used to compare the three sequences. The Passing-Bablok regression [66] is a useful statistical procedure to estimate the agreement and bias between two analytical methods, being robust and reasonably insensitive to data outliers. The Bland-Altman plot [67] is a widespread method to assess the

agreement between two analytical methods, making it simple to visualize the differences between the methods' measurements.

To explore the sensitivity of the proposed methodology to heart rate, images were acquired with 3D SACORA and 3D SASHA at simulated heart rates ranging from 50 to 120 bpm. The estimated T1s were then compared against the T1 reference values obtained with IR-SE. As described before, both sequences automatically calculated the PD recovery beats, ensuring the acquisition of fully recovered PD. Furthermore, the TS4 in 3D SACORA was automatically adjusted according to the heart rate to ensure acquisition within the range of T1 values of interest. The precision and accuracy of this approach were measured by the coefficient of variation

$$CV = \frac{SD}{M} \tag{3.8}$$

and relative error

$$RE = \frac{M_{proposed\ Method} - M_{reference\ Method}}{M_{reference\ Method}} \tag{3.9}$$

Where SD is the standard deviation inside the ROI, M is the average value inside the ROI, and reference method is the T1 map obtained from the IR-SE acquisition.

In-vivo validation

Seven large white castrated male healthy pigs (mean weight, 40 kg) were scanned with 3D SACORA and 3D SASHA. During 3D SACORA pre-contrast acquisition, the mean heart rate was 73 bpm (range, 55 to 83 bpm). In all pigs, images were acquired before and after administration of MR contrast agent. Scans were carried out under free-breathing conditions. No respiratory navigator approach was implemented because abdominal respiration in pigs produces little chest movement under free-breathing conditions.

The study protocol was approved by the local institutional Animal Research Committee and conducted conforming to the recommendations of the Guide for the Care and Use of Laboratory Animals.

Bulls-eye plots of T1 and coefficient of variation were generated from 3D SACORA and 3D SASHA data according to the American Heart Association (AHA) standard 17-segment model of the LV. For both techniques, the central segment was used to report blood values. The segment values used were the mean values of the seven pigs. These plots were used to provide information about myocardium homogeneity and give a 3D perspective on the estimated T1s.

For 3D SACORA and 3D SASHA, septal T1 values (mean ± standard deviation) were measured from ROIs manually drawn on the septal myocardium. These measurements were used to compare the septal T1 values and coefficient of variation obtained by both sequences.

3.1.4. Joint T1 and T2 mapping – feasibility study

In this section, the acquisition scheme of 3D SACORA is modified to obtain T1 and T2 maps in a single breath-hold in order to test the feasibility of developing a sequence based on 3D SACORA for T1/T2 mapping.

Pulse design and signal model

As the first step, simple modifications to the acquisition scheme of 3D SACORA were performed. The resulting acquisition scheme can be divided into three blocks (**Figure 3-5**). In the first block, the proton density images (PD) are acquired to avoid effects from previous saturation pulses. The second block consists of the acquisition of TS1, TS2, and TS2+RRinterval (TS3). TS1 is set to 250 ms. TS2 is the maximum saturation time allowed by the heart rate and is used for T1 and T2 (T2- prep echo time = 0 ms) estimations. TS3 is calculated to be always acquired as close as possible to the native cardiac T1 (1500 ms at 3T), and therefore the amount of recovering beats changes according to the heart rate. The third block is focused on the T2 mapping part of the acquisition. Here, two T2-weighted images are acquired using T2- preparation pulses with echo times of 23 and 50 ms. Thus, there is one less T1-weighted image and two new T2-weighted images in comparison with the T1 mapping scheme of 3D SACORA, resulting in an acquisition time of 17 RR intervals

(for HR=60 bpm). The relaxation parameters are estimated independently with the 3D SACORA model for T1 and the monoexponential decay model for T2.

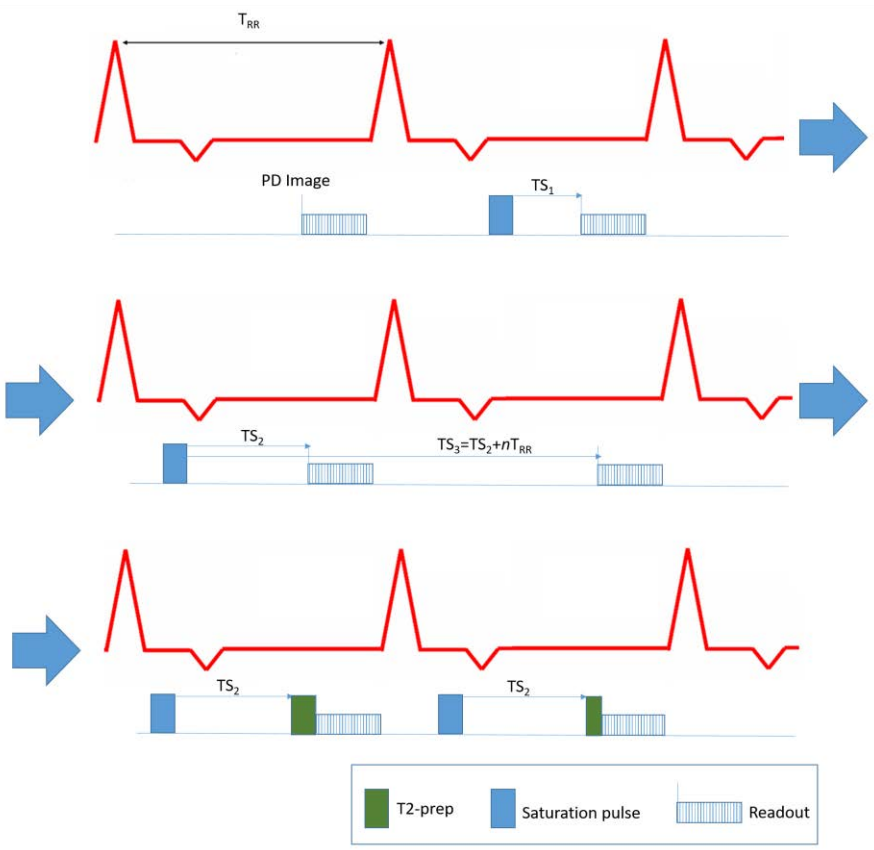

Figure 3-5 - Schematic of the preliminary 3D T1/T2 sequence, flawed by acquiring the T2-weighted images in the same RR interval of the saturation pulse. The sequence performs two turbo field echo (TFE) shots for each 3D image: in the PD image block, the two TFEs are separated by a minimum 6 s magnetization recovery; three images are acquired at TS1, TS2, and TS3 for T1 mapping, while the image of TS2 (T2- prep echo time = 0 ms) and the two images acquired with T2- prep echo times of 23 and 50 ms (bottom row) are used for T2 mapping.

This preliminary 3D T1/T2 sequence is a simple way of modifying the 3D SACORA scheme for acquiring both T1 and T2 maps. However, by design, this acquisition scheme has the drawback of acquiring the T2-weighted images in the same RR interval of the saturation pulse, which for such a rapid acquisition, may not provide T2-weighted images with enough signal for accurate T2 mapping. This limitation is impossible to overcome with this acquisition scheme and signal model, and therefore, this sequence implementation was discarded and not further considered.

In this way, this preliminary 3D T1/T2 sequence was modified to ensure adequate signal for T2 mapping. Hence, the 3D T1/T2 sequence proposed for this feasibility study is designed to acquire T2-weighted images with excellent signal by not acquiring these images in the same RR interval of the saturation pulse, but by acquiring these images with an *n* amount of recovery beats depending on the heart rate. This 3D T1/T2 sequence was named 3D dual saturation-recovery compressed SENSE rapid acquisition (3D dual-SACORA). The acquisition scheme can be divided into three blocks (**Figure 3-6**). In the first block, the proton density (PD) is acquired to avoid effects from previous saturation pulses. The T1 relaxation recovery time between the two readouts of the PD is longer than 6 s to ensure full signal recovery. The second block consists of the acquisition of TS1 and TS2. TS1 is set to 300 ms. TS2 is the maximum saturation time allowed by the heart rate. The third block is focused on the T2 mapping part of the acquisition. Here, TS3 and TS4 are calculated to be always acquired as close as possible to the native cardiac T1 (1500 ms at 3T), and therefore the amount of recovering beats changes according to the heart rate. For a heart rate of 60 bpm, TS3 is 1300 ms, and TS4 is 1603 ms. These two T2-weighted images are acquired with T2-prep echo times of 25 and 45 ms, respectively.

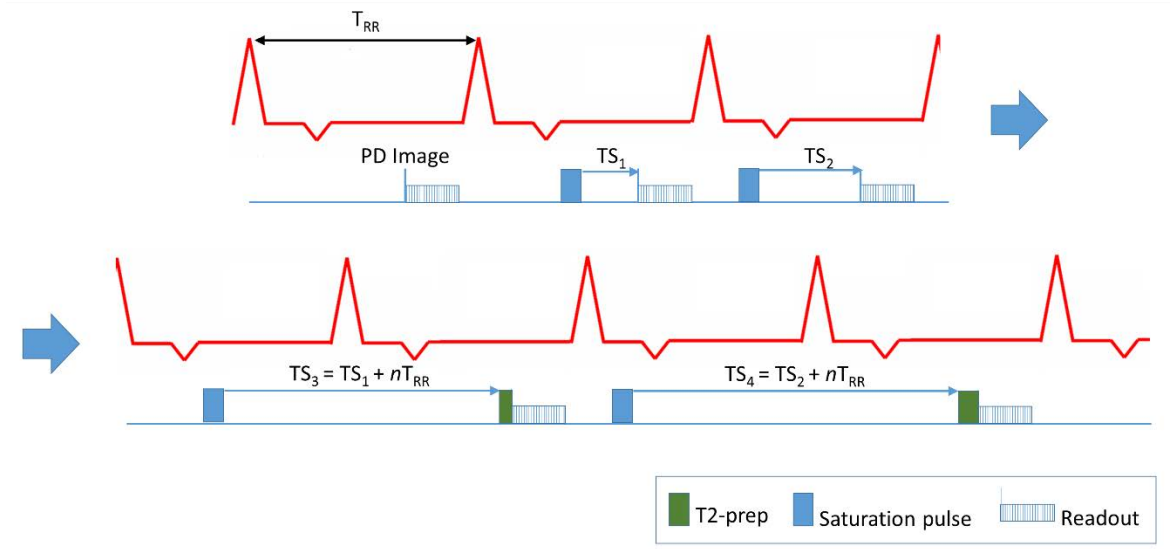

Figure 3-6 - Schematic of 3D dual-SACORA. The sequence performs two turbo field echo (TFE) shots for each 3D image: in the PD image block, the two TFEs are separated by a minimum 6 s magnetization recovery; two T1-weighted images are acquired at TS1 and TS2, and two T2-weighted images are acquired at TS3 and TS4.

The relaxation parameters T1 and T2 are estimated jointly with a three-parameter combined signal model [32] given by

$$M(TS, T2P) = A\left(1 - e^{-\frac{TS}{T1}}\right)e^{-\frac{T2P}{T2}} \quad (3.10)$$

Where TS is the saturation time, T2P is the echo time of the T2 preparation pulses, and A is associated with the signal at full recovery (M0). A three-parameter model was chosen instead of a four-parameter model to improve model stability and therefore increase precision.

Feasibility study

A feasibility study was performed to assess the potential of the 3D dual-SACORA sequence. Built on the sequence parameters of 3D SACORA, the proposed sequence is a spoiled saturation recovery TFE sequence (TR/TE/FA = 2.41ms/1.17ms/5º) with an echo train length of 91. The sequence covered 300x300x72 mm with a slice thickness of 12 mm reconstructed to 6 mm (12 slices) and in-plane resolution of 2.0x2.0 mm. A spatial domain compressed SENSE of 3.5 with a strong denoising level was applied to acquire the 3D volume in 2 independent TFE shots. The acquisition time was 20 RR intervals (for HR=60 bpm), and the acquired images were reconstructed in real-time on the scanner.

All acquisitions were performed on a Philips Ingenia Elition 3.0T X (Philips Healthcare, Best, the Netherlands) using a 28 channel cardiac coil.

A phantom of eight tubes was built to validate 3D dual-SACORA. The phantom consisted of five tubes for T1 values between 338 and 1819 ms and three tubes for T2 values between 19 and 104 ms. The phantom was scanned with the proposed sequence with a simulated heart rate of 60 bpm. Under the same conditions, reference T1 and T2 values were estimated using an inversion-recovery spin-echo (IR-SE) sequence (TR=10000 ms, 12 inversion times ranging 100-3000 ms) and gradient and spin-echo (GraSE) sequence (TR=1000 ms, 9 echo times ranging 9.8-88 ms). 3D dual-SACORA and reference T1 and T2 values were estimated through non-linear least-square fitting following Bloch equations modeling. Mean and standard deviation were measured from the parametric maps with manually drawn regions of interest. 3D dual-SACORA was compared against the reference sequences with linear

regression analysis. The coefficient of variation (CV) and relative error were calculated for assessing precision and accuracy.

An in-vivo study was performed with a healthy volunteer to evaluate the image quality of the parametric maps obtained with the 3D dual-SACORA sequence. T1 and T2 values (mean ± standard deviation) were measured from ROIs manually drawn on the septal myocardium and blood pool. Reference T1 and T2 mean septal values were estimated using MOLLI (TR/TE/FA = 2.28ms/1.03ms/20°, 5(3)3 variant) and GraSE (TR=1091 ms, 9 echo times ranging 9.3-83.5 ms, FA=90°), respectively.

3.2. Improving image quality via a residual dense network (RDN)

3.2.1. RDN architecture and implementation details

After careful consideration, the selected convolutional neural network to improve the image quality of the T1 maps was the Residual Dense Network (RDN) [56]. As described in section 1.4.2, this network can make full use of all the image hierarchical features (local features and global features) and has shown outstanding performance against state-of-the-art methods on benchmark datasets.

In this study, an RDN architecture (**Figure 1-36**) [56] following the image super-resolution (ISR) implementation presented in [68] was used; hence the hyperparameters common to all experiments are the following:

- number of residual dense blocks (RDB) = 6,
- number of convolutional layers stacked inside an RDB = 20,
- number of feature maps of each convolutional layer = 64,
- kernel size of convolutional layers (local and global feature fusion = 1 × 1, all the rest = 3 × 3),
- learning rate decay (initial value = 0.0004, decay factor = 0.5, decay frequency = 30)
- flatness of minima (minimum = 0, maximum = 0.15, increase = 0.01, increase frequency = 5)
- patch size of low resolution training data = 40,

- training steps per epoch = 500,
- training batch size = 16

Zero-padding is used for convolutional layers of kernel size of 3 × 3 to keep the shape fixed. In the RDB, the rectified linear unit (ReLU) activation function is applied, which is linear if the input is positive and zero if the input is negative, making the network easier to train. Batch normalization (BN) and pooling layers are not used to increase computational performance and maximize the reliability of the pixel information, respectively.

The model was trained with a GeForce GTX TITAN X using Python 3.6.4, Tensorflow 1.13.1, Keras 2.2.4, and ISR 2.1 [68].

3.2.2. Model training and validation

Although the model has shown excellent performance on image super-resolution and denoising against state-of-the-art methods on benchmark real-world image datasets [55, 56, 69], it has not been validated on medical datasets. In this way, the model was initially validated on two benchmark medical datasets, one containing brain MR images and the other containing cardiac MR images, achieving a reasonable assessment of the model's robustness. After this validation, a self-acquired cardiac dataset was prepared, and the model was validated on improving cardiac T1 maps. The training and validation procedures are described in detail in this section.

Benchmark medical datasets

The high-resolution brain MR images used in this work were obtained from the MGH-USC Human Connectome Project (HCP) database (https://ida.loni.usc.edu/login.jsp). The images include different 2D slices obtained from several high-resolution 3D acquisitions. Low-resolution images were obtained by downsampling (x2) the high-resolution images with the Lanczos algorithm [54], as exemplified in **Figure 3-7**. The low and high-resolution datasets were divided into 1000 images for training, 400 images for validation, and 100 images for testing. The network was trained during 100 epochs with two different loss functions, the

Mean Absolute Error loss function (L1 loss) and the Peak Signal-to-Noise Ratio loss function (PSNR loss). L1 loss is defined as the mean of the absolute differences between the predicted and real values. It is frequently used in super-resolution and image reconstruction because it is robust against outliers, discourages blurring, and provides good convergence [56, 70, 71]. PSNR is defined as the ratio between the maximum power of the signal and the power of the noise of the signal. It is a metric frequently used to measure the quality of images that have been compressed, making it attractive to use a loss function to directly maximize this metric for image enhancement models. Hence, the PSNR loss is theoretically promising and has shown excellent results in image enhancement [72]. The training with L1 loss lasted approximately 15 hours and 54 minutes, with the best result achieved at epoch 70, while the training with PSNR loss took roughly 14 hours and 44 minutes, with the best result achieved at epoch 26.

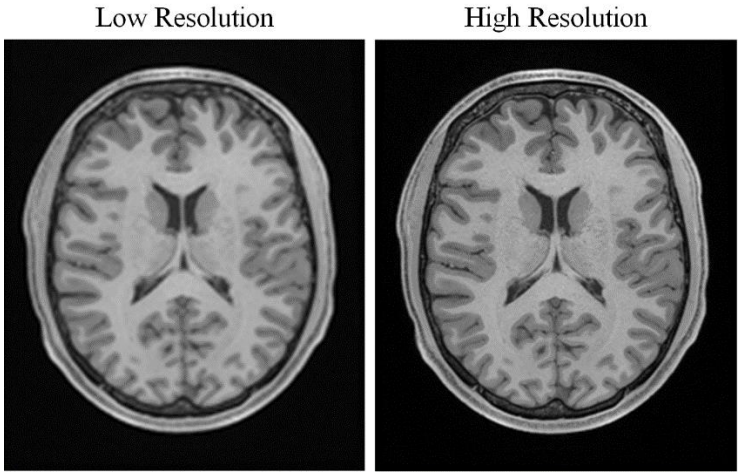

Figure 3-7 – Representative images of the low-resolution (left) and high-resolution (right) 2D brain images used for training the model.

Testing the network with brain images provides information about the implementation's performance in a best-case scenario, with good SNR and several well-defined edges. In contrast, cardiac images tend to be noisier and more challenging than brain images. Therefore, the same network was trained and applied in a cardiac dataset obtained from the HVSMR 2016 challenge (http://segchd.csail.mit.edu/) [73], providing a robust dataset of high-resolution cardiac images with different slice's orientation and resolution. Low-

resolution images were obtained by downsampling (x2) the high-resolution images with the Lanczos algorithm, as shown in **Figure 3-8**. The dataset's size was the following for both resolutions: 1000 images for training, 422 images for validation, and 100 images for testing. The network was trained during 84 epochs with L1 loss, lasting roughly 12 hours and 30 minutes, and achieving the best result at epoch 71.

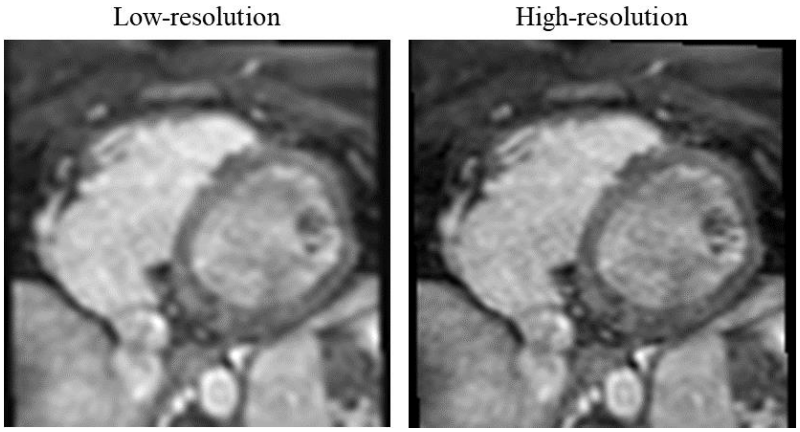

Figure 3-8 - Representative images of the low-resolution and high-resolution 2D cardiac images used for training the model.

Self-acquired cardiac dataset

All images were acquired on a Philips Achieva 3T-Tx (Philips Healthcare, Best, the Netherlands) using a 32 channel cardiac coil. Several different 3D high-resolution acquisitions were performed on pigs to obtain a robust dataset of 2D slices with different orientations and resolutions, including images of healthy pigs and pigs with heart disease. The study protocol was approved by the local institutional Animal Research Committee and conducted in accordance with recommendations of the Guide for the Care and Use of Laboratory Animals.

At this point, two experiments were performed. The first experiment tests the model's performance on images acquired for the self-acquired training dataset, while the second experiment tests the model's effectiveness on improving the T1-weighted images and the corresponding T1 maps. In the first experiment, the datasets consisted of 808 images for training, 200 images for validation, and 100 images for testing. The low-resolution images

were obtained by downsampling (factor of 3) the high-resolution images using the Lanczos resampling (**Figure 3-9**). Data augmentation was used by applying rotations. The model was trained with L1 loss during 80 epochs (approximately 11 hours and 24 minutes), achieving the best result at epoch 77.

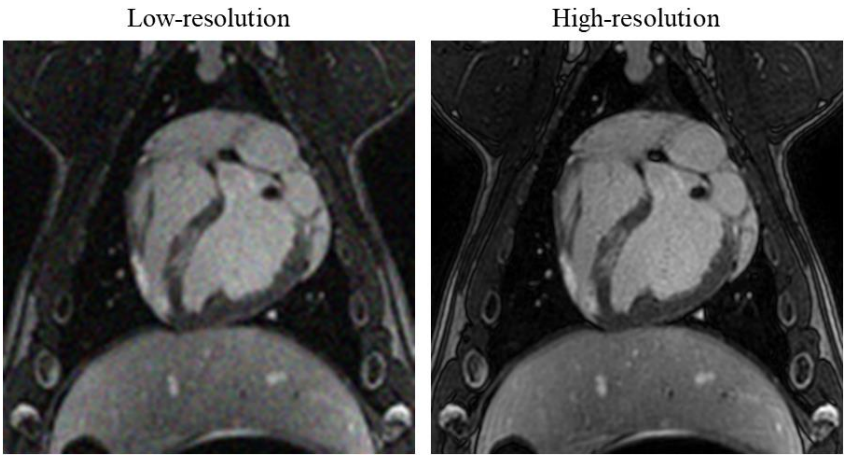

Figure 3-9 - Representative images of the image dataset used for training the model. On the right, an acquired high-resolution image. On the left, the corresponding low-resolution image, obtained with Lanczos downsampling.

In the second experiment, the focus was to improve the T1 maps - both resolution and SNR. The datasets were upsized to increase performance, and Rician noise was added to the low-resolution images to simulate noisy MR images and achieve a denoising effect. In this way, more data was acquired, and data augmentation was used by applying rotations and adding Rician noise. As in the previous experiments, low-resolution images were obtained by downsampling (factor of 3) the high-resolution images using the Lanczos resampling (**Figure 3-10**). Both low and high-resolution datasets were divided into 1060 images for training and 254 images for validation. The RDN was trained with L1 loss during 80 epochs (approximately 14 hours and 45 minutes), achieving the best result at epoch 72.

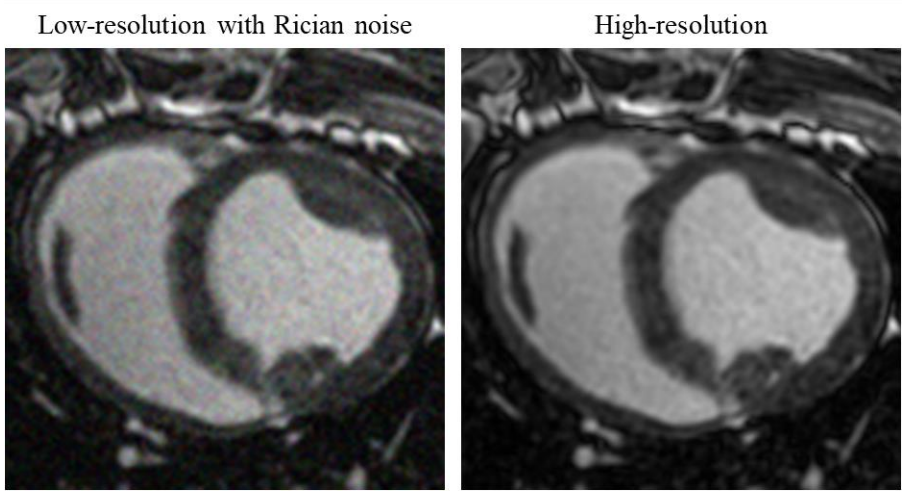

Figure 3-10 - Pair of images used for training the model. On the right, an acquired high-resolution image. On the left, the corresponding low-resolution image, obtained with Lanczos downsampling and by adding Rician noise.

3.2.3. Testing

Image quality assessment

The datasets prepared to evaluate the model's performance on improving MR images' quality have a subset for testing. This subset's images, which in our experiments are 100 pairs of low-resolution and high-resolution images, are used to compare the model results against a state-of-the-art method. In this way, the testing subset's low-resolution images were upsampled with the trained model and Lanczos resampling [54]. Afterward, these upsampled images were compared with the original high-resolution images using subjective and objective metrics of image quality assessment to evaluate the model's performance quantitatively.

The root mean squared error (RMSE) is a general-purpose metric that estimates the perceived errors of images (RMSE of 0 indicates perfect similarity), providing information about a model's accuracy by comparing directly the pixel values of the ground-truth image with the output image of the model. The RMSE is given by

$$RMSE = \sqrt{\frac{1}{n}\sum_{i=1}^{n}(O_i - P_i)^2} \tag{3.11}$$

Where n is the number of pixels of the image, O_i are the pixel values from the original high-resolution image, and P_i are the pixel values predicted by the model.

The Peak Signal-to-Noise Ratio (PSNR) metric is an objective computational method closely related to the RMSE. It is currently the most used metric to evaluate super-resolution models because it is accurate, widely present in literature, and easy to compute [55]. The higher the values of PSNR, the better the similarity between the compared images. The PSNR is given by

$$PSNR = 10\log_{10}\left(\frac{L^2}{\frac{1}{n}\sum_{i=1}^{n}(O_i - P_i)^2}\right) \tag{3.12}$$

Where n is the number of pixels of the image, L is the maximum pixel value, O_i are the pixel values from the original high-resolution image, and P_i are the pixel values predicted by the model.

These two standard metrics assess the image quality through objective computational methods and do not consider the humans' perceptual evaluation. Another standard metric is the structural similarity (SSIM) metric. It is a subjective metric that evaluates the images from the humans' perspective and takes into account luminance, contrast, and structure [74]. This metric provides an accurate perceptual assessment with the drawback of being quite costly. The SSIM values are between 0 and 1, where 1 indicates perfect structural similarity between images. The SSIM index can be given by

$$SSIM(x,y) = \frac{(2\mu_x\mu_y + C_1)(2\sigma_{xy} + C_2)}{(\mu_x^2 + \mu_y^2 + C_1)(\sigma_x^2 + \sigma_y^2 + C_2)} \tag{3.13}$$

Where x and y are the two images to be compared (high-resolution image and estimated image), μ_x and μ_y are the respective means of the images, σ_x and σ_y are the respective standard deviations of the images, σ_{xy} is the covariance between the images, and C1 and C2 are constants included to avoid instability.

These three metrics were calculated for the testing subsets (100 images) using images upsampled with the trained model and Lanczos resampling. For both methods, the values obtained from the full subset were averaged to obtain a single value for each metric, obtaining

a complete image quality assessment of the images produced by both the trained model and Lanczos resampling.

T1 maps assessment

After showing the performance of the trained models in increasing the quality of MR images, in this part, the goal was to evaluate the quality of the T1 maps estimated through T1-weighted images upsampled by the trained model. In this case, no ground-truth image is available because the only images available are the T1-weighted images acquired with the T1 mapping sequences; therefore, the acquired images were upsampled x3 using both the trained model and the state-of-the-art Lanczos resampling in order to compare the T1 maps obtained by the model with a reference method.

Two T1 mapping sequences early described in this thesis, 3D SACORA and 3D SASHA, were used to test the RDN model. For both sequences, the images of four healthy pigs from the 3D SACORA study (described in section 3.1.3) were used [51], which were acquired on a Philips Achieva 3T-Tx using a 32 channel cardiac coil. The 3D SACORA acquisition parameters were: TR/TE/FA = 2.8 ms/1.32 ms/5°; echo train length = 76; compressed SENSE factor = 4.5; in-plane resolution = 2×2 mm; 12 reconstructed slices (acquisition slice thickness of 10 mm reconstructed to 5 mm). The 3D SASHA acquisition parameters were: TR/TE/FA = 2.8 ms/1.3 ms/12°; echo train length = 30; compressed SENSE factor = 1.8; in-plane resolution = 2×2 mm; 12 reconstructed slices (acquisition slice thickness of 10 mm reconstructed to 5 mm). In **Figure 3-11**, representative saturation time images acquired with 3D SACORA and the corresponding T1 map are shown.

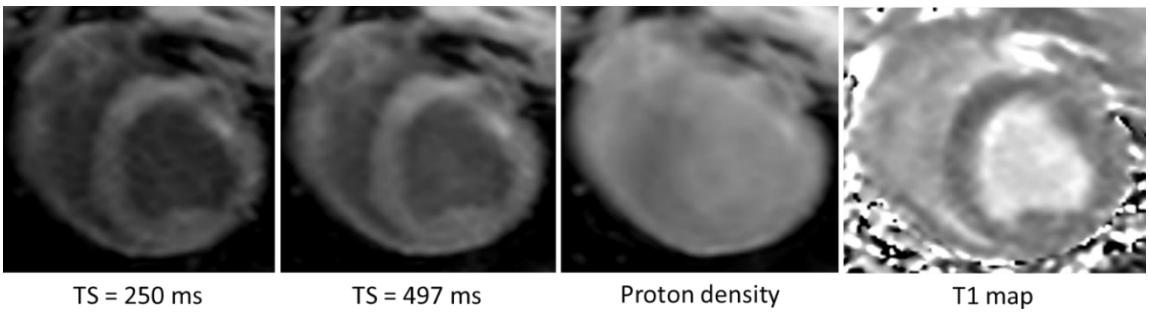

Figure 3-11 – Example of the in-vivo images acquired with 3D SACORA and the corresponding T1 map.

The acquired T1-weighted images were upsampled x3 with the trained model and the Lanczos resampling, and the resulting upsampled images were fitted to obtain the T1 maps following the respective Bloch equations modeling of 3D SACORA and 3D SASHA. The computed T1 maps were visually assessed to evaluate the performance of both methods. ROIs were drawn in the septal myocardium and blood pool of 20 slices (5 per pig) to analyze the effect of the upsampling on the T1 values. The mean T1 and the standard deviation were obtained from the ROIs. Furthermore, line ROIs were drawn crossing the myocardium (**Figure 3-12**) to elaborate a profile of the pixel values on the edges between myocardium and blood and evaluate the resolution.

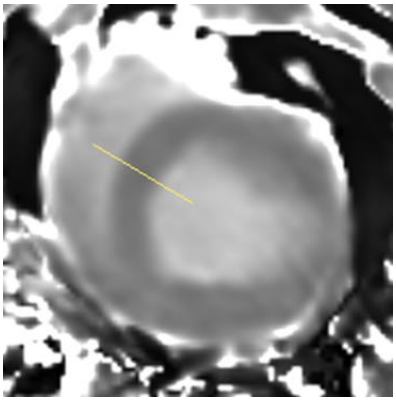

Figure 3-12 – Example of a line ROI crossing the myocardium of a 3D SASHA T1 map (no improvement of the image quality was applied) to obtain the pixel values profile.

CHAPTER 4

RESULTS

4.1. Single breath-hold saturation recovery 3D cardiac T1 mapping via compressed SENSE

4.1.1. Phantom validation

The Passing-Bablok regression plots show good correlation and no significant bias between methods. The 3D SACORA plot (**Figure 4-1a**) has a slope of 0.99 (95% confidence interval [CI]: 0.98, 1.01) and an intercept of 12.90 ms (95%CI: -6.19, 23.02 ms), whereas the 3D SASHA plot (**Figure 4-1b**) has a slope of 1.005 (95%CI: 0.997, 1.013) and an intercept of -4.62 ms (95%Cl: -11.60, 2.47 ms).

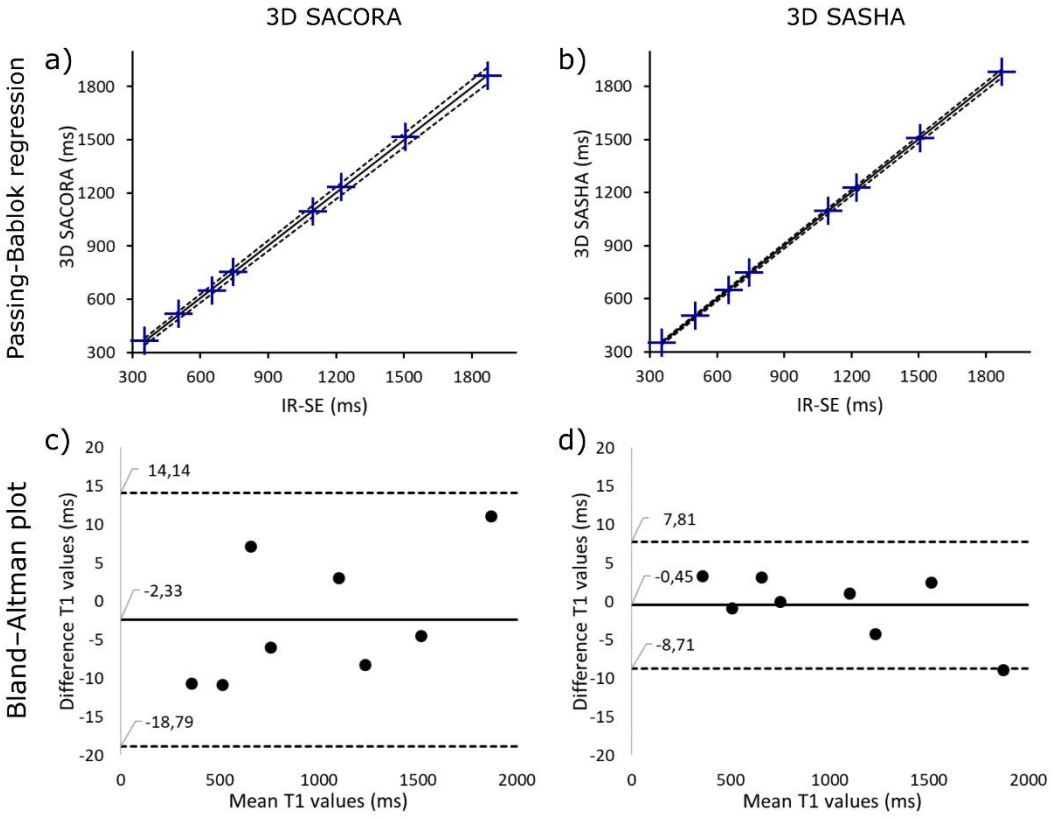

Figure 4-1 - 3D SACORA and 3D SASHA results from phantom experiments validated against IR-SE. a,b) Passing-Bablok regressions of 3D SACORA and 3D SASHA. c,d) Bland-Altman plots of 3D SACORA and 3D SASHA.

The Bland-Altman plots in **Figure 4-1** compare reference T1s with T1s estimated by 3D SACORA and 3D SASHA. These plots show good agreement between both methods and IR-SE. For 3D SACORA (**Figure 4-1c**), the bias was -2.3 ms (95%CI: -18.79, 14.14 ms). For 3D SASHA (**Figure 4-1d**), the bias was -0.45 ms (95%CI: -8.71, 7.81 ms).

The relative error at different heart rates ranged from -0.016 to 0.032 for 3D SACORA (mean, 0.008; standard deviation, 0.011); for 3D SASHA the range was -0.0095 to 0.039 (mean, 0.008; standard deviation, 0.01) (**Figure 4-2a, b**). 3D SACORA showed less dependence on heart rate, particularly for pre-contrast cardiac T1 values at 3T; estimated T1 values with 3D SASHA tended to increase with higher heart rate, whereas 3D SACORA T1s seemed to be relatively independent of heart rate. Regarding accuracy, both sequences performed equally well.

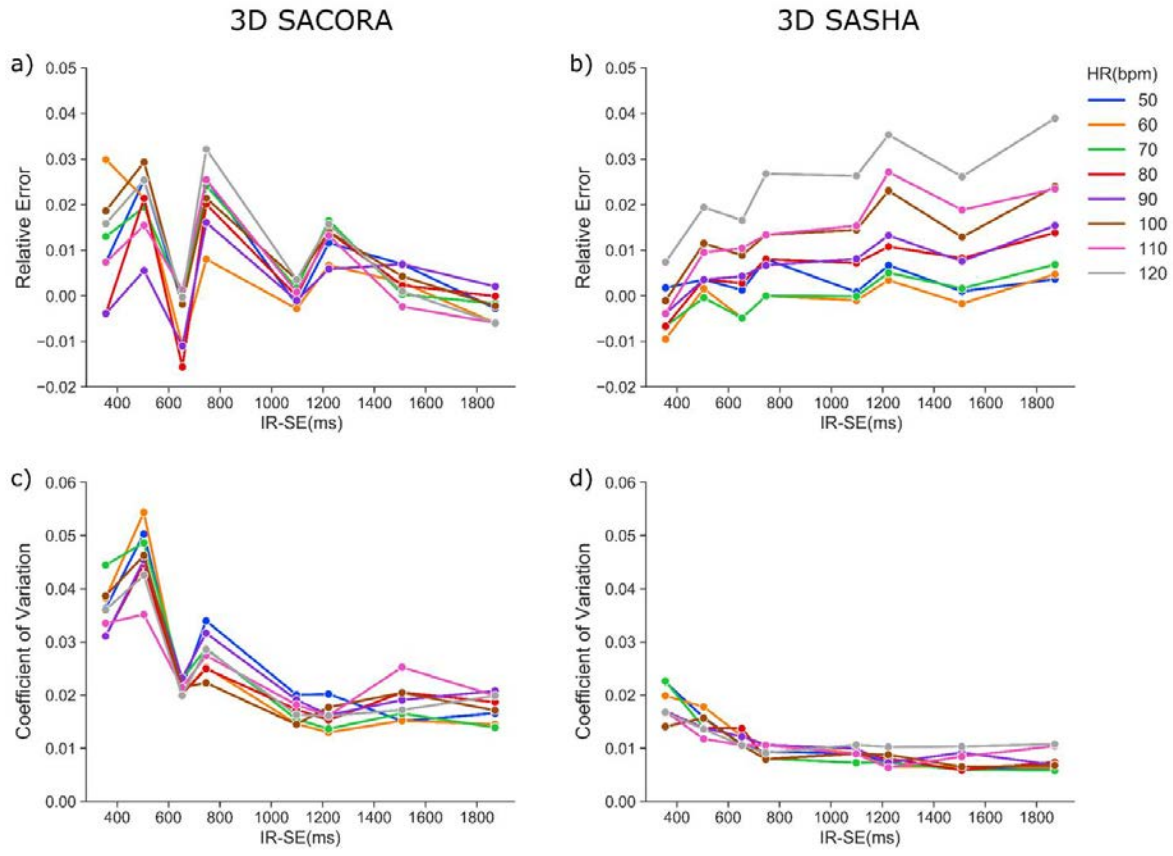

Figure 4-2 - Phantom experiments assessing the HR dependency of 3D SACORA and 3D SASHA. a,b) Relative error of 3D SACORA and 3D SASHA at different HRs. c,d) Coefficient of variation of 3D SACORA and 3D SASHA at different HRs.

The coefficient of variation at different heart rates ranged from 0.013 to 0.054 for 3D SACORA (mean, 0.025; standard deviation, 0.011); for 3D SASHA, the range was 0.006 to 0.023 (mean, 0.011; standard deviation, 0.004) (**Figure 4-2c, d**). Although precision was acceptable with both sequences, 3D SASHA performed slightly better, particularly on short T1s. The coefficient of variation appeared to be independent of the heart rate in both sequences.

4.1.2. In-vivo validation

Scans of the seven pigs were performed with 3D SACORA and 3D SASHA before and after MR contrast agent administration. 3D SACORA acquired the 3D T1 map in 15 heartbeats (heart rate, 60 bpm). For both sequences, the final T1 parametric maps were obtained from the scanner shortly after acquisition. Reconstruction, fitting, and image generation took approximately 20s.

Four images from the same animal for each sequence are shown in **Figure 4-3**: two T1-weighted images, a PD image, and the corresponding T1 map. All T1-weighted images showed good contrast and quality. The TS1 image from 3D SACORA presented some noise, likely due to the short saturation time and relatively high compressed SENSE factor (4.5). No contrast was visible between myocardium and blood pool in the PD images, as expected. The T1 maps correctly represented the information contained in the T1-weighted images.

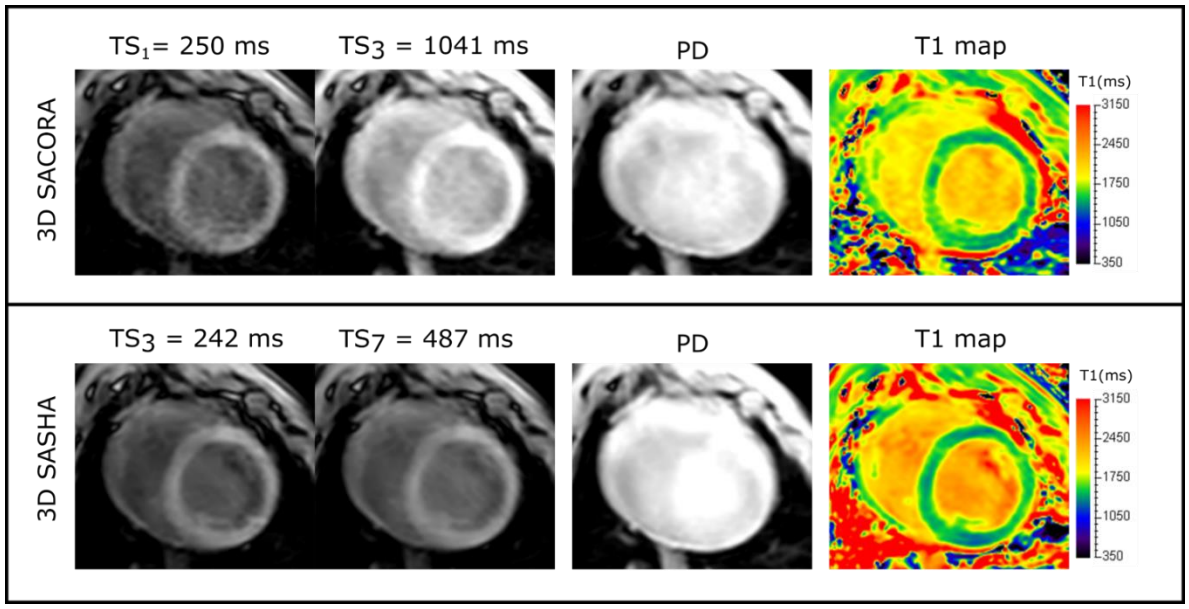

Figure 4-3 - Representative images acquired from pig 6 with 3D SACORA and 3D SASHA (two T1-weighted images and a PD image) and the corresponding T1 maps.

Bulls-eye plots were calculated for 3D SACORA and 3D SASHA, according to the AHA LV model (**Figure 4-4**). Bulls-eye plots of mean T1 values (**Figure 4-4a, b**) showed good homogeneity across the LV myocardium for both sequences. The mean T1 for the whole LV myocardium was 1480 ± 33 ms with 3D SACORA and 1539 ± 54 ms with 3D SASHA. For the blood pool, the mean T1 values were 2126 ± 104 ms and 2306 ± 93 ms, respectively. The difference between the two sequences in mean whole LV myocardium T1 was mainly due to T1 measurements in the lateral and anterior segments. The bulls-eye plots for the coefficient of variation (**Figure 4-4c, d**) showed good precision in the measurement of T1 values in myocardium and blood for both sequences. The mean coefficients of variation in 3D SACORA were 0.029 ± 0.005 in the whole LV myocardium and 0.033 ± 0.006 in the blood pool; the corresponding values for 3D SASHA were 0.030 ± 0.008 and 0.029 ± 0.005.

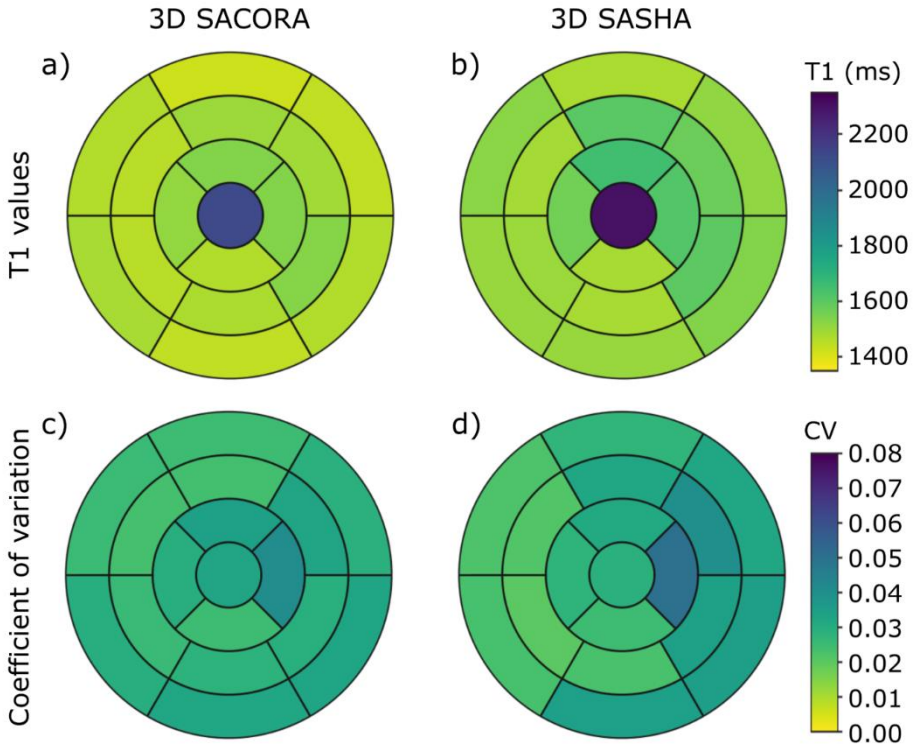

Figure 4-4 - Bulls-eye plots of T1 and coefficient of variation (CV) for the whole left-ventricle myocardium with 3D SACORA and 3D SASHA. The central segment corresponds to the blood. a,b) Bulls-eye plots of mean T1 values for both sequences. c,d) Bulls-eye plots of mean CV for both sequences.

Septal T1s and coefficients of variation were measured with 3D SACORA and 3D SASHA in all seven pigs before and after administration of MR contrast agent (**Figure 4-5**). Native and post-contrast T1 (**Figure 4-5a, b**) did not differ between the two sequences, confirming good accuracy and precision. Mean septal native and post-contrast T1s measured with 3D SACORA were 1453 ± 44 ms and 824 ± 66 ms, respectively. For 3D SASHA, the mean septal native T1 was 1460 ± 60 ms and the mean septal post-contrast T1 was 824 ± 60 ms. The coefficient of variation plots (**Figure 4-5c, d**) showed good precision for both sequences in all animals. The mean coefficient of variation for native septal T1 was 0.041 ± 0.010 for 3D SACORA and 0.039 ± 0.010 for 3D SASHA. The post-contrast values were 0.050 ± 0.008 and 0.041 ± 0.008, respectively.

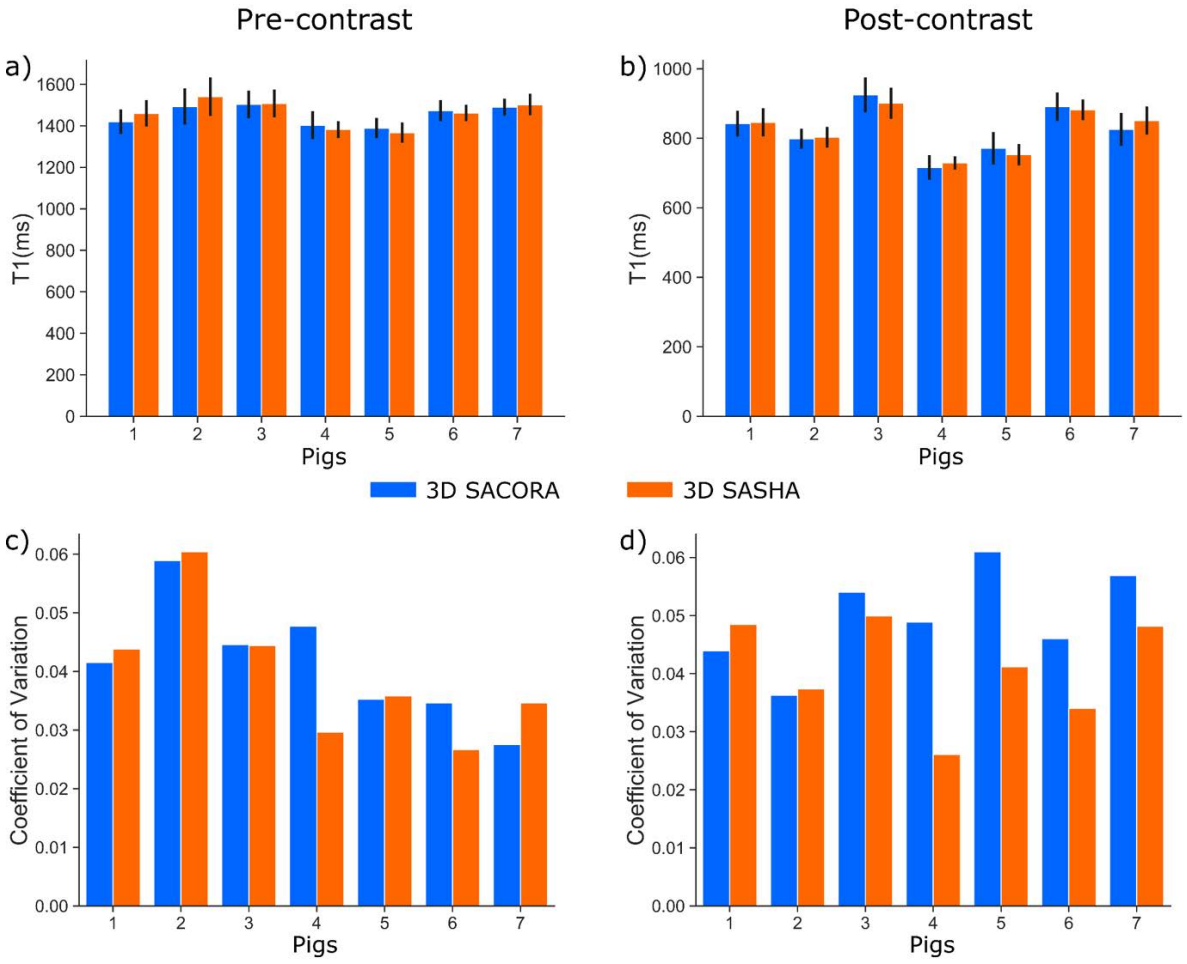

Figure 4-5 - Septal T1 measurements (pre-contrast and post-contrast) obtained from all pigs with 3D SACORA and 3D SASHA. a) Pre-contrast septal T1 and standard deviation for both sequences. b) Post-contrast septal T1 and standard deviation for both sequences. c) Septal coefficient of variation of pre-contrast acquisitions for both sequences. d) Septal coefficient of variation of post-contrast acquisitions for both sequences.

Representative pre-contrast and post-contrast T1 maps of three slices (apex, middle, base) acquired with 3D SACORA and 3D SASHA in two pigs are shown in **Figure 4-6**. 3D SACORA images showed good contrast and homogeneity, and were comparable to corresponding 3D SASHA images, despite the shorter acquisition time (15s vs. 188s, for a heart rate of 60 bpm).

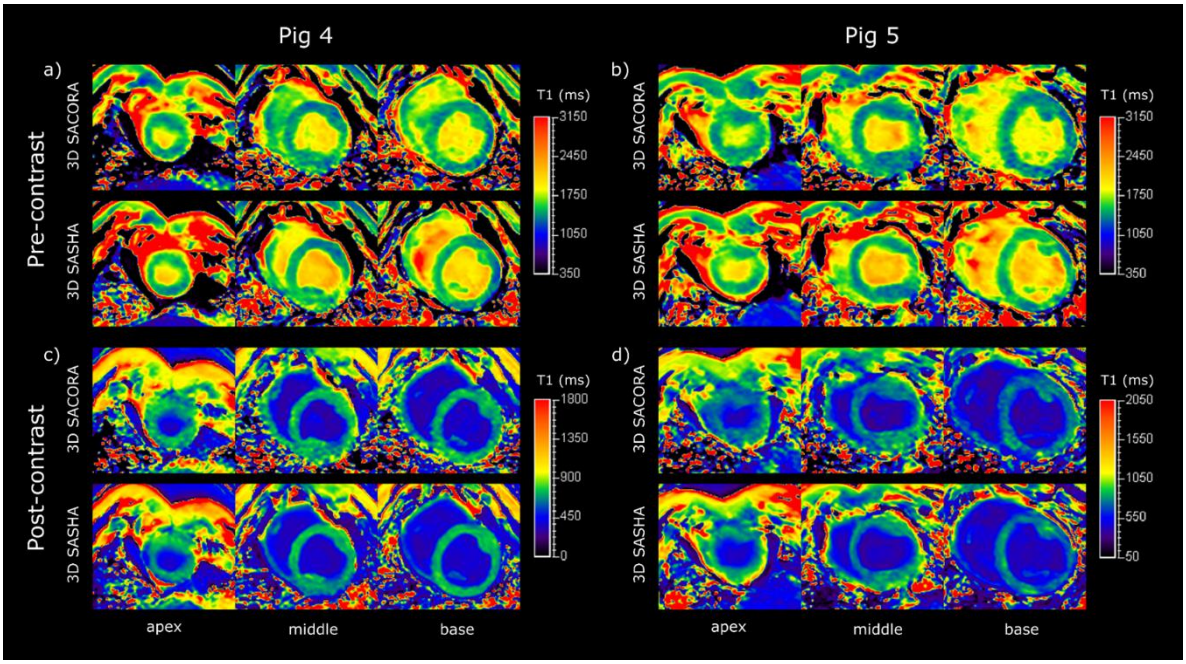

Figure 4-6 - Pre-contrast and post-contrast T1 maps of three slices (apex, middle, base) acquired with 3D SACORA and 3D SASHA from pigs 4 and 5. a,b) Pre-contrast images from pigs 4 and 5. c,d) Post-contrast images from pigs 4 and 5.

4.1.3. Joint T1 and T2 mapping

T1 and T2 maps of the phantom were successfully obtained with the proposed 3D dual-SACORA sequence. The linear regression plots (**Figure 4-7**) showed good agreement between the T1 and T2 values obtained by the proposed sequence, and IR-SE and GraSE, respectively. However, 3D dual-SACORA seemed to underestimate very long T2s.

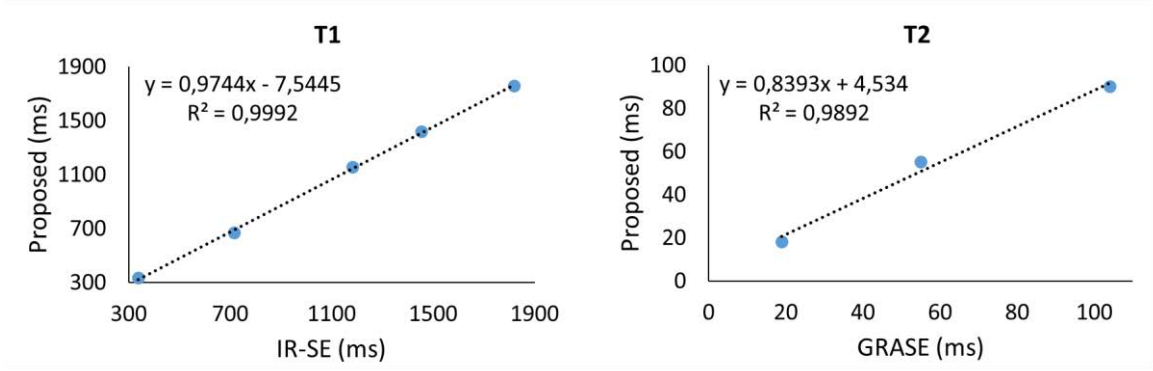

Figure 4-7 – Linear regression plots from the phantom experiments comparing 3D dual-SACORA against IR-SE and T2-GraSE.

The coefficient of variation and relative error are shown in **Figure 4-8** for both T1 and T2. The plots show that the 3D dual-SACORA sequence achieved good precision and accuracy for most values. As already seen in the linear regression analysis, the relative error also suggests that the 3D dual-SACORA sequence underestimated very long T2s (104 ms).

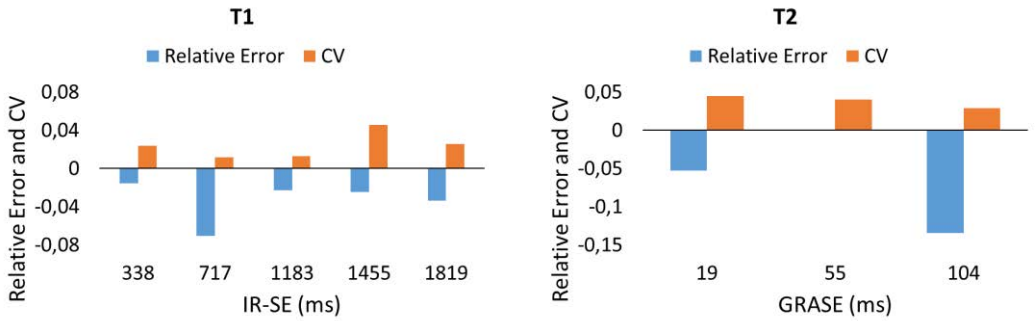

Figure 4-8 - Coefficient of Variation (CV) and relative error of 3D dual-SACORA for both relaxation parameters.

A volunteer was successfully scanned with 3D dual-SACORA (acquisition duration of approximately 20s) in a single breath-hold. T1-weighted images (TS1 and TS2) and T2-weighted images (TS3 and TS4) showed good contrast and quality, as shown in **Figure 4-9**. As expected, no contrast was visible between myocardium and blood pool in the PD images. Although TS4 has a T2 preparation of 45 ms, the image's SNR and quality were excellent as it was acquired with a recovery beat (TS4 = 1773 ms). The parametric maps accurately represented the information contained in the saturation time images.

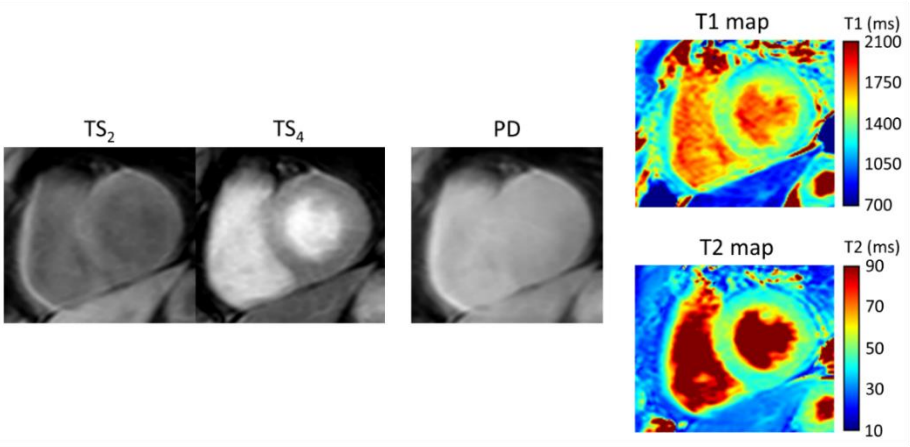

Figure 4-9 - Representative images acquired from the volunteer with the 3D dual-SACORA sequence and the corresponding parametric maps.

Representative parametric maps acquired with the 3D dual-SACORA sequence in the volunteer are shown in **Figure 4-10**. The maps showed good contrast and homogeneity. The mean septal T1 of the three slices was 1443.7 ± 51.3 ms, while the mean blood pool was 1799.7 ± 64.7. Regarding T2, the mean septal value of the three slices was 51.7 ± 2.8 ms, and the mean blood pool was 170.3 ± 24.7 ms. As reference values, the septal T1 estimated with MOLLI was 1208 ms, while the septal T2 estimated with GraSE was 50 ms.

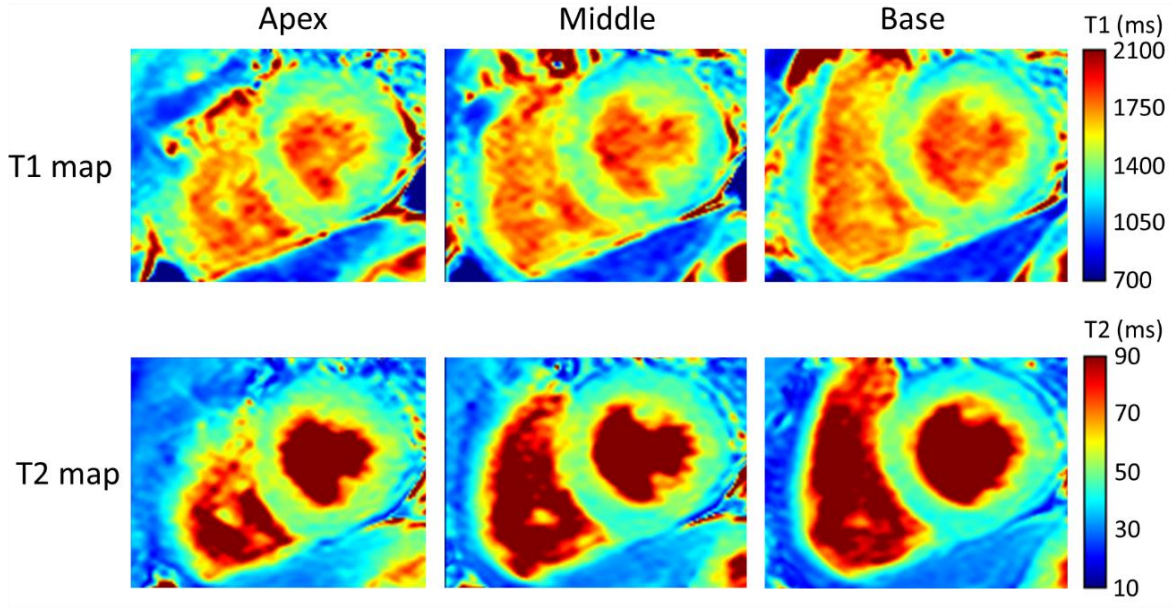

Figure 4-10 - Representative parametric maps of three slices (apex, middle, base) acquired with the 3D dual-SACORA sequence.

4.2. Improving image quality via a residual dense network (RDN)

4.2.1. Image quality assessment

The RDN model was trained with several different medical datasets to thoroughly evaluate the model's performance with MR images. Firstly, the model was tested with brain images as they have excellent SNR and several well-defined edges. The model was tested with two losses: L1 loss and PSNR loss. The model's training was successful with both losses;

however, the PSNR loss exhibited more erratic variation over the epochs and more difficulty stabilizing than the L1 loss. The L1 loss superiority can also be seen in the comparison between the model and Lanczos resampling results of the testing subset, as shown in **Table 4-1**. The L1 loss achieved better results on the analyzed metrics than the PSNR loss and the Lanczos resampling.

Methods / Metrics	RDN L1 loss	RDN PSNR loss	Lanczos resampling
RMSE (ms)	5,4	5,8	9,1
PSNR (dB)	32	31	26
SSIM	0,80	0,81	0,63

Table 4-1 – Table with the averaged metrics calculated from the testing subset (brain benchmark dataset) for the three methods.

Based on these results, the L1 loss was selected as the default loss for the remaining experiments. The images upsampled with the model are far more similar to the original high-resolution images than the images upsampled with Lanczos resampling, as shown in **Figure 4-11**. The images upsampled with the model show high image quality, excellent resolution, and well-defined edges. Interestingly, the model was able to discriminate and eliminate an artifact present on the low-resolution image, creating an upsampled image free of artifacts.

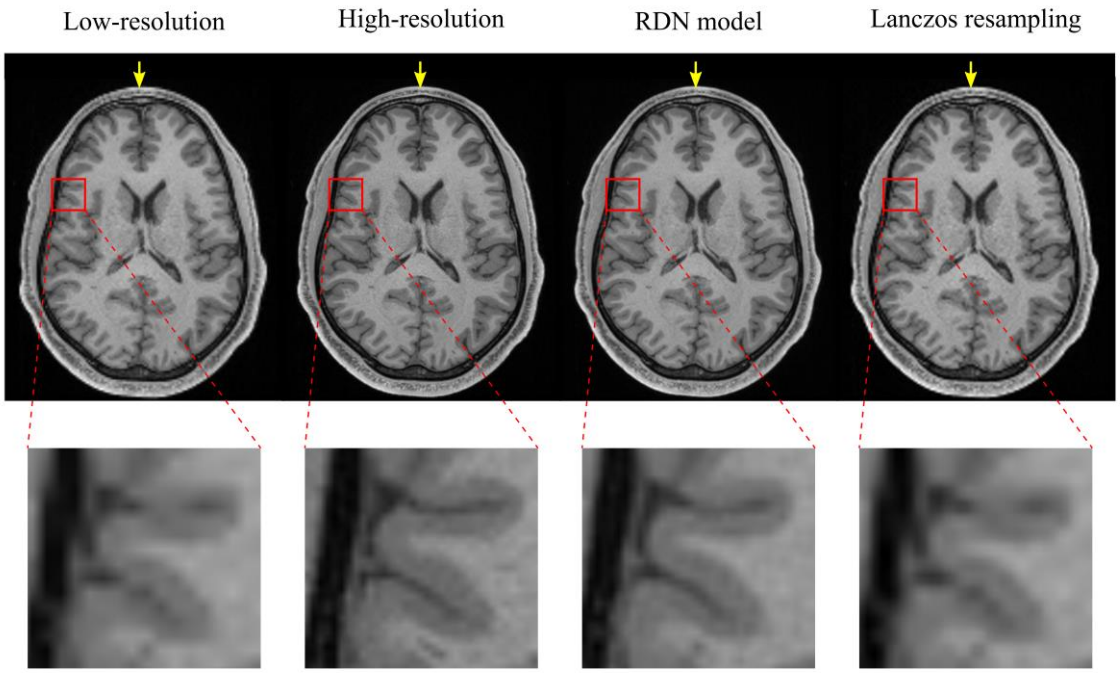

Figure 4-11 – Visual comparison between the original images (brain benchmark dataset) from the testing subset and the images obtained by upsampling the low-resolution image with the model and Lanczos resampling. The yellow arrow points to an artifact of the low-resolution image that was eliminated by the model.

The model was also tested with a benchmark cardiac dataset to test its performance with cardiac images, which are noisier and have fewer well-defined edges than brain images. The model was trained successfully, similarly to the behavior exhibited with the brain dataset. The model again achieved better metrics than the Lanczos resampling on the testing subset, as shown in **Table 4-2**. Nevertheless, the difference between the methods was more evident with the brain dataset, as expected, considering the fewer well-defined edges of the cardiac images.

Methods / Metrics	RDN L1 loss	Lanczos resampling
RMSE (ms)	3,33	4,49
PSNR (dB)	29,80	27,30
SSIM	0,79	0,76

Table 4-2 - Table with the averaged metrics calculated from the testing subset (cardiac benchmark dataset) for the two methods.

Both methods were able to improve the low-resolution images visually, as shown in **Figure 4-12**. The image upsampled with the model seems slightly better than the image upsampled with Lanczos resampling, although the difference is trivial. This minimal difference is most likely related to the relatively low-resolution of the cardiac dataset's high-resolution images.

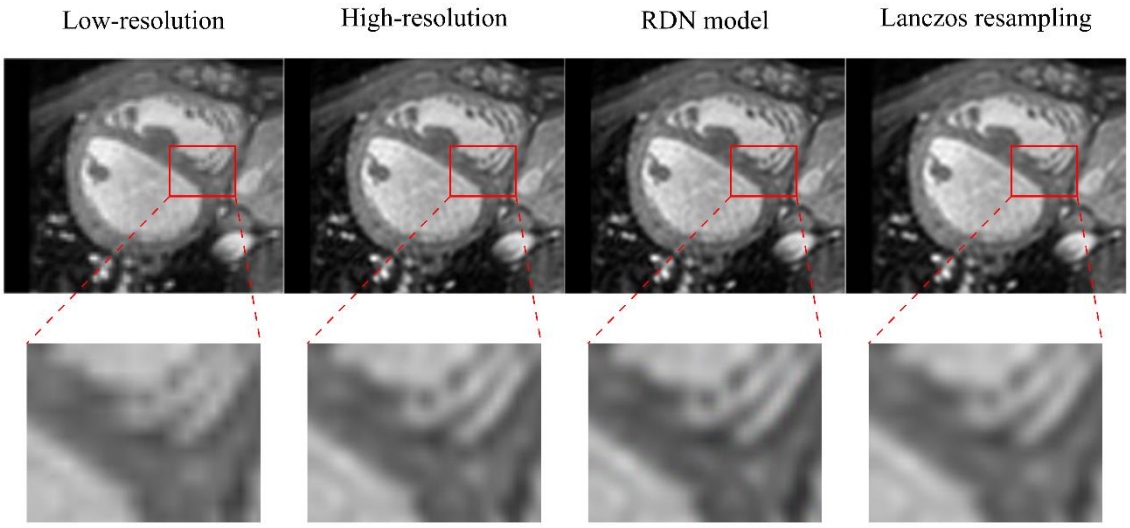

Figure 4-12 - Visual comparison between the original images from the testing subset (cardiac benchmark dataset) and the images obtained by upsampling the low-resolution image with the model and Lanczos resampling.

The importance of high-quality, high-resolution images for training the model was demonstrated. Hence, high-resolution cardiac images were acquired purposely for improving the performance of the model. The model was trained successfully and was clearly able to achieve better metrics on the testing subset than the Lanczos resampling, as shown in **Table 4-3**.

Methods / Metrics	RDN L1 loss	Lanczos resampling
RMSE (ms)	5,5	7,6
PSNR (dB)	31	26
SSIM	0,90	0,81

Table 4-3 - Table with the averaged metrics calculated from the testing subset (self-acquired cardiac dataset) for the two methods.

A visual assessment of the upsampled images shows that the model produced images considerably better than the low-resolution images and identical to the original high-resolution images, as shown in **Figure 4-13**. Comparing the model against Lanczos resampling, it produced better quality images than Lanczos resampling, particularly on parts of the images with well-defined edges.

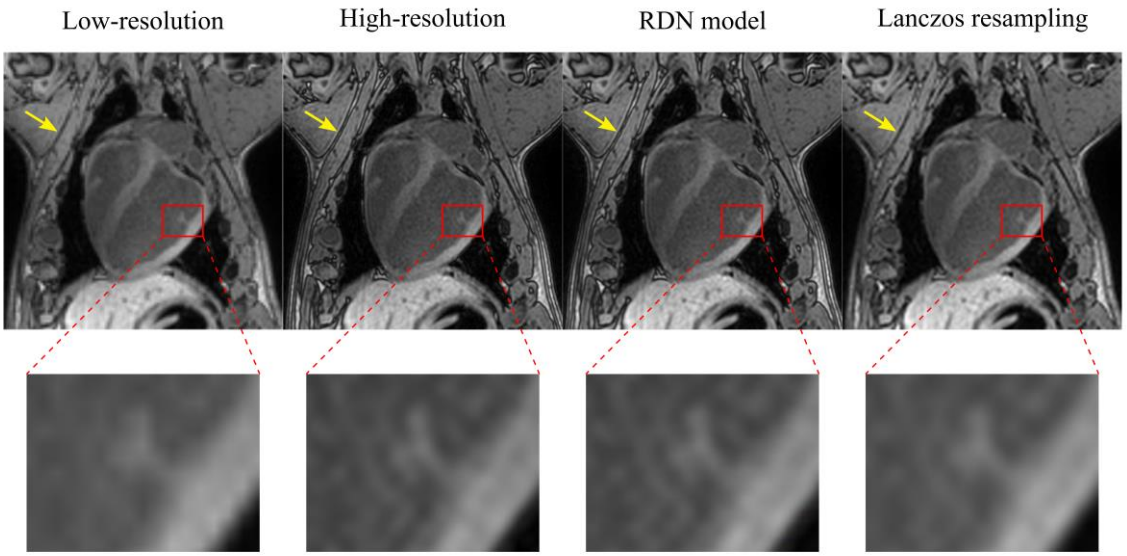

Figure 4-13 – Visual comparison between the original images (self-acquired cardiac dataset) from the testing subset and the images obtained by upsampling a low-resolution image with the model and Lanczos resampling. The yellow arrow points to an area with defined edges, which have a much better resolution with the model than with Lanczos resampling.

4.2.2. T1 maps assessment

In the previous section, the feasibility of using the RDN model to improve MR images was demonstrated. In this section, the results achieved while studying the feasibility of applying the model to T1 maps are presented. The model was successfully trained to upsample and denoise the T1-weighted images that are pixel-wise fitted to produce the maps. The trained model was tested in a rapid acquisition (3D SACORA) and a longer sequence that prioritizes the SNR (3D SASHA).

3D SACORA

The T1-weighted images of 3D SACORA were upsampled and denoised using the RDN model and Lanczos resampling. First of all, the model and Lanczos resampling could perfectly upsample the low-resolution images without apparent pixel value change, as shown in **Figure 4-14**. The model was able to improve the image quality, mainly by denoising and eliminating artifacts. The model's features related to denoising and artifacts correction seem to be more relevant to improve these images than the upsampling.

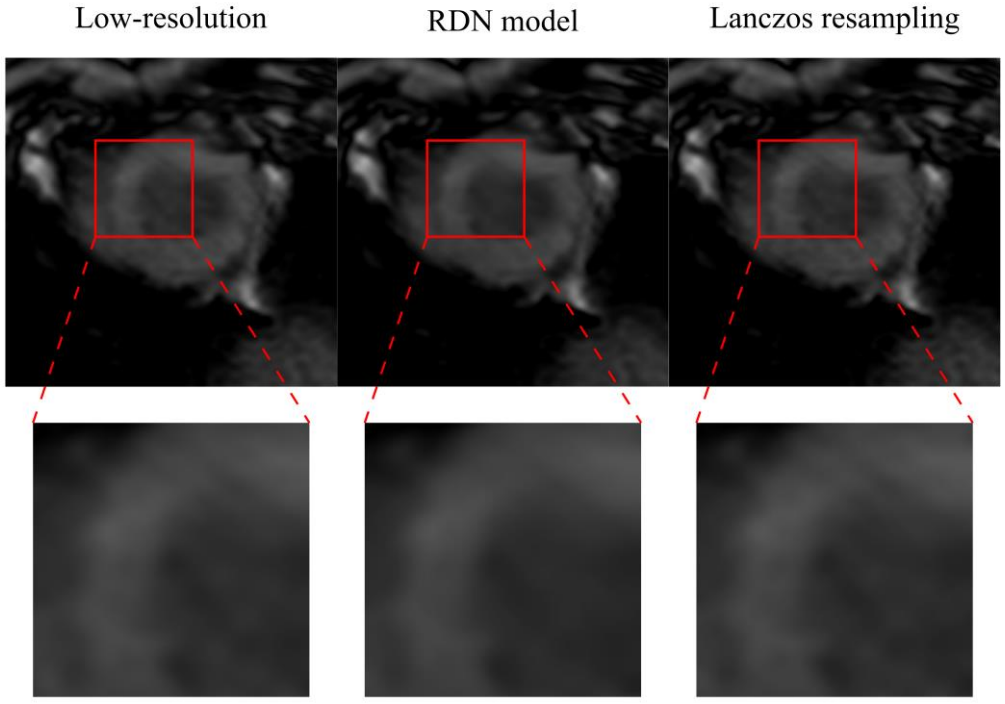

Figure 4-14 – T1-weighted image acquired with 3D SACORA from pig two and upsampled with the model and Lanczos resampling.

The final goal was to improve the image quality of the 3D SACORA T1 maps, which was achieved for all pigs, as can be visually assessed in **Figure 4-15**. Visually, the T1 maps obtained by the model are of much better quality than the ones obtained by Lanczos resampling. In this way, the model was able to improve the quality of both the T1-weighted images and the T1 maps.

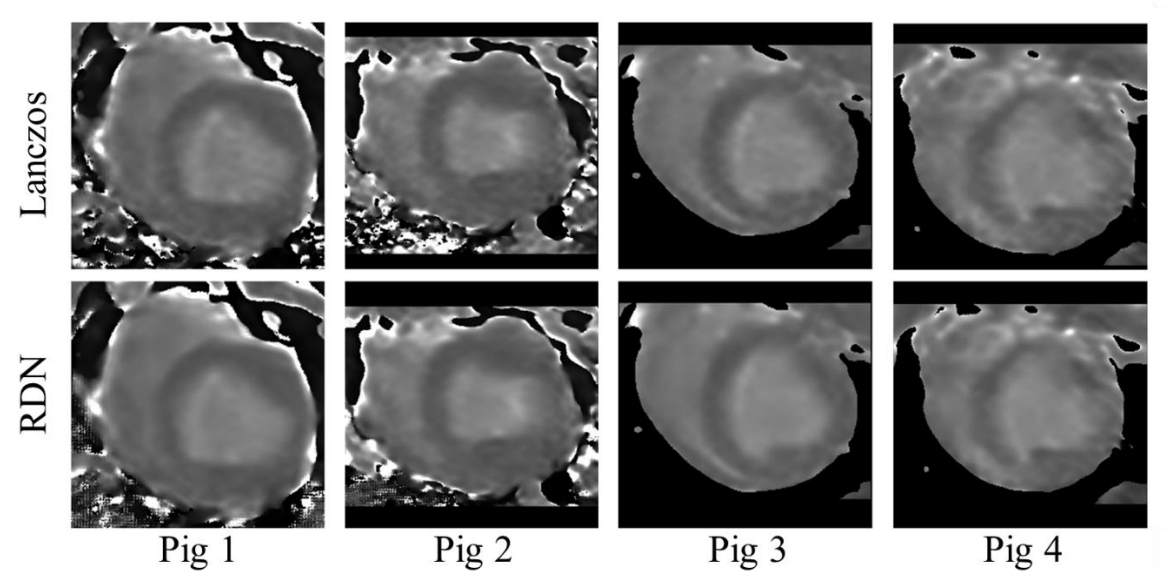

Figure 4-15 - T1 maps obtained by fitting the upsampled saturation time images (Lanczos and RDN) for the 3D SACORA sequence.

Analytically, the images obtained with the model also present better results, as shown in **Table 4-4**. The mean septal T1 of the four pigs is 1459.5 ± 61.3 ms for Lanczos and 1460,3 ± 55.6 ms for the RDN model, while the blood T1 is 2033.8 ± 67.3 ms and 2051.5 ± 59.2 ms, respectively. Hence, the RDN model achieved the same T1 values of Lanczos resampling but with better standard deviation (precision).

3D SACORA

	Myocardium				Blood			
	Lanczos		RDN		Lanczos		RDN	
	mean T1 (ms)	std (ms)	mean T1 (ms)	std (ms)	mean T1 (ms)	std (ms)	mean T1 (ms)	std (ms)
Pig1	1440,2	59,8	1434,0	50,0	2026,8	90,2	2044,6	80,0
Pig2	1423,6	55,4	1423,2	49,8	1984,2	68,0	2004,0	61,4
Pig3	1460,2	63,0	1465,0	58,2	2059,4	56,2	2076,6	45,6
Pig4	1514,0	66,8	1518,8	64,2	2064,6	54,6	2080,8	49,6
Mean	**1459,5**	**61,3**	**1460,3**	**55,6**	**2033,8**	**67,3**	**2051,5**	**59,2**

Table 4-4 – Mean T1 and standard deviation of the septal myocardium and blood pool of all pigs for Lanczos resampling and the RDN model (3D SACORA).

The denoising applied with the RDN model seems not to change the pixel values, as corroborated by **Figure 4-16**. The profile shows that the model could accurately eliminate the noise without changing the signal.

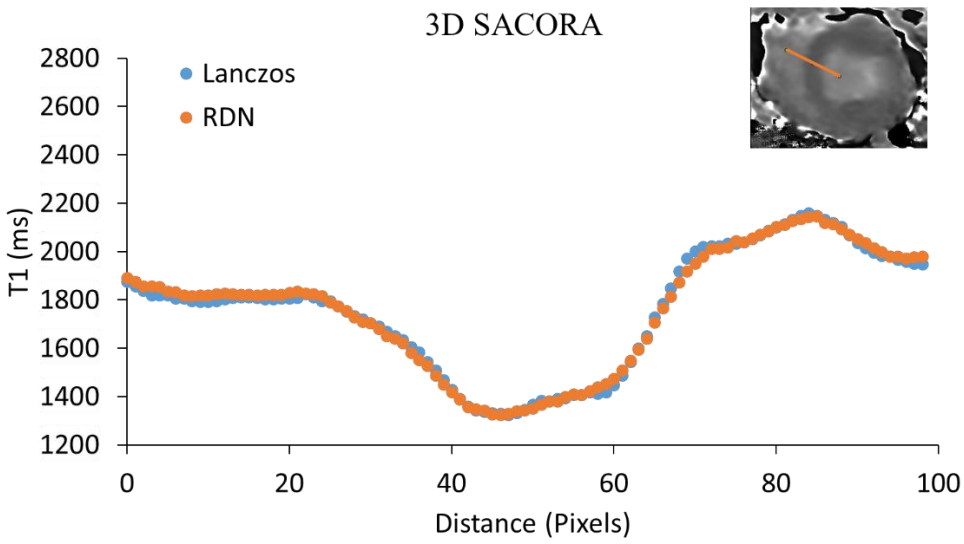

Figure 4-16 – Pixels profile of a 3D SACORA T1 map from pig two, after upsampling by Lanczos resampling and the RDN model.

3D SASHA

The RDN model was also tested with 3D SASHA images, which have different characteristics from the 3D SACORA images since 3D SASHA has a longer acquisition time, and consequently, the images presented higher SNR but also more cardiac motion artifacts. In order to evaluate the robustness of the model across different sequences, the T1-weighted images of 3D SASHA were also upsampled and denoised using the RDN model and Lanczos resampling. The T1-weighted images results show that the model improved the images without modifying the pixel values, being the ability to eliminate the motion artifacts the main advantage of using the model, as shown in **Figure 4-17**.

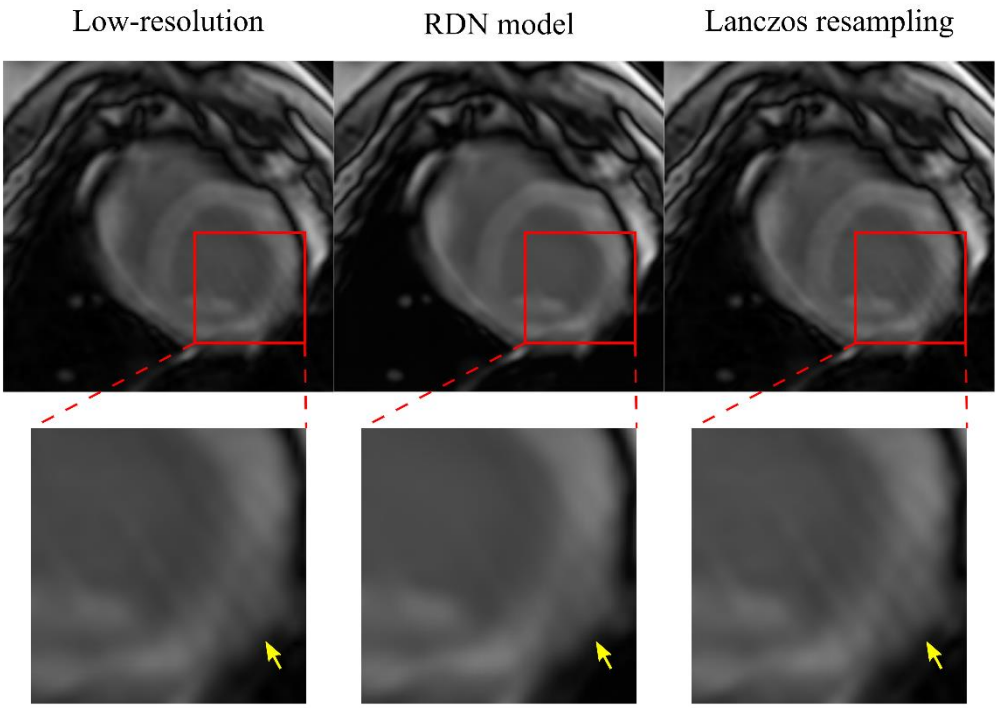

Figure 4-17 - T1-weighted image acquired with 3D SASHA from pig one and upsampled with the model and Lanczos resampling. The yellow arrow points to motion artifacts that were diminished by the model.

As expected from the improvements visible on the T1-weighted images, the T1 maps obtained with the model were much cleaner than those obtained with Lanczos resampling, as shown in **Figure 4-18**. Although the SNR of the 3D SASHA images is already excellent, the model could further denoise the T1 maps. More importantly, the model was also able to remove most of the motion artifacts.

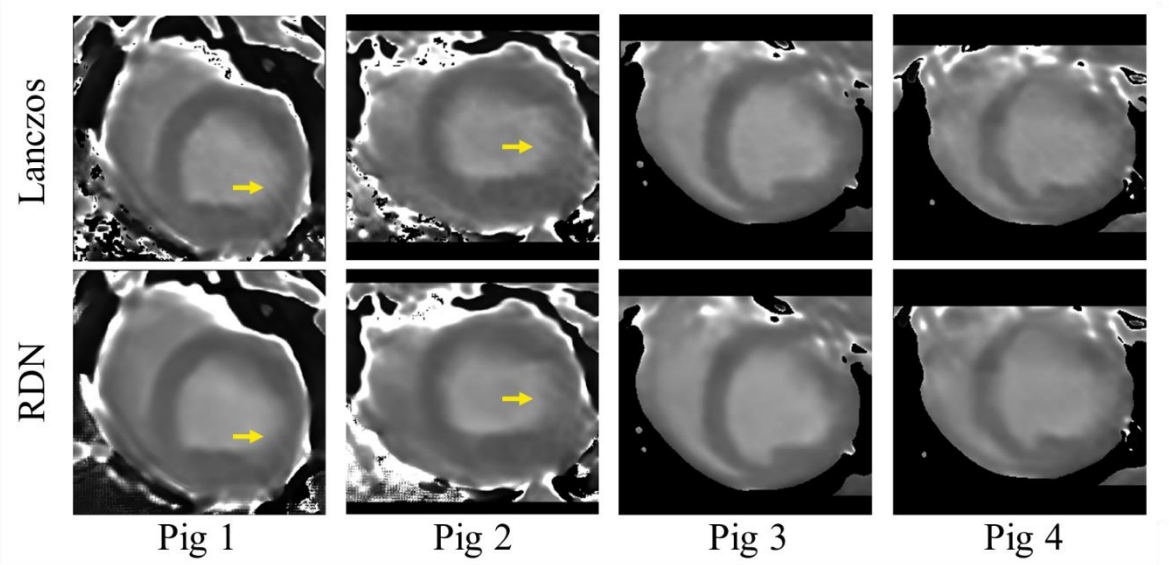

Figure 4-18 - T1 maps obtained by fitting the upsampled saturation time images (Lanczos and RDN) for the 3D SASHA sequence. The yellow arrow points to motion artifacts that were diminished by the model.

Analytically, the RDN model also achieved better results than Lanczos resampling, as shown in **Table 4-5**. The mean septal T1 of the four pigs is 1471.9 ± 50.9 ms for Lanczos and 1469,5 ± 50.4 ms for the RDN model, while the blood T1 is 2240.0 ± 74.0 ms and 2272.7 ± 70.3 ms, respectively. In this way, the RDN model was able to improve the standard deviation without considerably changing the T1 values.

3D SASHA

	Myocardium				Blood			
	Lanczos		RDN		Lanczos		RDN	
	mean T1 (ms)	std (ms)	mean T1 (ms)	std (ms)	mean T1 (ms)	std (ms)	mean T1 (ms)	std (ms)
Pig1	1418,4	42,2	1422,8	40,6	2210,8	72,2	2283,6	73,2
Pig2	1416,2	53,2	1414,0	48,6	2191,4	102,2	2224,4	95,8
Pig3	1501,8	50,6	1494,6	52,6	2332,2	58,4	2348,0	52,8
Pig4	1551,4	57,6	1546,4	59,6	2225,6	63,2	2234,6	59,4
Mean	**1471,9**	**50,9**	**1469,5**	**50,4**	**2240,0**	**74,0**	**2272,7**	**70,3**

Table 4-5 - Mean T1 and standard deviation of the septal myocardium and blood pool of all pigs for Lanczos resampling and the RDN model (3D SASHA).

The T1 values of the T1 maps obtained with both methods were also compared in **Figure 4-19**. The pixel profile shows that both methods achieved the same T1 values, and no resolution has been lost on the edges myocardium-blood by the denoising applied by the RDN model.

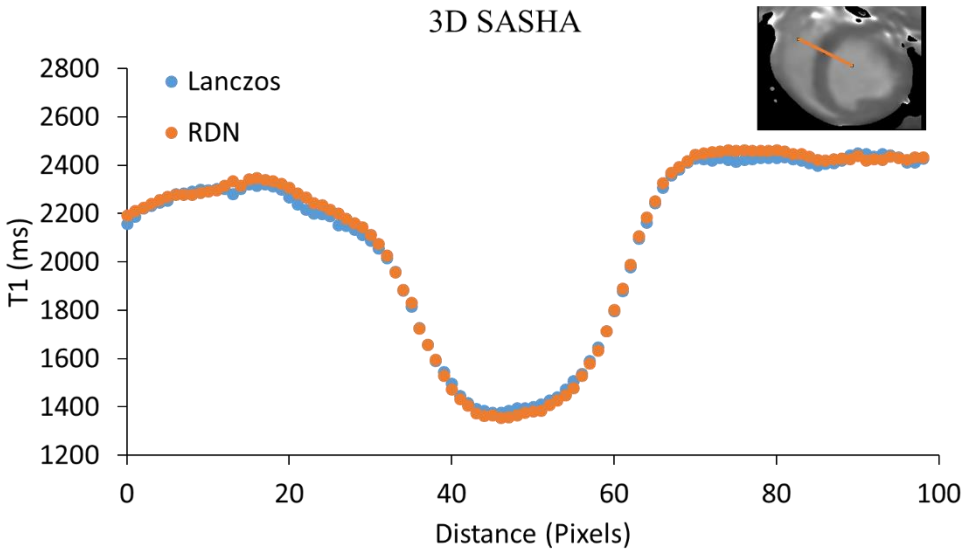

Figure 4-19 - Pixels profile of a 3D SASHA T1 map from pig three, after upsampling by Lanczos resampling and the RDN model.

CHAPTER 5

DISCUSSION

5.1. Single breath-hold saturation recovery 3D cardiac T1 mapping via compressed SENSE

3D SACORA (3D saturation-recovery compressed SENSE rapid acquisition) was developed as a new 3D T1 mapping sequence to speed up T1 mapping acquisition of the whole heart. The proposed sequence was validated in phantoms against the gold standard technique (IR-SE) and in-vivo against the reference 3D SASHA sequence.

3D SACORA successfully acquired a whole-heart 3D T1 map in a single breath-hold at 3T, estimating T1 values in agreement with those obtained with the IR-SE and 3D SASHA sequences. Thus, 3D SACORA's use of 5 saturation times for T1 fitting as well as k-space under-sampling via compressed SENSE enabled very short acquisition times (15s, for a heart rate of 60 bpm) without considerably compromising T1 estimation accuracy or image quality.

3D saturation recovery T1 mapping sequences have been developed recently because they do not require full longitudinal magnetization recovery and produce highly accurate T1 values. Acquisition times with these 3D sequences are however much longer than 20 s, and scans, therefore, cannot be performed under single breath-hold conditions. 3D SACORA was optimized to keep scan time shorter than 20 s without compromising T1 estimation accuracy, image quality, or LV coverage. Conditions established for this optimization included i) allowing enough time for the PD to achieve full magnetization recovery between readouts, ii) limiting the number of turbo field echo shots as much as possible, iii) optimizing trade-off between readout length and the compressed SENSE factor, iv) acquiring T1-weighted images with enough SNR for proper application of compressed SENSE, and v) acquiring a T1-weighted image with a saturation time as close as possible to the native cardiac T1 values at 3T.

3D SACORA is able to acquire a 3D T1 map in 15 heartbeats (heart rate, 60 bpm) at 3T. The main constraint for acquiring T1 maps with a short scan time at 3T is the recovery beats

required by the proton density. To mitigate this, 3D SACORA was designed to have just two readout shots. This was achieved by combining a shot length of ±210 ms with a compressed SENSE factor of 4.5, providing good image quality without major deterioration or blurring. A compressed SENSE factor of 4.5 guarantees good T1 estimation accuracy and precision, with comparable results to lower compressed SENSE factors, as shown in **Figure 3-2**. A shot length of ±210 ms is similar to the conventional 2D MOLLI shot length of ±190 ms [11] and shorter than the diastolic time length at very high heart rates (250 ± 59 ms at 128 ± 22 bpm) [75]. The PD readouts were separated by 6 s to guarantee full magnetization recovery. 3D SACORA acquires two T1-weighted images with long saturation times in order to enhance fitting quality for relevant cardiac T1 values at 3T. In addition, these images are ideal for applying compressed SENSE due to their high SNR, whereas T1-weighted images with shorter saturation times tend to be noisier, as shown in **Figure 4-3**.

3D SACORA and our own implementation of 3D SASHA were validated in phantom experiments. 3D SASHA is the reference sequence for in-vivo experiments in this study and has an acquisition time roughly 13 times longer than 3D SACORA. The phantom results show that 3D SACORA and 3D SASHA acquired 3D T1 maps with high accuracy and precision and in good agreement with IR-SE measurements. However, slight differences were found between 3D SACORA and 3D SASHA in specific cases (**Figure 4-2**). First, 3D SASHA is more precise than 3D SACORA for short T1s, due to the denser sampling of short saturation time T1-weighted images present in 3D SASHA. Second, 3D SACORA T1 estimation is, by design, less heart-rate sensitive than 3D SASHA. Heart-rate sensitivity in 3D SASHA acquisition is due to its lack of long saturation images, which can undermine T1 estimation quality, especially at high heart rates. Thus, the 3D SACORA sampling strategy was validated over a wide range of heart rates (50 bpm to 120 bpm). For heart rates outside this range, the sequence keeps acquiring saturation times at the low saturation time area of the T1 relaxation curve and close to the T1s of interest, as shown in **Table 3-1**. This sampling strategy of the saturation times makes 3D SACORA robust for a very wide range of heart rates.

The pig heart is an established model in cardiology due to its similarity to the human heart [76, 77]. In this study, in-vivo data were acquired before and after contrast administration.

The image quality in 3D SACORA was close to that obtained with 3D SASHA despite the much shorter acquisition time. All septal T1 measurements were similar in the two sequences (**Figure 4-5a, b**), despite the differences in sequence design and protocol. Furthermore, the mean septal pre-contrast T1 of 1453 ms estimated by 3D SACORA is in good agreement with published saturation recovery T1 measurements in pigs at 3T [62]. There was a slight discrepancy between 3D SACORA and 3D SASHA in T1s measured in the lateral and anterior segments of the myocardium (**Figure 4-4a, b**), probably caused by movement artifacts, which were more frequent in 3D SASHA due to the longer acquisition time.

In pigs, cardiac acquisitions performed in free-breathing are free of major respiratory artifacts [77, 78]. This was crucial for the successful comparison of 3D SACORA with 3D SASHA in a model without respiratory motion compensation (e.g., respiratory navigator [19] or motion correction [79]) or breath-hold acquisition. Nevertheless, the results might be improved by taking appropriate measures to minimize respiratory artifacts. For example, T1 map quality could be improved by reducing respiration-induced motion using registration approaches such as non-rigid image registration [80].

In this study, an in-house version of 3D SASHA [18] for 3T was used. As the reference sequence for the in-vivo experiments, the sampling strategy of the saturation times was similar to conventional 3D SASHA in order to acquire gold standard in-vivo T1 values. In addition, 3D SASHA was implemented with a shorter shot length than 3D SACORA, minimizing the effect of cardiac motion and reducing partial volume averaging, which are especially relevant for high heart rates. This sequence was validated successfully against IR-SE with phantom experiments, and the in-vivo results were in good agreement with published saturation recovery T1 measurements at 3T [19, 62].

Despite the good performance of 3D SACORA in post-contrast imaging, the sequence was primarily designed for pre-contrast imaging. Although post-contrast T1 values obtained with the proposed technique do not differ significantly from those obtained with 3D SASHA, the accuracy and precision of short T1 could be improved by increasing the number of short saturation images. The additional acquisition time could be compensated by decreasing the number of PD recovery beats.

One of the main limitations of this study for validating the novel T1 mapping sequence 3D SACORA is the lack of in-vivo human data. Nevertheless, the pig model is a well-established model for cardiac research, and in-vivo pig acquisitions can be performed under free-breathing conditions without significantly decreasing image quality [76–78]. Additionally, studies of new cardiac acquisitions have been successfully performed on pigs [29, 81–83]. A clinical study will be required to evaluate the performance of 3D SACORA (single breath-hold of 15s, for a heart rate of 60 bpm) in patients with ischemic and non-ischemic cardiomyopathies.

In short, the proposed 3D SACORA sequence acquired pre-contrast and post-contrast T1 maps of the whole heart with good accuracy, precision, and image quality for LV analysis at 3T. The sequence was optimized for speed and can acquire a 3D T1map in 15 heartbeats for a heart rate of 60 bpm.

Inspired by the performance of 3D SACORA, a feasibility study was performed to assess the potential of modifying the acquisition scheme of 3D SACORA in order to obtain T1 and T2 maps in a single breath-hold. Although this adds a whole new level of complexity, the possibility of using 3D SACORA concepts to acquire simultaneous, co-registered 3D T1 and T2 maps is exciting and could be groundbreaking. In this way, this proposed 3D T1/T2 sequence (3D dual-SACORA) was built on the main concepts of 3D SACORA: an optimized trade-off between readout length and compressed SENSE factor, acquisition of images with enough SNR for correct application of compressed SENSE, and the acquisition of at least one image with an acquisition time as close as possible to the native cardiac T1 values at 3T.

Initially, a preliminary 3D T1/T2 sequence was designed by modifying the least possible the 3D SACORA acquisition scheme and signal model. However, by design, this preliminary sequence may not provide T2-weighted images with enough SNR for accurate T2 mapping, particularly at high heart rates. The T2-weighted images could have such short saturation times that, together with the T2-preparation pulse, could lead to too much signal loss for accurate T2 mapping. This issue is extra challenging in single breath-hold acquisitions, which already have a complex trade-off between SNR and acquisition duration. Hence, after realizing that a simple modification of 3D SACORA was not the best option, this preliminary 3D T1/T2 sequence was modified to ensure adequate signal for T2 mapping. In this way, the

3D T1/T2 sequence proposed in this feasibility study (3D dual-SACORA) was designed to acquire T2-weighted images with an excellent SNR by not acquiring these images in the same RR interval of the saturation pulse, but using recovery beats according to the heart rate, acquiring the T2-weighted images as close as possible to the native cardiac T1 value at 3T (approximately 1500 ms). As the T2-weighted images have different saturation times in the 3D dual-SACORA sequence, the standard exponential signal model to estimate T2 is not applicable; instead, a combined signal model was used to jointly estimate T1 and T2.

The phantom results show that 3D dual-SACORA obtained parametric maps with high accuracy and precision, and in good agreement with the reference sequences. However, the accuracy for very long T2s (104 ms) was considerably lower than the other tested T2 values. This result is tolerable as 104 ms is much longer than the T2 of the myocardium, and it is challenging to predict very long T2s with a T2-preparation time of 45 ms. In general, 3D dual-SACORA tends to underestimate the values of both T1 and T2 slightly. This slight underestimation may come from the fact that T1 and T2 depend on each other, which may cause bias on T1 due to the T2-preparation pulse. Furthermore, the phantom was built with separate tubes for T1 and T2, which may cause additional modeling imperfection in a combined signal model as both relaxation parameters are used for the estimation.

The saturation time images and the parametric maps obtained with the 3D dual-SACORA sequence in the volunteer within a single breath-hold showed good contrast and homogeneity. The T2-weighted images presented excellent quality, showing that the use of recovering beats for acquiring T2-weighted images in saturation recovery sequences is auspicious and a valuable idea. The septal T1 values are in good agreement with published work such as Rui Guo et al. [19] and Kosuke Morita et al. [61], and the septal T2 values with works from Sofia Kvernby et al. [33] and Haikun Qi et al. [79]. Additionally, these septal values agree with the reference values estimated with MOLLI and GraSE, once taken into account the T1 underestimation of MOLLI [15]. Regarding the blood, there is apparently a slight underestimation of the T1 [34, 84], which may be caused by the bias on T1 due to the T2-preparation pulse or the long echo train length.

The preliminary findings of this feasibility study open the door to the possibility of using 3D SACORA concepts to develop a successful 3D T1/T2 sequence. Although 3D dual-

SACORA has room for improvement, the results show that a large study based on the proposed sequence is welcome and can be groundbreaking. To the best of our knowledge, 3D dual-SACORA is the first saturation recovery sequence using recovering beats for acquiring T2-weighted images. With this in mind, future work will be to test and optimize further the proposed sequence and perform a large study.

5.2. Improving image quality via a residual dense network (RDN)

A deep learning-based post-processing method was implemented to improve the image quality of MR images with the end goal of improving the T1 maps obtained with 3D SACORA. In this way, a comprehensive study of the performance of the method on MR images was performed by validating it across different MR datasets and T1 sequences.

After careful research of the several deep learning methods that could be applied to improve the T1 maps of 3D SACORA, the Residual Dense Network (RDN) was selected [56]. This convolutional neural network model has demonstrated outstanding performance on image super-resolution and denoising benchmark real-world image datasets [55, 56, 69], and is considered a state-of-the-art method in single-image-super-resolution. Super-resolution aims to obtain high-resolution images from small spatial resolution images or degraded images, such as blurry and noisy images. The possibility of improving MR image quality using super-resolution through the RDN model is appealing and scientifically relevant. In this way, although the focus is on improving the T1 maps of 3D SACORA, the model was used on different MR datasets from various sequences, providing broad information about the model's versatility and performance.

Firstly, the model was validated with benchmark MR datasets, performing an initial feasibility test of the model's performance with MR images. The model was separately tested with a benchmark brain dataset and a benchmark cardiac dataset to perform an image quality assessment of the MR images improved by the model. The model improved the images successfully for both datasets, achieving better performance with the brain dataset than with the cardiac dataset. This result was expected as the brain dataset's high-resolution images presented a better resolution and quality than those of the cardiac dataset. Additionally, the

brain images have more well-defined edges than the cardiac images, making the resolution enhancement more evident.

Secondly, a robust self-acquired cardiac dataset was acquired and prepared for guaranteeing high-quality, high-resolution images for training the model. This experiment aimed to test the performance of the RDN model on self-acquired cardiac images. The results showed improved image quality assessment metrics and visual assessment, particularly on well-defined edges. These results validate the use of these acquired high-resolution images to improve the saturation time images.

Lastly, a larger self-acquired cardiac dataset was used to train the RDN model, and the model was tested on improving the saturation time images and, consequently, the T1 maps. As described before, 3D saturation recovery compressed SENSE rapid acquisition (3D SACORA) has been recently proposed to perform single breath-hold T1 mapping of the left ventricle [51]. Although this sequence acquires good quality T1 maps, the possibility of improving the T1 maps of 3D SACORA without compromising the correct estimation of T1 values would be a breakthrough. In addition to the rapid acquisition 3D SACORA, the longer acquisition 3D saturation recovery single-shot acquisition (3D SASHA) [18] was also used in this study to validate the model in two different 3D T1 mapping sequences, providing information regarding the versatility of the model and opening doors to the application of the model on other parametric mapping sequences. For both 3D SACORA and 3D SASHA, the model improved the image quality of the saturation time images and the T1 maps. The model was able to decrease the noise and eliminate motion artifacts, enhancing the T1 maps analytically and visually. Analytically, the model did not considerably modify the T1 values while improving the standard deviation in both myocardium and blood. Visually, the model improved the T1 maps by removing the noise and motion artifacts without losing resolution on the edges. The enhancement of the saturation time images and T1 maps seemed to be more related to the denoising and artifacts correction than to the upsampling, which may be explained by the already decent resolution of the saturation time images. The capability of the model to learn that the motion artifacts should not be present on the images is an exciting and auspicious result.

In this last experiment, Rician noise was added to the low-resolution images to create noisy MR images and teach the model how to go from noisy to clean MR images. Rician noise was chosen as it has been shown that the noise in magnitude MR images is governed by a Rician distribution, and it is common practice to corrupt MR images with Rician noise to simulate noisy MR images [85, 86].

The image interpolation method used in this study for resampling tasks was Lanczos resampling [54]. Lanczos is a state-of-the-art standard method widely used in real-world applications. Other traditional interpolation methods are also commonly applied, such as nearest-neighbor, bilinear, and bicubic interpolation. Lanczos resampling was chosen for the resampling tasks because recent AI studies with MR images have applied Lanczos resampling as the reference baseline method, with Lanczos achieving better results than the other baseline methods [87, 88]. Generally speaking, Lanczos resampling preserves better the sharp lines with the main drawback of being more computationally expensive.

The loss function used in this study was the L1 loss. The L1 loss is widespread in super-resolution mainly because it is robust against outliers, discourages blurring, and provides good convergence [56, 70, 71]. In the first experiment, the L1 loss was compared against the more complex PSNR loss, which is promising and has shown excellent results in image enhancement [72]. The results showed that the L1 loss achieved better metrics than the PSNR loss in this experiment, and therefore, the L1 loss was used thereafter. The L1 loss provided excellent convergence and good image quality in all experiments, corroborating that the L1 loss is an excellent choice for the RDN model [56, 89].

This study's goal was accomplished as the RDN model improved the 3D SACORA T1 maps' quality considerably without compromising the estimation of T1 values. However, the potential for improvement is hard to predict due to the extreme complexity of the topic. For instance, a reasonable amount of modifications could potentially improve the results, such as increasing the amount and quality of the images of the dataset, changing the type of images of the dataset (e.g., resolution, orientation), changing the resampling factor, choosing a different loss function, choosing a different CNN model, and changing the hyperparameters.

Future work in the short term will focus on using the trained model in different parametric mapping sequences as the model performed well in both 3D SACORA and 3D SASHA,

showing the versatility and robustness of the trained model. In the long run, the goal is to obtain the maps directly from the model, which means that this new model will need to improve the saturation time images and also perform the signal model fitting. Another exciting project is to implement a super-resolution model that uses the k-space data of the MR images. This would potentially improve the results and provide more possibilities for creating the low-resolution images, allowing more straightforward modification of resolution and noise.

In conclusion, a deep learning based super-resolution model was successfully implemented to improve the image quality of the T1 maps of 3D SACORA, and a comprehensive study of the performance of the model in different MR image datasets and sequences corroborated its capability to improve MR images.

CHAPTER 6

CONCLUSION AND FUTURE LINES OF RESEARCH

Groundbreaking developments such as 3D techniques, parallel imaging, compressed sensing, and AI have continuously advanced the CMR field. These developments provide new tools to upgrade and improve parametric mapping sequences, en route to decrease acquisition time, improve spatial resolution, and increase the coverage of the heart. Inspired by the need to develop novel high-quality parametric sequences for 3T, this thesis's main goal was to introduce an accurate and efficient 3D single breath-hold MR methodology for measuring cardiac parametric mapping on a 3T clinical scanner.

This thesis proposed and validated the 3D saturation-recovery compressed SENSE rapid acquisition (3D SACORA) imaging sequence, a new single breath-hold 3D T1 mapping technique at 3T. This sequence was developed by optimizing together several concepts such as 3D imaging, saturation recovery, compressed SENSE, and recovering beats to acquire images as close as possible to the cardiac T1 values at 3T. The sequence provided good quality single breath-hold saturation recovery 3D T1 mapping at 3T and stability over a wide range of heart rates, making it an auspicious and competitive new player in the 3D T1 mapping field.

Following the good results of 3D SACORA, a feasibility study was performed to assess the potential of modifying its acquisition scheme in order to obtain 3D T1 and T2 maps simultaneously in a single breath-hold. The findings of this feasibility study showed that a promising 3D T1/T2 sequence, named 3D dual-SACORA, was successfully developed, and a more extensive study would be welcome to optimize further the sequence and assess its performance thoroughly. Introduced in 3D dual-SACORA, the novel idea of using recovering beats in a saturation recovery sequence to acquire T2-weighted images is particularly unique and can be groundbreaking.

Last but not least, this thesis implemented a deep learning-based post-processing method (RDN model) to improve the image quality of MR images with the end goal of improving

the T1 maps obtained with 3D SACORA. A comprehensive study of the model's performance in different MR image datasets and sequences showed its capability to improve MR images and T1 maps by increasing resolution, reducing noise, and eliminating artifacts. The model was able to take 3D SACORA T1 maps' quality to a whole new level by correcting many of the issues of acquiring 3D T1 maps in a single breath-hold, opening the door to the possibility of using deep learning-based post-processing models to improve MR images on a regular basis.

In short, a 3D single breath-hold MR methodology was introduced for measuring cardiac parametric mapping on a 3T clinical scanner. This methodology includes a ready-to-go 3D single breath-hold T1 mapping sequence for 3T (3D SACORA); the ideas for an upgrade of 3D SACORA, which led to a very promising preliminary 3D T1/T2 mapping sequence (3D dual-SACORA); and a deep learning-based post-processing implementation able to improve the image quality of 3D SACORA T1 maps.

Future lines of research derived from this thesis may involve:

- 3D SACORA was validated in pigs in this work; the next step is a clinical study to evaluate the performance of 3D SACORA in healthy volunteers and patients with ischemic and non-ischemic cardiomyopathies.
- Despite the good performance of 3D SACORA in post-contrast imaging, the sequence was primarily designed for pre-contrast imaging. A 3D SACORA version for post-contrast imaging could be achieved with a minor modification of the acquisition scheme as the accuracy and precision of short T1 could be improved by increasing the number of short saturation time images.
- The PD readouts were separated by 6 s to guarantee full magnetization recovery and be on the safe side; however, decreasing the number of PD recovery beats might be an excellent approach to further decreasing the acquisition time.
- The feasibility study of the 3D dual-SACORA sequence showed that a large study based on this proposed sequence could be groundbreaking, and therefore, future work could include testing and optimizing further this sequence and perform a large study.
- The trained RDN model could be tested in different parametric mapping sequences as the model performed well in both 3D SACORA and 3D SASHA.

- An exciting improvement would be obtaining the maps directly from a super-resolution model, which means that this new model would need to improve the saturation time images and also perform the signal model fitting.
- Another exciting project would be implementing a super-resolution model that uses the 3D SACORA images' k-space data and benchmark it against the current implementation.

Based on the results described in this thesis, the conclusions can be summarized as follows:

1) This thesis proposed the 3D SACORA imaging sequence, a ready-to-go new single breath-hold 3D T1 mapping technique at 3T. 3D SACORA was optimized to keep scan time around 15 s without compromising T1 estimation accuracy, image quality, or LV coverage.
2) 3D SACORA was carefully validated in phantoms against the gold standard technique IR-SE and in-vivo against the reference technique 3D SASHA. The sequence provided good quality 3D T1 mapping at 3T and stability over a wide range of heart rates, making it an auspicious and competitive new player in 3D T1 mapping at 3T.
3) Following the good results of 3D SACORA, a feasibility study was performed to assess the possibility of adding a T2 mapping feature to the 3D SACORA sequence without substantially increasing the acquisition time. The findings of this feasibility study showed that a promising 3D T1/T2 sequence, named 3D dual-SACORA, was successfully developed, and a more extensive study to validate further this sequence would be valuable.
4) Lastly, a deep learning-based post-processing method (RDN model) was used to improve the image quality of MR images with the end goal of improving the T1 maps obtained with 3D SACORA. The model was able to improve MR images and T1 maps by increasing resolution, reducing noise, and eliminating artifacts. Specifically, 3D SACORA T1 maps' quality was notably improved, opening the door for using deep learning-based post-processing models as a standard MR image enhancement approach.

REFERENCES

1. Purcell EM, Torrey HC, Pound RV (1946) Resonance Absorption by Nuclear Magnetic Moments in a Solid. Phys Rev 69:37–38.

2. Bloch F (1946) Nuclear Induction. Phys Rev 70:460–474.

3. Lauterbur PC (1973) Image Formation by Induced Local Interactions: Examples Employing Nuclear Magnetic Resonance. Nature 242:190–191.

4. Mansfield P, Grannell PK (1973) NMR 'diffraction' in solids? J Phys C Solid State Phys 6:L422–L426.

5. Westbrook C (2002) MRI at a Glance. Wiley-Blackwell.

6. Suetens P (2009) Fundamentals of Medical Imaging. Cambridge University Press.

7. McRobbie DW, Moore EA, Graves MJ, Prince MR (2006) MRI from Picture to Proton, 2nd ed. Cambridge: Cambridge University Press.

8. Elmaoğlu M, Çelik A (2012) MRI Handbook. MR Physics, Patient Positioning, and Protocols, 2nd ed. Springer-Verlag.

9. Kwong RY, Jerosch-Herold M, Heydari B (2018) Cardiovascular Magnetic Resonance Imaging, 2nd ed. Springer.

10. Brown MA, Semelka RC (2003) MRI: Basic Principles and Applications. Wiley.

11. Messroghli DR, Radjenovic A, Kozerke S, Higgins DM, Sivananthan MU, Ridgway JP (2004) Modified Look-Locker inversion recovery (MOLLI) for high-resolution T1 mapping of the heart. Magn Reson Med 52:141–146.

12. Chow K, Flewitt JA, Green JD, Pagano JJ, Friedrich MG, Thompson RB (2014) Saturation recovery single-shot acquisition (SASHA) for myocardial T1 mapping. Magn Reson Med 71:2082–2095.

13. Weingärtner S, Akçakaya M, Basha T, Kissinger KV, Goddu B, Berg S, Manning WJ, Nezafat R (2014) Combined saturation/inversion recovery sequences for improved evaluation of scar and diffuse fibrosis in patients with arrhythmia or heart rate variability. Magn Reson Med 71:1024–1034.

14. Cameron D, Vassiliou VS, Higgins DM, Gatehouse PD (2018) Towards accurate and precise T 1 and extracellular volume mapping in the myocardium: a guide to current pitfalls and their solutions. Magn Reson Mater Phys Biol Med 31:143–163.

15. Kellman P, Hansen MS (2014) T1-mapping in the heart: accuracy and precision. J Cardiovasc Magn Reson 16:2.

16. Piechnik SK, Neubauer S, Ferreira VM (2018) State-of-the-art review: stress T1 mapping—technical considerations, pitfalls and emerging clinical applications. Magn Reson Mater Phys Biol Med 31:131–141.

17. Song T, Stainsby JA, Ho VB, Hood MN, Slavin GS (2012) Flexible cardiac T1 mapping using a modified look–locker acquisition with saturation recovery. Magn Reson Med 67:622–627.

18. Nordio G, Henningsson M, Chiribiri A, Villa ADM, Schneider T, Botnar RM (2017) 3D myocardial T 1 mapping using saturation recovery. J Magn Reson Imaging 46:218–227.

19. Guo R, Chen Z, Wang Y, Herzka DA, Luo J, Ding H (2018) Three-dimensional free breathing whole heart cardiovascular magnetic resonance T1 mapping at 3 T. J Cardiovasc Magn Reson 20.1: 64.

20. Nordio G, Bustin A, Henningsson M, Rashid I, Chiribiri A, Ismail T, Odille F, Prieto C, Botnar RM (2018) 3D SASHA myocardial T1 mapping with high accuracy and improved precision. Magn Reson Mater Phys Biol Med 32.2: 281-289.

21. Nordio G, Schneider T, Cruz G, Correia T, Bustin A, Prieto C, Botnar RM, Henningsson M (2020) Whole-heart T 1 mapping using a 2D fat image navigator for respiratory motion compensation. Magn Reson Med 83.1: 178-187.

22. Stainsby JA, Slavin GS (2014) Comparing the accuracy and precision of SMART1Map, SASHA and MOLLI. J Cardiovasc Magn Reson 16:P11.

23. Jogiya R, Schuster A, Zaman A, Motwani M, Kouwenhoven M, Nagel E, Kozerke S, Plein S (2014) Three-dimensional balanced steady state free precession myocardial perfusion cardiovascular magnetic resonance at 3T using dual-source parallel RF transmission: initial experience. J Cardiovasc Magn Reson 16:90.

24. Gensler D, Mörchel P, Fidler F, Ritter O, Quick HH, Ladd ME, Bauer WR, Ertl G, Jakob PM, Nordbeck P (2015) Myocardial T1: Quantification by Using an ECG-triggered Radial Single-Shot Inversion-Recovery MR Imaging Sequence. Radiology 274:879–887.

25. Shao J, Rapacchi S, Nguyen K-L, Hu P (2016) Myocardial T1 Mapping at 3.0T Using an Inversion Recovery Spoiled Gradient Echo Readout and Bloch Equation Simulation with Slice Profile Correction (BLESSPC) T1 Estimation Algorithm. J Magn Reson Imaging 43:414–425.

26. Schild HH (1990) MRI, Made Easy: (... Well Almost). Schering AG.

27. Kim PK, Hong YJ, Im DJ, Suh YJ, Park CH, Kim JY, Chang S, Lee H-J, Hur J, Kim YJ, Choi BW (2017) Myocardial T1 and T2 Mapping: Techniques and Clinical Applications. Korean J Radiol 18:113–131.

28. Oshio K, Feinberg DA (1991) GRASE (Gradient-and Spin-Echo) imaging: A novel fast MRI technique. Magn Reson Med 20:344–349.

29. Fernández-Jiménez R, Sánchez-González J, Aguero J, del Trigo M, Galán-Arriola C, Fuster V, Ibáñez B (2015) Fast T2 gradient-spin-echo (T2-GraSE) mapping for myocardial edema quantification: first in vivo validation in a porcine model of ischemia/reperfusion. J Cardiovasc Magn Reson 17.1: 92.

30. Giri S, Chung Y-C, Merchant A, Mihai G, Rajagopalan S, Raman SV, Simonetti OP (2009) T2 quantification for improved detection of myocardial edema. J Cardiovasc Magn Reson 11:56.

31. Ding H, Fernandez-de-Manuel L, Schär M, Schuleri KH, Halperin H, He L, Zviman MM, Beinart R, Herzka DA (2015) Three-dimensional whole-heart T_2 mapping at 3T: 3D Myocardial T_2 Mapping. Magn Reson Med 74:803–816.

32. Akçakaya M, Weingärtner S, Basha TA, Roujol S, Bellm S, Nezafat R (2016) Joint Myocardial T1 and T2 Mapping Using a Combination of Saturation Recovery and T2-preparation. Magn Reson Med 76:888–896.

33. Kvernby S, Warntjes MJB, Haraldsson H, Carlhäll C-J, Engvall J, Ebbers T (2014) Simultaneous three-dimensional myocardial T1 and T2 mapping in one breath hold with 3D-QALAS. J Cardiovasc Magn Reson 16:102.

34. Guo R, Chen Z, Herzka DA, Luo J, Ding H (2019) A three-dimensional free-breathing sequence for simultaneous myocardial T_1 and T_2 mapping. Magn Reson Med 81:1031–1043.

35. Roujol S, Foppa M, Weingartner S, Manning WJ, Nezafat R (2015) Adaptive Registration of Varying Contrast-Weighted Images for Improved Tissue Characterization (ARCTIC): Application to T1 Mapping. Magn Reson Med 73:1469–1482.

36. Deichmann R, Haase A (1992) Quantification of T1 values by SNAPSHOT-FLASH NMR imaging. J Magn Reson 1969 96:608–612.

37. Messroghli DR, Moon JC, Ferreira VM, Grosse-Wortmann L, He T, Kellman P, Mascherbauer J, Nezafat R, Salerno M, Schelbert EB, Taylor AJ, Thompson R, Ugander M, van Heeswijk RB, Friedrich MG (2017) Clinical recommendations for cardiovascular magnetic resonance mapping of T1, T2, T2* and extracellular volume: A consensus statement by the Society for Cardiovascular Magnetic Resonance (SCMR) endorsed by the European Association for Cardiovascular Imaging (EACVI). J Cardiovasc Magn Reson 19.1: 1-24.

38. Pruessmann KP, Weiger M, Scheidegger MB, Boesiger P (1999) SENSE: Sensitivity encoding for fast MRI. Magn Reson Med 42:952–962.

39. Griswold MA, Jakob PM, Heidemann RM, Nittka M, Jellus V, Wang J, Kiefer B, Haase A (2002) Generalized autocalibrating partially parallel acquisitions (GRAPPA). Magn Reson Med 47:1202–1210.

40. Donoho DL (2006) Compressed sensing. IEEE Trans Inf Theory 52:1289–1306.

41. Geerts-Ossevoort L, de Weerdt E, Duijndam A, van IJperen G, Peeters H, Doneva M, Nijenhuis M, Huang A (2020) Speed done right. Every time.

42. Candès EJ, Romberg JK, Tao T (2006) Stable signal recovery from incomplete and inaccurate measurements. Commun Pure Appl Math 59:1207–1223.

43. Candes EJ, Romberg J, Tao T (2006) Robust uncertainty principles: exact signal reconstruction from highly incomplete frequency information. IEEE Trans Inf Theory 52:489–509.

44. Lustig M, Donoho D, Pauly JM (2007) Sparse MRI: The application of compressed sensing for rapid MR imaging. Magn Reson Med 58:1182–1195.

45. Liu J, Feng L, Shen H-W, Zhu C, Wang Y, Mukai K, Brooks GC, Ordovas K, Saloner D (2017) Highly-accelerated self-gated free-breathing 3D cardiac cine MRI: validation in assessment of left ventricular function. Magn Reson Mater Phys Biol Med 30:337–346.

46. Weingärtner S, Akçakaya M, Roujol S, Basha T, Tschabrunn C, Berg S, Anter E, Nezafat R (2015) Free-breathing combined three-dimensional phase sensitive late gadolinium enhancement and T_1 mapping for myocardial tissue characterization: Integrated Sequence for 3D LGE Imaging and 3D T_1 Mapping. Magn Reson Med 74:1032–1041.

47. Wetzl J, Schmidt M, Pontana F, Longère B, Lugauer F, Maier A, Hornegger J, Forman C (2018) Single-breath-hold 3-D CINE imaging of the left ventricle using Cartesian sampling. Magn Reson Mater Phys Biol Med 31:19–31.

48. Vranic JE, Cross NM, Wang Y, Hippe DS, Weerdt E de, Mossa-Basha M (2019) Compressed Sensing–Sensitivity Encoding (CS-SENSE) Accelerated Brain Imaging: Reduced Scan Time without Reduced Image Quality. Am J Neuroradiol 40:92–98.

49. Zibulevsky M, Elad M (2010) L1-L2 Optimization in Signal and Image Processing. IEEE Signal Process Mag 27:76–88.

50. Ma Y, Hou Y, Ma Q, Wang X, Sui S, Wang B (2019) Compressed SENSE single-breath-hold and free-breathing cine imaging for accelerated clinical evaluation of the left ventricle. Clin Radiol 74.4: 325. e9-325. e17.

51. Ferreira da Silva T, Galan-Arriola C, Montesinos P, López-Martín GJ, Desco M, Fuster V, Ibáñez B, Sanchez-Gonzalez J (2020) Single breath-hold saturation recovery 3D cardiac T1 mapping via compressed SENSE at 3T. Magn Reson Mater Phys Biol Med 33.6: 865-876.

52. Sasi S D, Ramaniharan AK, Bhattacharjee R, Gupta RK, Saha I, Van Cauteren M, Shah T, Gopalakrishnan K, Gupta A, Singh A (2020) Evaluating feasibility of high resolution T1-perfusion MRI with whole brain coverage using compressed SENSE: Application to glioma grading. Eur J Radiol 129:109049.

53. Leiner T, Rueckert D, Suinesiaputra A, Baeßler B, Nezafat R, Išgum I, Young AA (2019) Machine learning in cardiovascular magnetic resonance: basic concepts and applications. J Cardiovasc Magn Reson 21:61.

54. Duchon CE (1979) Lanczos Filtering in One and Two Dimensions. J Appl Meteorol 18:1016–1022.

55. Wang Z, Chen J, Hoi SCH (2020) Deep Learning for Image Super-resolution: A Survey. IEEE Trans Pattern Anal Mach Intell.

56. Zhang Y, Tian Y, Kong Y, Zhong B, Fu Y (2018) Residual Dense Network for Image Super-Resolution. Proc. IEEE Comput. Soc. Conf. Comput. Vis. Pattern Recognit, pp 2472-2481.

57. He K, Zhang X, Ren S, Sun J (2016) Deep Residual Learning for Image Recognition. Proc. IEEE Comput. Soc. Conf. Comput. Vis. Pattern Recognit, pp 770-778.

58. Huang G, Liu Z, van der Maaten L, Weinberger KQ (2018) Densely Connected Convolutional Networks. Proc. IEEE Comput. Soc. Conf. Comput. Vis. Pattern Recognit, pp 4700-4708.

59. Timmis A, Townsend N, Gale CP, Torbica A, Lettino M, Petersen SE, Mossialos EA, Maggioni AP, Kazakiewicz D, May HT, De Smedt D, Flather M, Zuhlke L, Beltrame JF, Huculeci R, Tavazzi L, Hindricks G, Bax J, Casadei B, Achenbach S, Wright L, Vardas P (2020) European Society of Cardiology: Cardiovascular Disease Statistics 2019. Eur Heart J 41:12–85.

60. Akçakaya M, Weingärtner S, Roujol S, Nezafat R (2015) On the Selection of Sampling Points for Myocardial T1 Mapping. Magn Reson Med 73:1741–1753.

61. Morita K, Oda S, Utsunomiya D, Nakaura T, Matsubara T, Goto M, Okuaki T, Yuki H, Nagayama Y, Kidoh M, Hirata K, Iyama Y, Taguchi N, Hatemura M, Hashida M, Yamashita Y (2017) Saturation Recovery Myocardial T1 Mapping with a Composite Radiofrequency Pulse on a 3T MR Imaging System. Magn Reson Med Sci 17:35–41.

62. Chow K, Kellman P, Spottiswoode BS, Nielles-Vallespin S, Arai AE, Salerno M, Thompson RB (2015) Saturation pulse design for quantitative myocardial T1 mapping. J Cardiovasc Magn Reson 17.1: 84.

63. Busse RF, Riederer SJ (2001) Steady-state preparation for spoiled gradient echo imaging. Magn Reson Med 45:653–661.

64. Warntjes MJ, Kihlberg J, Engvall J (2010) Rapid T1 quantification based on 3D phase sensitive inversion recovery. BMC Med Imaging 10.1:19.

65. Li W, Griswold M, Yu X (2010) Rapid T1 Mapping of Mouse Myocardium with Saturation Recovery Look-Locker Method. Magn Reson Med 64.5:1296–1303.

66. Passing H, Bablok W (1983) A New Biometrical Procedure for Testing the Equality of Measurements from Two Different Analytical Methods. Application of linear regression procedures for method comparison studies in Clinical Chemistry, Part I. J Clin Chem Clin Biochem 21:709-720.

67. Altman DG, Bland JM (1983) Measurement in Medicine: The Analysis of Method Comparison Studies. J R Stat Soc Series D (The Statistician) 32.3:307-317.

68. Cardinale F, et al. (2018) ISR. https://github.com/idealo/image-super-resolution, last access: July 2020.

69. Zhang Y, Tian Y, Kong Y, Zhong B, Fu Y (2020) Residual Dense Network for Image Restoration. IEEE Trans Pattern Anal Mach Intell.

70. Isola P, Zhu J-Y, Zhou T, Efros AA (2017) Image-to-Image Translation with Conditional Adversarial Networks. Proc. IEEE Comput. Soc. Conf. Comput. Vis. Pattern Recognit, pp 1125-1134.

71. Lim B, Son S, Kim H, Nah S, Lee KM (2017) Enhanced Deep Residual Networks for Single Image Super-Resolution. Proc. IEEE Comput. Soc. Conf. Comput. Vis. Pattern Recognit workshops, pp 136–144.

72. Huang H, Tao H, Wang H (2019) A convolutional neural network based method for low-illumination image enhancement. Proc. 2nd Int. Conf. Artif. Intell. Pattern Recognit, pp 72–77.

73. Pace DF, Dalca AV, Geva T, Powell AJ, Moghari MH, Golland P (2015) Interactive Whole-Heart Segmentation in Congenital Heart Disease. In: Navab N, Hornegger J, Wells WM, Frangi AF (eds) Med. Image Comput. Comput.-Assist. Interv. Springer International Publishing, Cham, pp 80–88.

74. Wang Z, Bovik AC, Sheikh HR, Simoncelli EP (2004) Image Quality Assessment: From Error Visibility to Structural Similarity. IEEE Trans Image Process 13:600–612.

75. Bombardini T, Gemignani V, Bianchini E, Venneri L, Petersen C, Pasanisi E, Pratali L, Alonso-Rodriguez D, Pianelli M, Faita F, Giannoni M, Arpesella G, Picano E (2008) Diastolic time – frequency relation in the stress echo lab: filling timing and flow at different heart rates. Cardiovasc Ultrasound 6:15.

76. García-Álvarez A, García-Lunar I, Pereda D, Fernández-Jimenez R, Sánchez-González J, Mirelis JG, Nuño-Ayala M, Sánchez-Quintana D, Fernández-Friera L, García-Ruiz JM, Pizarro G, Agüero J, Campelos P, Castellá M, Sabaté M, Fuster V, Sanz J, Ibañez B (2015) Association of Myocardial T1-Mapping CMR With Hemodynamics and RV Performance in Pulmonary Hypertension. JACC Cardiovasc Imaging 8:76–82.

77. Galán-Arriola C, Lobo M, Vílchez-Tschischke JP, López GJ, de Molina-Iracheta A, Pérez-Martínez C, Agüero J, Fernández-Jiménez R, Martín-García A, Oliver E, Villena-Gutierrez R, Pizarro G, Sánchez PL, Fuster V, Sánchez-González J, Ibanez B (2019) Serial Magnetic Resonance Imaging to Identify Early Stages of Anthracycline-Induced Cardiotoxicity. J Am Coll Cardiol 73:779–791.

78. Fernández-Jiménez Rodrigo, Galán-Arriola Carlos, Sánchez-González Javier, Agüero Jaume, López-Martín Gonzalo J., Gomez-Talavera Sandra, Garcia-Prieto Jaime, Benn Austin, Molina-Iracheta Antonio, Barreiro-Pérez Manuel, Martin-García Ana, García-Lunar Inés, Pizarro Gonzalo, Sanz Javier, Sánchez Pedro L., Fuster Valentin, Ibanez Borja (2017) Effect of Ischemia Duration and Protective Interventions on the Temporal Dynamics of Tissue Composition After Myocardial Infarction. Circ Res 121:439–450.

79. Qi H, Bustin A, Cruz G, Jaubert O, Chen H, Botnar RM, Prieto C (2019) Free-running simultaneous myocardial T1/T2 mapping and cine imaging with 3D whole-heart coverage and isotropic spatial resolution. Magn Reson Imaging 63:159–169.

80. Roujol S, Foppa M, Weingartner S, Manning WJ, Nezafat R (2015) Adaptive Registration of Varying Contrast-Weighted Images for Improved Tissue Characterization (ARCTIC): Application to T1 Mapping. Magn Reson Med 73:1469–1482.

81. Wang S-C, Patel AR, Tanaka A, Wang H, Ota T, Lang RM, Carroll TJ, Kawaji K (2017) A novel profile/view ordering with a non-convex star shutter for high-resolution 3D volumetric T_1 mapping under multiple breath-holds: Novel Profile Ordering for 3D T_1 Mapping. Magn Reson Med 77:2215–2224.

82. Kawaji K, Tanaka A, Patel MB, Wang H, Maffessanti F, Ota T, Patel AR (2017) 3D late gadolinium enhanced cardiovascular MR with CENTRA-PLUS profile/view ordering: Feasibility of right ventricular myocardial damage assessment using a swine animal model. Magn Reson Imaging 39:7–14.

83. Sánchez-González J, Fernandez-Jiménez R, Nothnagel ND, López-Martín G, Fuster V, Ibañez B (2015) Optimization of dual-saturation single bolus acquisition for quantitative cardiac perfusion and myocardial blood flow maps. J Cardiovasc Magn Reson 17.1: 21.

84. Weingärtner S, Meßner NM, Budjan J, Loßnitzer D, Mattler U, Papavassiliu T, Zöllner FG, Schad LR (2016) Myocardial T1-mapping at 3T using saturation-recovery: reference values, precision and comparison with MOLLI. J Cardiovasc Magn Reson 18.1: 84.

85. Gudbjartsson H, Patz S (1995) The Rician Distribution of Noisy MRI Data. Magn Reson Med 34:910–914.

86. Yang J, Fan J, Ai D, Zhou S, Tang S, Wang Y (2015) Brain MR image denoising for Rician noise using pre-smooth non-local means filter. Biomed Eng OnLine 14:2.

87. Georgescu M-I, Ionescu RT, Verga N (2020) Convolutional Neural Networks with Intermediate Loss for 3D Super-Resolution of CT and MRI Scans. IEEE Access 8:49112–49124.

88. Kolarik M, Burget R, Uher V, Povoda L (2019) Superresolution of MRI brain images using unbalanced 3D Dense-U-Net network. 42nd Int. Conf. Telecommun. Signal Process. TSP. IEEE, pp 643–646.

89. Anagun Y, Isik S, Seke E (2019) SRLibrary: Comparing different loss functions for super-resolution over various convolutional architectures. J Vis Commun Image Represent 61:178–187.